

INFORMATION TO USERS

This manuscript has been reproduced from the microfilm master. UMI films the text directly from the original or copy submitted. Thus, some thesis and dissertation copies are in typewriter face, while others may be from any type of computer printer.

The quality of this reproduction is dependent upon the quality of the copy submitted. Broken or indistinct print, colored or poor quality illustrations and photographs, print bleedthrough, substandard margins, and improper alignment can adversely affect reproduction.

In the unlikely event that the author did not send UMI a complete manuscript and there are missing pages, these will be noted. Also, if unauthorized copyright material had to be removed, a note will indicate the deletion.

Oversize materials (e.g., maps, drawings, charts) are reproduced by sectioning the original, beginning at the upper left-hand corner and continuing from left to right in equal sections with small overlaps. Each original is also photographed in one exposure and is included in reduced form at the back of the book.

Photographs included in the original manuscript have been reproduced xerographically in this copy. Higher quality 6" x 9" black and white photographic prints are available for any photographs or illustrations appearing in this copy for an additional charge. Contact UMI directly to order.



Bell & Howell Information and Learning
300 North Zeeb Road, Ann Arbor, MI 48106-1346 USA
800-521-0600

NOTE TO USERS

This reproduction is the best copy available

UMI

UNIVERSITY OF ALBERTA

HEAT TRANSFER AND FLUID FLOW IN MICROCHANNELS

BY

GH. MOHIUDDIN MALA



A thesis submitted to the Faculty of Graduate Studies and Research in partial fulfillment
of the requirements for the degree of DOCTOR OF PHILOSOPHY

DEPARTMENT OF MECHANICAL ENGINEERING

EDMONTON ALBERTA

SPRING 1999



National Library
of Canada

Acquisitions and
Bibliographic Services

395 Wellington Street
Ottawa ON K1A 0N4
Canada

Bibliothèque nationale
du Canada

Acquisitions et
services bibliographiques

395, rue Wellington
Ottawa ON K1A 0N4
Canada

Your file Votre référence

Our file Notre référence

The author has granted a non-exclusive licence allowing the National Library of Canada to reproduce, loan, distribute or sell copies of this thesis in microform, paper or electronic formats.

The author retains ownership of the copyright in this thesis. Neither the thesis nor substantial extracts from it may be printed or otherwise reproduced without the author's permission.

L'auteur a accordé une licence non exclusive permettant à la Bibliothèque nationale du Canada de reproduire, prêter, distribuer ou vendre des copies de cette thèse sous la forme de microfiche/film, de reproduction sur papier ou sur format électronique.

L'auteur conserve la propriété du droit d'auteur qui protège cette thèse. Ni la thèse ni des extraits substantiels de celle-ci ne doivent être imprimés ou autrement reproduits sans son autorisation.

0-612-39562-6

Canada

UNIVERSITY OF ALBERTA
LIBRARY RELEASE FORM

NAME OF THE AUTHOR: GH. MOHIUDDIN MALA

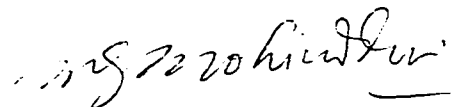
TITLE OF THESIS: HEAT TRANSFER AND FLUID FLOW IN
MICROCHANNELS

DEGREE: DOCTOR OF PHILOSOPHY

YEAR THIS DEGREE GRANTED: 1999

Permission is hereby granted to the University of Alberta to reproduce single copies of this thesis and to lend or sell such copies for private, scholarly or scientific research purpose only.

The author reserves all other publication and other rights in association with the copyright in the thesis, and except as hereinbefore provided neither the thesis nor any substantial portion thereof may be printed or otherwise reproduced in any material form whatever without the author's prior written permission.



Gh. Mohiuddin Mala

414-2865 Ottawa

Ontario, Canada K1V0G8

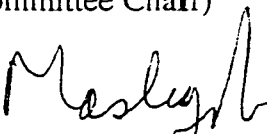
DATED: April 12, 1999

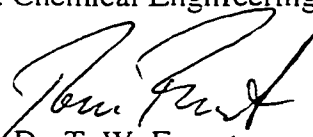
UNIVERSITY OF ALBERTA


FACULTY OF GRADUATE STUDIES AND RESEARCH

The undersigned certify that they have read, and recommended to the Faculty of Graduate Studies and Research for acceptance, a thesis entitled HEAT TRANSFER AND FLUID FLOW IN MICROCHANNELS by GH. MOHIUDDIN MALA in partial fulfillment of the requirements for the degree of DOCTOR OF PHILOSOPHY.


Dr. A. Bhattacharyya
(Committee Chair)


Dr. J.H. Masliyah
(Prof. Chemical Engineering)


Dr. T. W. Forest
(Supervisory Committee Member)
(Chairman, Department of Mechanical Engineering)


Dr. J. D. Dale
(Supervisory Committee Member)


Dr. Dongqing Li
(Supervisor)

Dated: April 12, 1999


Dr. Ayodeji A. Jeje
(External Reader)

Dedication

Dedicated to the loving memories of my younger brother Mohammed Hussain (1971-1988) and my mother-in-law Ms. Sayeeda Hamid. May Allah (SWT) bless them with all the Heavenly Bounties and rest their souls in Peace, Amen.

Abstract

Fluid flow and heat transfer characteristics in microchannels of different cross-sections; parallel plate, cylindrical and trapezoidal microchannels were studied. The trapezoidal microchannels were etched in silicon and glass by photolithographic techniques. The cylindrical microchannels of fused silica and stainless steel were readily available. Channels with depths of 18 μm to 300 μm were studied. The study was divided into three parts viz. theoretical modeling, numerical simulation and experimentation. Electrokinetic effects such as the effects of electrical double layer (EDL) at the solid-liquid interface and surface roughness effects were considered. An experimental apparatus was constructed and a procedure devised to measure the flow rate, pressure drop, temperatures and electrokinetic parameters like streaming potential, streaming current, and conductivity of the working fluid. Great care was taken so that the measurements were accurate and repeatable.

For steady state laminar flow and heat transfer in microchannels, mathematical models were developed that consider the effects of electrical double layer and surface roughness at the microchannel walls. The non-linear, 2-D, Poisson-Boltzmann equation that describes the potential distribution at the solid liquid interface was solved numerically and results were compared with a linear approximate solution that overestimates the potential distribution for higher values of zeta potential. Effects of the EDL field at the solid-liquid interface, surface roughness at the microchannel walls and the channel size, on the velocity distribution, streaming potential, apparent viscosity, temperature distribution and heat transfer characteristics are discussed.

The experimental results indicate significant departure in flow characteristics from the predictions of the Navier-Stokes equations, referred to as conventional theory. The difference between the experimental results and theoretical predictions decreases as the hydraulic diameter increases. For higher hydraulic diameters, the experimental results are in

rough agreement with the predictions of Navier-Stokes equations. For the same volume flow rate, experimentally measured pressure gradients are significantly higher than conventional theory predictions. Therefore, the friction factor and apparent viscosity are higher. The results also indicate material dependence of the flow behavior. The observed effects are attributed to either to an early transition from laminar flow to turbulent flow or to the surface effects; electrokinetic and surface roughness effects.

For parallel plate microchannels, the electrokinetic effects explain the observed differences. For cylindrical and trapezoidal silicon microchannels, experimentally measured pressure drop is significantly higher than conventional theory prediction; with and without electrokinetic effects. For cylindrical microchannels, the electrokinetic effects were not measured as one material was conducting while as for the fused silica the diameter of microchannels was greater than 50 μm . For such large microchannels the EDL effects are negligible as shown by theory. For trapezoidal microchannels, flow rate, pressure drop, temperature and electrokinetic parameters were measured for three different electrolyte concentrations. It was found that the electrokinetic effects are negligible for trapezoidal microchannels having hydraulic diameters greater than 50 μm , and the higher-pressure requirement is because of surface roughness. The roughness-viscosity model developed for cylindrical and trapezoidal microchannels explains the higher-pressure requirement as measured experimentally. The predictions of the roughness viscosity model agree well with the experimental data. The heat transfer characteristics are similar to as obtained by various other researchers. The measured Nusselt numbers were lower than the conventional theoretical predictions but agree well with the modified conventional equation by considering the roughness effects on heat transfer.

ACKNOWLEDGEMENTS

The author wishes to acknowledge the following for their help in the preparation of this thesis.

- Dr. Dongqing Li for his supervision of this research.
- Dr. J. D. Dale and Dr. T. W. Forest for their guidance as part of the author's supervisory committee.
- Dr. Yuebin Ning and Mr. Graham Mckinnon of Alberta Microelectronic Center for providing the facilities for microfabrication of microchannels.
- Mark Ackerman, Allan Muir, Tony, Albert Yuen for their assistance with the design of the experimental apparatus, procedure and data acquisition system.
- Gail, Helen, Doris, Li Ping, and Shelly of Mechanical Engineering Department Office for all their help.
- Interlibrary Loans for providing all the documents not available in U of A Libraries.
- Institute of Polymer Research, Dresden Germany for conducting some of the experiments.
- The Natural Sciences and Engineering Research Council of Canada and Department of Mechanical Engineering for providing funding for the equipment purchased for this research.
- University of Alberta, Alberta Microelectronic Center and Department of Mechanical Engineering for awarding various scholarships/fellowships during the period of this research.
- Weilin Qu, Peter (Yongan Gu), Chun Yang, Ali Atai and Saifu Bekely for their occasional help in code writing and general discussions.
- Ram Maikala and Suman Dee for being so great friends.
- To many other graduate students past and present for extending friendship.
- My parents, for their support and inspiration throughout my entire educational carrier.
- My dearest friends Sajjid and Rosina for being there for me.
- My wife, Samina Shaheen, and my son, Zuhaib Mohiuddin for their unconditional love, support and patience during this research. Thank you for all of your sacrifices for allowing me to pursue my dreams. I love you both very much.



Gh. Mohiuddin Mala

Contents

Chapter 1: Introduction and Background	
1.1	Introduction 1
1.2	Types of Microchannels 4
1.2.1	Non-cylindrical microchannels 4
1.2.2	Cylindrical microchannels 5
1.3	References 6
Chapter 2 Literature Review	
2.1	Overview and applications 7
2.2	Literature review 8
2.2.1	Liquid flow in microchannels 9
2.2.2	Discovery and review of electrokinetic phenomena 12
2.2.3	Heat transfer in microchannels 15
2.3	References 25
Chapter 3: Heat Transfer and Fluid Flow in Parallel Plate Microchannels: Theoretical	
3.1	Introduction 31
3.2	Poisson-Boltzmann equation 34
3.2.1	Solution of the Poisson-Boltzmann equation 36
3.3	Equation of motion 37
3.4	Streaming potential 38
3.5	Volume flow rate 40
3.6	The electroviscous effect 41
3.7	Friction constant 41
3.8	Energy equation 42
3.8.1	Heat transfer coefficient 43
3.9	Results and discussion 43
3.9.1	Prediction of potential distribution 44
3.9.2	Velocity distribution and streaming potential 46
3.9.3	Predictions for friction constant 48
3.9.4	Predictions for apparent viscosity 49

3.9.5	Predictions for heat transfer	50
3.10	Summary	54
3.11	References	55
Chapter 4: Flow Characteristics of Water Through a Microchannel Between Two Parallel Plates with Electrokinetic Effects		
4.1	Introduction	56
4.2	Mathematical model	58
4.2.1	Poisson-Boltzmann equation	59
4.2.2	Equation of motion	60
4.2.3	The streaming potential	61
4.2.4	Volume flow rate and apparent viscosity	63
4.2.5	Friction coefficient	64
4.2.6	Experiments	65
4.3	Data analysis	66
4.3.1	Calculation of $\lambda_s P_s$	66
4.3.2	Determination of channel height and zeta potential	68
4.3.3	Total resistance, streaming potential and zeta potential	68
4.4	Correction factor Φ	71
4.5	Volume flow rate	72
4.6	Velocity distribution	73
4.7	Friction coefficient	74
4.8	Concluding remarks	76
4.9	References	77
Chapter 5: Flow Characteristics of Water in Microtubes		
5.1	Introduction	79
5.2	Experimental apparatus, procedure and results	81
5.3	Early transition to turbulence	86
5.4	Friction characteristics	90
5.5	Effects of surface roughness	93
5.6	Summary	99
5.7	References	100

Chapter 6: Electrical Double Layer Potential Distribution In a Rectangular Microchannel		
6.1	Introduction	102
6.2	Poisson-Boltzmann equation	105
6.3	Solution of the Poisson-Boltzmann equation	107
6.3.1	Linear approximate analytical solution	108
6.3.2	Complete numerical solution by successive overrelaxation	109
6.4	Results and discussion	111
6.5	References	118
Chapter 7: Design of Experimental Apparatus for Trapezoidal Silicon Microchannels		
7.1	Design consideration	120
7.2	Pressure requirement and measurement	122
7.3	Flow rate measurement	123
7.4	Temperature measurement	124
7.5	Measurement of electrokinetic parameters	124
7.6	Conductivity measurement	126
7.7	Micro heater	126
7.8	Microfilter	126
7.9	Microchannel manufacture by silicon micromachining	127
7.9.1	Etching process	127
7.9.2	Precision sawing	132
7.10	Bonding materials to silicon chips	133
7.11	Data acquisition and control	134
7.11.1	Data acquisition card (DAQ)	134
7.11.2	GPIB interface	135
7.11.3	LabView	136
7.12	Procedure	136
7.13	References	137

Chapter 8: Fluid Flow and Heat Transfer Characteristics of Water in Trapezoidal Silicon Microchannels		
8.1	Introduction	138
8.2	Poisson-Boltzmann equation	140
8.3	Equation of motion	142
8.4	Streaming potential	143
8.5	Solution of governing equations	144
8.6	Transformation of actual non-uniform (y,z) to uniform (η,ζ) coordinates	145
8.7	Equation of motion in (η,ζ) Coordinates	147
8.8	Poisson-Boltzmann equation in (η,ζ) Coordinates	149
8.9	Finite difference form of the governing equations	150
8.10	Heat transfer coefficient	152
8.11	Experimental apparatus and procedure	153
8.12	Results and discussion	156
	8.12.1 Flow rate pressure drop characteristics	158
	8.12.2 Friction characteristics	165
	8.12.3 Roughness viscosity model	167
	8.12.4 Heat transfer characteristics	170
8.13	Summary	176
8.14	References	177
Chapter 9: Concluding remarks		
9.1	Contributions of this work	180
9.2	Future work	182
Appendix I: Equipment specification and calibration		
AI.1	Calibration curve for the Valedyne pressure transducer	184
AI.2	Features of the transducer	184
AI.3	Specifications of the high pressure precision pump	185
AI.4	Specifications of the low pressure tubing pump	185
AI.5	Calibration of the flow sensor	185
AI.6	Specifications of the flow sensor	186
AI.7	Specifications of the Keithley 6517A electrometer	187

AI.8	Specifications of the InPro 7001/120 conductivity sensor	187
AI.9	Specifications of the conductivity / resistivity transmitter	188
AI.10	Specifications of the PCI-MIO-16E-4 DAQ Board	189

List of Tables

Table 6.1	Dimensions of stainless steel and fused silica microtubes	83
Table 7.1	Comparison of the mechanical properties of silicon with other commonly used materials	128
Table 7.2	A comparison between etching process and conventional milling process	128
Table 8.1	A comparison of numerical results with analytical results from Shah and London (1978)	152
Table 8.2	Characteristics dimensions of the trapezoidal silicon microchannels	157

List of Figures

Figure 2.1	Schematic of a microchannel heatsink	9
Figure 3.1	Schematic representation of the electrical double layer at the channel wall.	33
Figure 3.2	Schematic of a microchannel between two parallel plates.	36
Figure 3.3	Non-dimensional electrostatic potential distribution near the channel wall for $\xi=50$ mV. $\bar{X} = 0$, center of the channel and $\bar{X} = 1$, the channel wall.	45
Figure 3.4	Non-dimensional streaming potential variation with G_1 for various κ and ξ	46
Figure 3.5	Non-dimensional velocity distribution for various κ with $\xi=50$ mV.	47
Figure 3.6	Variation of C_f with ξ for different values of κ .	48
Figure 3.7	Variation of the ratio of apparent viscosity to bulk viscosity with electrokinetic separation distance, κ .	49
Figure 3.8a	Temperature profile at various cross-sections for $Re = 2.83$.	51
Figure 3.8b	Temperature Profile at Various Cross-sections for $Re = 56.5$.	51
Figure 3.9	Variation of local Nusselt number along the channel length.	52
Figure 3.10	Variation of the average Nusselt number with Reynolds number, Re for $\kappa=40.8$ and $\xi=50$ mV.	53
Figure 4.1	Schematic of a microchannel between two parallel plates.	60
Figure 4.2	Variation of the channel's total electrical resistance with the channel height, (a): Glass and (b): Silicon Channels.	68
Figure 4.3	Variation of streaming potential with channel height for various solution concentrations and channel materials.	69
Figure 4.4	Zeta potential variation with ionic concentration for silicon and glass materials	70
Figure 4.5	Variation of Φ with channel height for silicon and Glass channels with Millipore water as the working fluid.	71

Figure 4.6	A comparison of volume flow rate of Millipore water between Experimental data and the predictions of equation (4.24) (a) in silicon channels (b) in glass channels (c) The predictions of equation (4.24) and of equation (4.26).	73
Figure 4.7	Nondimensional velocity distribution of Millipore water in a 20 μm channel for various ΔP and ξ .	74
Figure 4.8	Variation of friction coefficient with channel height.	75
Figure 5.1	Schematic of experimental setup for flow in stainless steel and fused silica microtubes	82
Figure 5.2	Experimentally measured pressure gradient $\Delta P/\Delta l$ vs. Re for (a) Stainless Steel and (b) Fused Silica microtubes, and comparison with the classical theory, equation (5.1)	84
Figure 5.3	Experimentally obtained correlations of ΔP vs Re in (a) $Re < 500$ (b) $500 < Re < 1500$ and (c) $Re > 1500$ flow regions of a 130 μm SS microtube and comparison with the classical theory, equation (5.1)	88
Figure 5.4	Friction factor, f_{exp} vs. Re for some SS and FS microtubes and comparison with the classical theory, Equations (5.8) and (5.9).	91
Figure 5.5	Friction constant ratio C^* (Equation 5.10) vs. Re for some SS and FS microtubes	92
Figure 5.6	Variation of roughness viscosity ratio with non-dimensional radius for some SS and FS microtubes at $Re = 950$	97
Figure 5.7	Comparison of volume flow rates predicted by the roughness viscosity model with the measured flow rates for some SS and FS microtubes and comparison with Equation 5.1.	98
Figure 5.8	Comparison of the velocity profiles predicted by the roughness viscosity model and the Poiseuille flow equation for some FS and SS microtubes	99
Figure 6.1	Schematic of a rectangular microchannel	106
Figure 6.2	Nondimensional EDL potential distribution in one quarter of the microchannel, with $\xi = 150 \text{ mV}$ a) linear solution, and b) complete numerical solution.	113
Figure 6.3	Nondimensional EDL potential distribution in one quarter of the microchannel, with $\xi = 75 \text{ mV}$ a) linear	

	solution, and b) complete numerical solution.	114
Figure 6.4	Nondimensional <i>EDL</i> potential distribution in one quarter of the microchannel, with $\xi=25$ mV a) linear solution, and b) complete numerical solution.	115
Figure 6.5	Comparison of the profiles of the linear and the nonlinear <i>EDL</i> potential distributions for three zeta potential values.	116
Figure 6.6	Nonlinear <i>EDL</i> potential distribution in a quarter of a microchannel with different ξ potentials at different surfaces.	118
Figure 7.1	Isotropic chemical etching of silicon	130
Figure 7.2	Anisotropic chemical etching of silicon	130
Figure 7.3:	Layout of the microchannel mask as designed in L-edit for anisotropic chemical etching of trapezoidal silicon microchannels	131
Figure 8.1	Schematic of a trapezoidal microchannel in silicon with Pyrex glass cover.	141
Figure 8.2	Schematic of the transformation of non-uniform (y,z) Cartesian coordinates to uniform (η, ζ) computational coordinates.	146
Figure 8.3	Schematic of the experimental apparatus for liquid flow and heat transfer in microchannels with electrokinetic effect measurement.	154
Figure 8.4abc	Pressure drop Vs flow rate characteristics for (a) 51.07 μm , 51.3 μm , and (c) 79.93 μm trapezoidal silicon microchannels for <i>DIUF</i> water, 10^{-5} M and 10^{-4} M KCl electrolyte concentrations.	159
Figure 8.4d	Experimentally measured pressure drop Vs flow rate characteristics for 114.5 μm hydraulic diameter trapezoidal silicon microchannels for <i>DIUF</i> water, 10^{-5} M and 10^{-4} M KCl electrolyte concentrations.	160
Figure 8.4e	Comparison of the theoretically predicted pressure drop with experimentally measured pressure drop for 51.3 μm hydraulic diameter trapezoidal silicon microchannel for <i>DIUF</i> water.	161
Figure 8.4f	Comparison of the theoretically predicted pressure drop with experimentally measured pressure drop for 51.3 μm hydraulic diameter trapezoidal silicon microchannel for 10^{-5} M KCl water.	162
Figure 8.4g	Comparison of the theoretically predicted pressure drop with experimentally measured pressure drop for 51.3 μm hydraulic	

	diameter trapezoidal silicon microchannel for 10^{-4} M KCl water.	162
Figure 8.4h	Comparison of the experimentally measured pressure gradient with theoretical prediction for (1) 51.3 μm , (2) 62.3 μm , and (3) 64.9 μm hydraulic diameter trapezoidal silicon microchannels for DIUF water.	164
Figure 8.4i	Comparison of the experimentally measured pressure gradient with theoretical prediction for (4) 114.5 μm , (5) 142 μm , and (6) 168.9 μm hydraulic diameter trapezoidal silicon microchannels for DIUF water.	166
Figure 8.5a	A comparison of the experimental and theoretical predictions of friction factor for (a) 51.3 μm , (b) 62.3 μm , (c) 64.9 μm , (d) 114.5 μm , (e) 142 μm , and (f) 168.9 μm , hydraulic diameter trapezoidal silicon microchannels for DIUF water.	166
Figure 8.5b	: Friction constant ratio Vs Reynolds number for (a) 51.3 μm , (b) 62.3 μm , (c) 64.9 μm , (d) 114.5 μm , (e) 142 μm , and (f) 168.9 μm , hydraulic diameter trapezoidal silicon microchannels for DIUF water.	166
Figure 8.6a	A comparison of the experimental pressure gradient Vs Reynolds number with the theoretical predictions of roughness viscosity model for (a) 51.3 μm , (b) 62.3 μm , (c) 64.9 μm hydraulic diameter trapezoidal silicon microchannels for DIUF water.	171
Figure 8.6b	A comparison of the experimental pressure gradient Vs Reynolds number with the theoretical predictions of roughness viscosity model for (d) 114.5 μm , (e) 142 μm , and (f) 168.9 μm , hydraulic diameter trapezoidal silicon microchannels for DIUF water.	171
Figure 8.7a	Nusselt number vs Reynolds number for a 62.3 μm trapezoidal silicon microchannel and comparison of the experimental results with conventional theory and RVM.	173
Figure 8.7b	Nusselt number vs Reynolds number for a 63.1 μm trapezoidal silicon microchannel and comparison of the experimental results with conventional theory and RVM.	173
Figure 8.7c	Nusselt number vs Reynolds number for a 114.5 μm trapezoidal silicon microchannel and comparison of the experimental results with conventional theory, Peng et al and RVM	174
Figure 8.7d	Nusselt number vs Reynolds number for a 168.9 μm trapezoidal silicon microchannel and comparison of the experimental results with conventional theory, Peng et al and RVM.	174

List of symbols used

A	Coefficients in the roughness-viscosity function
A_c	Cross-sectional area of the flow channel, m^2
A_s	Surface area of the flow channel, m^2
B_r	Brinkman number
C_f	Friction constant, f^*Re dimensionless
C	Friction constant, f^*Re
$Conc1$	Concentration number 1, $10^{-5} M$ KCl
$Conc2$	Concentration number 1, $10^{-4} M$ KCl
$C, C_{i=1...4}$	Constants in Chapter 8
C^*	Friction constant ratio, Equation (5.10)
C_p	Specific heat of water, $kJ/kg-K$
D	Diameter of the tube, m
$DIUF$	De-ionized ultra filtered water
EDL	Electric double layer, V
E_c	Eckert number, dimensionless
E_s	Streaming potential, V
E_z, E_x	Electric field strength, $V m^{-1}$
E_1, E_2, E_3	Parameters in Equations (5.15) and (5.16)
F	Body force vector
FS	Fused silica
G_1, G_2, G_3	Non-dimensional parameter
H	Height of the microchannel, m
J	Jacobian determinant
I_c, I_s	Conduction and streaming currents respectively, A
Nu	Nusselt number, dimensionless
Nu_{av}	Average Nusselt number, dimensionless
P	Pressure vector
Pr	Prandtl number, dimensionless
P	Pressure at any point, N/m^2
PBE	Poisson-Boltzmann equation

P_s	Wetted perimeter of the channel, m
P_z	Pressure gradient in Z-direction = dp/dZ , $Pa\ m^{-1}$ ($N\ m^{-3}$)
Q	volume flow rate through the channel, $m^3\ s^{-1}$
Q_p	Conventional volume flow rate through the channel, $m^3\ s^{-1}$
R	Radius of the microtube, m
R_b	Bulk electrical resistance of the liquid flowing in the channel, Ω
Re	Reynolds number, <i>dimensionless</i>
Re_k	Reynolds number based on the roughness ($U_k\ k/\nu$)
Re_{ref}	Reference Reynolds number
RVM	Roughness Viscosity Model
R_s	Surface electrical resistance of the channel, Ω
R_T	Total electrical resistance of the channel with the liquid, Ω
SS	Stainless steel
T	Absolute temperature, K
T_i, T_{in}	Inlet fluid temperature, K
T_m, T_f	Mean temperature of the fluid, K
T_w	Wall temperature, K
U	Reference velocity (chapter 8) m/s
U_k	Velocity at the top of the roughness element, m/s
V_{av}	Average velocity of the fluid, $m\ s^{-1}$
V_o	Reference velocity, (<i>arbitrarily chosen as $1\ m\ s^{-1}$</i>)
V_z	Velocity of the fluid in z-direction, $m\ s^{-1}$
W	Width of the microchannel, m
X, Y, Z	Cartesian coordinates, m
a	Half distance between the plates, m
a, b, h	Channel dimensions (Chapter 8)
c_p	Specific heat of the fluid, $kJ/kg\cdot K$
d_h	Hydraulic diameter of non-circular microchannels, m
e	Electron charge, $1.6021 \times 10^{-19}\ C$
	Strain (Chapter 7)
f	Friction factor, <i>dimensionless</i>

h	Heat transfer coefficient, $W m^{-2} K^{-1}$
$i j k$	Summation / Iteration index, (Chapter 5)
k	Debye-Huckel parameter, $(2n_o z^2 e^2 / \epsilon \epsilon_o k_b T)^{1/2} m^{-1}$
	Height of the roughness element, m (Chapter 6)
l	Length of the microtube, m
k_b	Boltzmann constant, $1.3805 \times 10^{-23} J mol^{-1} K^{-1}$
k, k_f	Thermal conductivity of the fluid, $W m^{-1} K^{-1}$
l	Length of the channel, m
$m n$	Summation index, (Chapter 6, 8)
\dot{m}	mass flow rate of water, kg/s
$n^+ n^-$	Concentration of positive and negative ions, m^{-3}
n_o	Average number of positive or negative ions/unit volume or ionic number concentration, m^{-3}
p	Perimeter / nondimensional pressure
\dot{q}	Heat gained by water, W
r	Radial co-ordinate, m
t	Time interval
u	Velocity vector
u	Velocity component in flow-direction, m/s
v_r	Relative speed of molecules
x	Coordinate in the axial / flow direction, m
$x y z$	Non-dimensional x and y co-ordinates, (Chapter 6, 8)
$z^+ z^-$	Valence of the positive and negative ions, <i>dimensionless</i>

Greek Symbols

$\alpha \beta \chi$	Constants
α_t	Thermal diffusivity of the fluid
β_x, β_y	Collocation parameters for x and y directions, (Chapter 5)
χ	Parameter used in chapter 6
ΔP	Pressure gradient across the tube, $N m^{-2}$
$\Delta x \Delta y \Delta z$	Step sizes in x y and z directions

ε	Dielectric constant of the medium, <i>dimensionless</i>
ε_0	Permittivity of vacuum, $8.854 \times 10^{-12} \text{ C V}^{-1} \text{ m}^{-1}$
ϕ	Angle in trapezoidal microchannels
η	Uniform computation coordinate (<i>Chapter 8</i>)
κ	Non-dimensional electrokinetic separation distance between the two plates, a^*k
λ_b	bulk conductivity of the fluid, $\Omega^{-1} \text{ m}^{-1}$
λ_s	surface conductivity of the channel wall, Ω^{-1}
λ_T	Total conductivity of the fluid, $\Omega^{-1} \text{ m}^{-1}$
λ_o	Electrical conductivity of the fluid, $\Omega^{-1} \text{ m}^{-1}$
μ	Dynamic viscosity of the fluid, $N \text{ s m}^{-2}$
μ_a	Apparent viscosity of the fluid, $N \text{ s m}^{-2}$
μ_R	Roughness viscosity on top of the roughness element, $N \text{ s m}^{-2}$
μ_{Rwm}	Mean wall roughness viscosity on top of roughness element, $N \text{ s m}^{-2}$
μ_w	Dynamic viscosity of the water at wall temperature, $N \text{ s m}^{-2}$
ν	Kinematic viscosity of water, $\text{m}^2 \text{ s}^{-1}$
ω	Relaxation parameter
Φ	Correction factor applied to the classical equation to incorporate the surface conductance effect
θ	Non-dimensional temperature distribution, <i>dimensionless</i>
θ_m	Non-dimensional mean temperature distribution, <i>dimensionless</i>
ρ	Charge density, C m^{-3} Density of water, kg m^{-3} (<i>Chapter 5, 8</i>) Resistivity of the material (<i>Chapter 7</i>)
ρ_f	Density of fluid, kg m^{-3}
σ	Molecular diameter or collision distance from center to center
τ_w	Shear stress at the channel wall, $N \text{ m}^{-2}$
ξ	Zeta potential, i.e., the electric potential at the boundary between the diffuse double layer and the compact layer, V
ψ	Electrostatic potential at any point in the electric double layer, V
Ψ	Electrostatic potential at any point in the electric double layer, V

ψ	Non-dimensional electrostatic potential in the electrical double layer, (<i>Chapter 5</i>)
ψ_o	Electrostatic potential at the channel wall, V
ζ	Uniform computation coordinate (<i>Chapter 8</i>)

Subscripts

<i>ave</i>	Average
<i>e</i>	Electrokinetic
<i>exp</i>	Experimental value
<i>max</i>	Maximum value
<i>thy, thry</i>	Theoretical value
<i>m</i>	Mean
<i>1</i>	shorter length
<i>2</i>	longer length

Superscript

-	Non-dimensional parameters
---	----------------------------

Chapter 1 Introduction and Background

1.1 Introduction:

The design of modern electronic devices and systems comprises millions of small components. This high component concentration at the chip level has lead to significant increases in the chip cooling requirements due to greater dissipative heat fluxes. New technologies are developed stages to meet these cooling demands. These include mini and microchannel liquid cooled heatsinks. Flow in microchannels has been demonstrated to yield very high heat transfer coefficients and thus offer a compact and viable solution to this heat dissipation problem, Tuckermann (1984). However, to design an efficient liquid cooled microchannel heatsink, it is necessary to understand the flow characteristics in microchannels. Only after obtaining the flow characteristics can the energy equation be solved to determine the heat transfer characteristics. But to date, the fundamental knowledge of flow characteristics such as flow pattern, pressure loss, friction characteristics etc. which are all important parameters is limited.

The primary objective of this work was to investigate and understand the fundamental characteristics of fluid flow and heat transfer in microchannels of various cross-sections. More emphasis was laid on the flow characteristics because an examination of the pertinent literature revealed conflicting reports about the pressure loss, friction factor, apparent viscosity, and flow pattern in microchannels. For example, in microchannels the early transition of flow from laminar to turbulent at $Re \geq 300$, experimentally measured higher-pressure gradients in laminar flow compared to theoretical predictions and the question of solid surface effects on the apparent viscosity

have attracted considerable attention in scientific literature. The apparent viscosity is a characteristic of the flow field and calculated in such a way that if substituted for the bulk viscosity the Navier-Stokes predictions should be in agreement with the experimental observations. However, these effects are not due to any particular phenomena but there are a number of factors, like the electrokinetic and surface roughness effects which contribute to these anomalies. Therefore, to accurately predict the flow characteristics in microchannels, one needs to answer the following questions:

- 1 Do Navier-Stokes equations adequately model the fluid flow at these small scales or should they be modified and if so how?
- 2 Whether phenomena, which typically are ignored in large-scale channels, become important in microchannels?
- 3 Is transition to turbulence affected by the small size of the channels?

This dissertation, written in paper format, critically examines fluid flow and heat transfer characteristics in microchannels of various cross-sections like parallel plate, cylindrical and trapezoidal microchannels. The remainder of the Chapter 1 describes different types of microchannels.

In Chapter 2, an overview and applications of microchannel flow is presented. An extensive review of the pertinent literature on microchannel fluid flow and heat transfer is also discussed.

In Chapter 3, a mathematical model for liquid flow and heat transfer in microchannels between two parallel plates with electrokinetic effects is developed. The governing equations are solved numerically and predictions for flow and heat transfer are made. The results show that the presence of EDL effect at the solid liquid interface

results in a higher apparent viscosity, thus a higher flow resistance and lower heat transfer coefficients than obtained with conventional theory.

In Chapter 4, experimental results of liquid flow in silicon and glass parallel plate microchannels with electrokinetic effects are discussed. The experimental results are compared with the predictions of the mathematical model developed in Chapter 3. Good agreement between the experimental results and theoretical predictions has been found.

In Chapter 5, flow characteristics of water in stainless steel and fused silica microtubes of 50 to 254 μm diameters are discussed. The required experimental pressure gradient is much higher than that predicted by the conventional theory (Poiseuille flow equation). This higher-pressure drop is explained in terms of the change in flow pattern i.e. transition of flow from laminar to turbulent, and distributed surface roughness effects. A mathematical model that incorporates the effects of surface roughness in laminar flow by modifying the momentum equation is developed. A good agreement between the predictions of roughness viscosity model and experimental results has been found.

In Chapter 6, the Poisson-Boltzmann equation that describes the distribution of the electrical double layer potential at the solid liquid interface is solved. As the Poisson-Boltzmann equation is exponentially non-linear, an analytical solution is not possible. The complete numerical solution is compared with the linear approximate solution.

In Chapter 7, a detailed description of the experimental design and apparatus developed during the course of this work is given. Experimental procedure, data acquisition, microchannel fabrication and equipment specification are discussed in detail.

In Chapter 8, flow and heat transfer characteristics of water in trapezoidal silicon microchannels are discussed. The experimental results for flow and heat transfer are

compared with the theoretical predictions. The governing equations are solved numerically for the exact geometry.

Chapter 9 briefly summarizes the results and contributions of this work. Suggestions and directions for future research work are also discussed.

1.2 Types of microchannels

Microelectromechanical systems and devices use microchannels of various cross-sections and shapes, which vary from cylindrical pores to parallel plate configurations. Numbers of companies have developed proprietary processes for fabricating structures containing such microchannels. These structures may be planar or three dimensional, while the microchannels within the structure can have a hydraulic diameter of 5 μm to 1 mm. The length to diameter ratios of these microchannels varies from 50 to 5000. Microchannel center to center distance can vary, as they are geometry dependent and can be as small as 100 μm . These microchannels can be broadly classified into two categories: cylindrical and non-cylindrical. In non-cylindrical microchannels, rectangular, trapezoidal and parallel plate configurations are most commonly used.

1.2.1 Non-cylindrical microchannels

The microchanneled structure program has gone through different development stages to meet the diverse criteria required for different microfluidic and heat exchanger applications like, micro-valves and VLSI heatsinks etc. This led to the development of near rectangular channels produced on plates of different dimensions. The 3M Company, as reported by Hoopman (1991), produced channels on 25 cm by 60 cm plated with microchannels in the long direction, as it is economical to produce microchannels on small dimensions. The advantages of the rectangular microchannels are reported to be:

1. High channel surface area to flow cross-sectional ratio.
2. Wall between channels can be controlled down to less than 25 μm .
3. High percentage of open area.
4. Internal surface finish of the channels is better than 0.5 μm .
5. Process must be suitable for fabrication of large flat plates.
6. Can be fabricated in a finned plate configuration

The disadvantages are:

1. Lower pressure capabilities.
2. Lower channel to channel pressure differential.
3. Requires an overall high plate thickness.
4. Not as readily adaptable to three-dimensional structures.

1.2.2 Cylindrical microchannels

The circular section microchannels may vary in shape and /or size along the length of the channel. This provides the opportunity to control the pressure drop and heat transfer coefficients at different areas of the structure. So far microchannels have been made on 30 cm by 30 cm plate of copper, nickel lined channels. The advantages of such processes are:

1. Wide ranges of channel sizes are available from 5 μm to 1 mm.
2. Many channel variations like bends, T-shapes etc. are possible.
3. Channel shapes and sizes can be varied along the length.
4. Internal surface finish of the channels can be controlled.
5. Channels can handle high pressures.
6. Process adapts well to three-dimensional structures.

The disadvantages are:

1. Difficult to control the channel straightness at l/d ratios greater than 500.
2. Low ratio of channel internal surface area to structure surface area.

1.3 References

1. Hoopman TL, 1991, 'Microchanneled structures', ASME Vol. DSC-19, pp. 171-174
2. Tuckerman, D.B., (1984), 'Heat transfer microstructures for integrated cooling,' Ph.D. Thesis, Stanford University, Stanford, CA.

Chapter 2 Literature Review

2.1 Overview and applications

The miniaturization of electronic equipment, commonly referred to as microelectronic systems, has produced a far-reaching technological revolution. Researchers are working towards creating micromachines that find applications in almost all fields of life by using techniques originally developed to fabricate integrated circuits. The goal is to make fully assembled devices and systems that can replace large-scale electromechanical systems cheaply and perform equally or better. Because of the miniature size, the microelectromechanical systems can also be used at places where the conventional electromechanical systems could not be used owing to their size and weight. The potential applications for these micromachines are consumer products. Some of the most exciting possibilities are: tools for microsurgery, instruments for use in spacecraft, systems for fiber optics communications, thermal control and microelectronic cooling, sensors and actuators, biomedical applications and scientific instruments.

The design of microelectromechanical systems calls upon a large range of engineering skills and talents. For applications like thermal control and electronic cooling (*e.g.* water-cooled heatsinks), sensors and actuators, biomedical applications, microscale pumps and valves, etc. the understanding of fluid flow and thermal behavior in microchannels of various cross-sectional shapes is vital. This makes fluid dynamics and heat transfer pivotal for continued success in micromachining technology. A detailed theoretical and experimental analysis of microscale flow is needed to understand the basic principles and to explore whether any new phenomena are encountered in the microflow

domain and if any phenomena that are ignored in macro-scale flow are important in the microscale flow. However, it must be remembered that the microscale regime is much smaller than the macroscale world but is larger than the continuum limit.

2.2 Literature review

As discussed earlier innovative cooling techniques are required to meet cooling requirements of electronic devices and systems that exceed 10^6 W/m². Liquid cooled microchannel heatsinks are promising solutions. A microchannel heat sink is a structure with number of micron-size microchannels fabricated on the other side of the electronic chip. The microchannel side is anodically bonded to a cover plate (usually Pyrex glass) to form closed channels, as shown in Figure 2.1. A liquid coolant is made to flow through these microchannels to carry the dissipated heat. The dissipated heat passes through to the heat sink by conduction, and then to the coolant by convection.

For an efficient heat sink design, with water or any other liquid as the working fluid, it is imperative to understand the fundamentals of fluid flow at microscale level. Analysis of microscale flow involves conventional fluid mechanics with interfacial effects, which are generally ignored in conventional theory. These interfacial effects are present at the solid liquid interface. The interfacial effects are considered in electrokinetic phenomena, which account for the properties of the surfaces and the electrolytes. Only after solving the flow problem with as much detail as possible, can the heat transfer problem be solved. Consequently, in reviewing the related previous works about fluid flow and heat transfer in microchannels, the review is divided into three parts, (i) liquid flow in microchannels, (ii) electrokinetic flow, and (iii) heat transfer in microchannels.

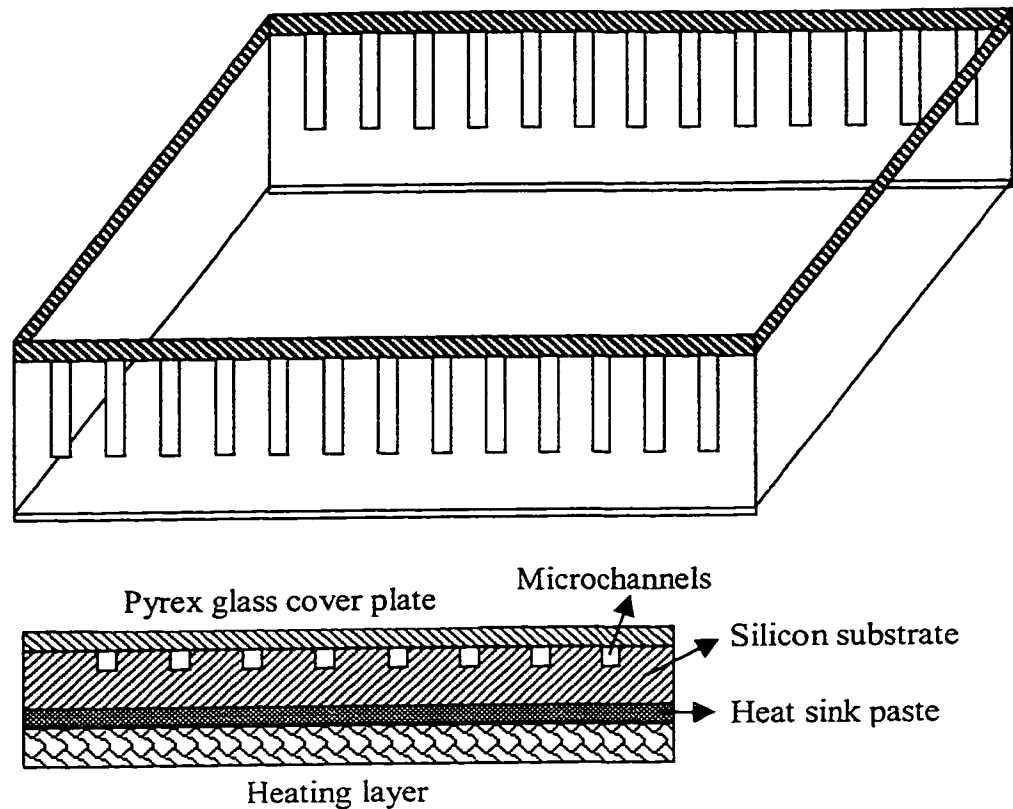


Figure 2.1: Schematic of a microchannel heatsink

2.2.1 Liquid flow in microchannels

Several researchers have studied liquid flow in small capillaries and microchannels. Some of the studies found a good agreement with the conventional theory (Navier-Stokes Equations) while in others cases the results deviated sufficiently. Anderson and Quinn (1972) investigated the mobility of ions in water a few molecular diameters from a hydrophilic water-solid interface. They found that the water retained all its characteristic bulk properties for Mica pores as small as 56 Angstroms. Guvenc (1985) developed a V-groove multi-pass capillary structure to control and measure low flow rates in portable drug infusers. The grooves were isosceles triangles with a base of $50\mu\text{m}$ and a depth of $35\mu\text{m}$.

Guvenc plotted flow rate versus pressure drop and showed good agreement with the theory. Nakagawa et al. (1990) investigated water flow in channels 5 μm deep and 200-800 μm wide and their results were within 10% of conventional theory. Israelachvili and collaborators (1986, 1990) have done a considerable amount of work concerning viscous forces in thin films. He found that the apparent viscosity was about the same as the bulk viscosity for films thicker than ten molecular layers or 5 nm. For thinner films, the apparent viscosity depends on the number of molecular layers and can be as much as 10^5 times larger than the bulk viscosity. Chan and Horn (1985), reported that the apparent viscosity does not deviate from the bulk viscosity in films as thin as 50nm and that it increases slightly in thinner films. The apparatus used by Israelachvili, and Chan and Horn, consisted of two crossed mica cylinders with a small gap in between. Horn et al. (1989) used the Israelachvili apparatus to study the forces between two silica surfaces. Again they found that the viscosity between the surfaces did not differ from the bulk viscosity. The flow in this apparatus is considerably different from the Poiseuille flow in the microchannels used in this study. Migun and Prokhorenko (1987) found that the apparent viscosity of polar indicator liquids increases in capillaries smaller than 1 μm diameter. They believe this is due to an increased structure in the fluid near the wall. Derjaguin et al. (1983) reported an increase in the apparent viscosity for polar liquid layers less than 12 nm. In contrast, Debye and Cleland (1959) reported that the apparent viscosity was smaller than bulk viscosity for paraffin flow in porous glass with average pore size several times larger than molecular size. They believe that the reduction in apparent viscosity is due to an adsorbed layer on the wall that has a finite slip velocity. Molecular dynamic simulations have been used to examine the molecular structure of fluid flow. Koplik et al. (1989, 1988) have studied the

slow flow of a viscous Lennard-Jones fluid past a solid wall, and found that slip can occur in the case of moving contact lines. Slip along the wall results in a reduction on the apparent viscosity. Hess and Loose (1989) used non-equilibrium molecular dynamics to find a slip length for dense fluids on the order of molecular diameters. Thompson and Robbins (1990) found that the degree of slip was proportional to the amount of structure introduced in the fluid from the wall interaction. Contrary to this, Bitsanis et al. (1990), and Heinbuch and Fisher (1989) found that there is a molecular sticking, or increased apparent viscosity, in molecularly narrow pores. Pfahler (1992) conducted experimental investigation of Newtonian and non-Newtonian fluid flow in extremely small channels. For Newtonian fluids, he observed a reduction in friction or a reduced apparent viscosity in microchannels with depth less than 40 μm . For alcohol, the decrease reached a plateau at about 70% of the theory for depths between 0.5 and 10 μm and the results were independent of Reynolds number. The silicon oil viscosity decreased with the depth and also showed some dependence on Reynolds number. He found that as the channels have a large surface area to volume ratio the surface characteristics might play an important role in fluid flow characteristics in these microchannels. He showed through flow visualization using fluorescent micro-beads that typical macro-channel patterns prevail in microchannels also. For non-Newtonian fluids (biological fluids) he concluded that their behavior in micro-scaled devices was similar to their behavior in macro-scale. Nevertheless, he observed an anomalous non-Newtonian behavior in the biological fluids at much higher shear rates than expected.

2.2.2 *Discovery and review of electrokinetic phenomena*

As is evident from the reviews of the latest works on flow in microchannels, one notices that there are conflicting reports about fluid flow characteristics such as apparent viscosity, friction factor, friction constant, etc.. One possible explanation is the effect of electrokinetic phenomena. In conventional fluid mechanics these effects are very small and are neglected. But when the dimensions are reduced to micrometer scale, these electrokinetic effects become substantially important and thus need to be considered in order to model it correctly.

Electrokinetic phenomena were discovered quite early in the 19th century. Investigations along these lines have been conducted for more than a century and a half, Dukhin and Derjaguin (1974). During this period, the development of research in electrokinetic phenomena has contributed substantially, to the formation and understanding of the nature of the surface electric charges and electrical structure of the interfacial layer. Reuss (1809) discovered that flow through capillary elements could be induced by the application of an electrical field. In the following decades a number of authors, Abramson (1934), substantiated the existence of effects discovered by Reuss and promulgated fundamental theories of electrokinetics. Quincke (1859) discovered the phenomenon of streaming potential, which is the converse of electroosmosis. (Electroosmosis is the movement of liquid under the action of an external electrical field. The opposite effect, i.e. streaming potential is the appearance of a potential difference under the influence of the flow of a liquid). Quincke observed that when distilled water was forced through a diaphragm, the voltage developed across the diaphragm was proportional to the pressure differential causing the flow. A change in flow direction caused a change in electrical field

direction. Due to the research of Quincke and other investigators, it became clear that electrokinetic phenomena and, accordingly, the presence of surface charges in the boundary region between the liquid and the solid were the rule, rather than the exception, as every investigated inorganic or organic substance showed a charge on contact with a liquid, especially when the liquid was distilled water.

One may note that in the preceding discussion, the experiments conducted used micro-capillaries having characteristic dimensions from few molecular diameters to few microns. The microchannels used in this study fall in the same range of dimensions. Therefore, it is logical to expect the electrokinetic effects to be significant in pressure driven flows in microchannels and microcapillaries having equivalent dimensions with water as the working fluid. Thus to model the flow through these microchannels, electrokinetic phenomena should be considered.

The electrokinetic phenomena have been investigated thoroughly after the early experiments of Quincke. The literature is so enormous that it is impossible to review it in a few pages. However, a review of most related works to flow in microchannels is presented.

Helmholtz (1879) developed the double layer theory, which related analytically the electrical and flow parameters of electrokinetic transport. Although the theory was based on a somewhat intuitive analysis, it has stood the test of time and still represents an acceptable formulation of the electroosmotic phenomena in most capillaries. Smoluchowski (1903) expanded on the Helmholtz double layer theory by taking into account the actual distribution of velocity in the capillary channel. Freundlich (1909), published results of a number of comprehensive experiments dealing with electrokinetic effects, and was the first to use the word electrokinetics to describe the phenomena. He

demonstrated that the proportionality constant in electroosmosis, relating volumetric flow to electric current, was identical with the proportionality constant relating streaming potential and applied pressure.

A more realistic concept of the potential and charge distribution in the fluid adjacent to the capillary wall was introduced by Gouy (1910). He computed the electric charge distribution in a diffuse layer. Debye and Huckel (1923), determined the ionic distribution in solutions of low ionic energy, by means of a linear simplification of the exponential Boltzmann ion energy distribution. Various researchers have contributed to the technology of electrokinetics, and a comprehensive treatment of the classical theories of electroosmosis and streaming potential can be found in Burgreen and Nakache (1963), Bikerman (1958), Davis and Rideal (1961). Adamson ((1990) and Colloid and Surface Science compendium.

Lately, Burgreen and Nakache (1964) analytically investigated electrokinetic flow in very fine capillary channels of rectangular cross-section. They extended the general electrokinetic theory to small electrokinetic radius with high interface source potential. They found that when the fineness of the capillary approaches to $0.1\ \mu\text{m}$, at high surface potential, the retardation approaches 100% of the flow, i.e. the capillary would appear completely impermeable. Rice and Whitehead (1965) studied electrokinetic flow in narrow cylindrical capillaries by making use of the linear approximation (often referred to as Debye-Huckel approximation) for the net charge density in the double layer. Their results are applicable to surfaces at $\zeta < 50\ \text{mV}$, and are comparable to those of Burgreen and Nakache (1964). Levine, et al. (1975) extended the Rice and Whitehead theory to higher surface potentials without the use of Debye-Huckel approximation. They made predictions

about the streaming potential gradient and the electroviscous retardation effect, which manifests itself in an apparent viscosity that is always greater than the bulk viscosity of the fluid. Anderson and Koh (1977) computed the electrokinetic parameters for three different shapes; circle, ellipse and parallel plates. They solved the non-linear Poisson-Boltzmann equation numerically for potential profiles, which were integrated, with the classical momentum and conduction equations. They concluded that the capillary shape was sometimes an important factor. They calculated the electroviscous effect for water filled circular capillaries and found that its maximum augmentation is 28% of the bulk solution viscosity.

2.2.3 Heat transfer in microchannels

By early 1980's Tuckerman and Pease (1981a, 1981b, 1981c, 1982) and Tuckerman (1984) showed that the microfabrication techniques used for microelectronic devices could also be used to fabricate heat sinks. With these techniques, they were able to produce large aspect ratio channels with channel widths of the order of 50 μm and channel height of the order of several hundred micrometers. Fins, typically about 50 μm wide, separated these channels. They tested a 1cm by 1cm square, water-cooled heat sink, and found that for a 20.7 kPa (30psi) water pressure drop, there was an optimal design channel width and fin height of 57 μm , with channel aspect ratio of 6.4 that yielded best results. The experimental data presented agreed very closely with the theoretical predictions. Heat dissipation as high as 790 W/cm^2 and thermal resistance as low as $0.090^\circ\text{C}/(\text{W}/\text{cm}^2)$ was obtained.

The heat transfer between the coolant and the heat sink contributes significantly to the total thermal resistance in electronic component packages. Increasing the area of the heat sink in contact with the coolant can enhance the heat transfer and, therefore, the use of fins

is common. However, it has not been generally recognised that for laminar flow in confined channels, the heat transfer coefficient is inversely proportional to the width of the channels.

Tuckerman and Pease subsequently published several papers relating to microchannel heat sinks. A detailed description of their work can be found in Tuckerman's dissertation. They tested a pin fin structure that had the best thermal performance and dissipation in excess of 1300 W/cm^2 was obtained. Since their landmark work, several other researchers have published theoretical and or experimental works on microchannel heat sinks.

Goldberg (1984) studied thermal and fluid performance of laminar flow, air-cooled microchannel air heat sinks fabricated in copper. Sixteen, $0.508 \times 0.508 \text{ cm}$ chips, on 12.70 mm centres were each provided with a copper heat sink containing 0.635 cm long channels. The channel widths of 0.127 mm , 0.254 mm , and 0.635 mm were investigated. The fin width was equal to the channel width in all the cases. Thermal resistances as low as $3.4 \text{ }^\circ\text{C/W}$ were measured, which is more than an order of magnitude larger than those obtained by Tuckerman and Pease. Nevertheless, these values were in good agreement with calculated values.

Many authors have considered heat transfer in microstructures for cooling silicon chips wherein water flows through the microchannels etched in the back of the silicon wafer. Samalam (1989) reduced the analysis of this problem to a quasi-two-dimensional differential equation and presented exact analytical solutions to obtain the optimum dimensions of the channel width and spacing. Numerical examples showed that using these optimum values could lower the thermal resistance. A Laplace transform approach was used to solve the governing equations and defined the temperature field in each fin. Samalam

then optimised the channel width and spacing dimensions by using the obtained solution to find a minimum value of thermal resistance. Optimising the fin dimensions was found to be more important as the value of the aspect ratio (channel height to width) was allowed to decrease. Ideally aspect ratios as great as 10 were found to be desirable, although aspect ratios varying from 4 to 6 were predicted to provide acceptable performance.

Weisberg, et al. (1990) conducted a theoretical study of heat transfer in devices with multiple channels employed for heat removal from uniformly distributed heat sources. The conjugate heat transfer problem consisting of the determination of the temperature fields in both the solid substrate and the fluid was solved numerically. The numerical code was verified by comparison with an analytical solution for the special case when the solid and the fluid had similar thermal conductivities. These results were of use in the design and optimisation of an integrated cooling system for electronic circuits. Other analyses Tuckermann (1984), Keyes (1984), and Samalam (1989) assumed the heat transfer coefficient to be constant along the fin and neglected heat transfer from the channel's bottom. This study indicated that, in fact the heat transfer coefficient attained the local maxima at the middle point (both height and width) of the channel. As a result more heat will flow upward in the fin and the fin's temperature will tend to be more uniform than predicted by the constant heat transfer coefficient model. This would be especially true when the solid thermal conductivity is much larger than that of the liquid. The authors also determined that under certain conditions, the problem could be simplified by assuming the solid to be isothermal (*i.e.*, solid thermal conductivity is infinitely large compared to the rest of the system). When valid, this approximation greatly simplifies the solution of the governing equations. This investigation was extended in an investigation of flat plate heat

exchangers (Weisberg and Bau, 1992) similar to those fabricated in the back of electronic chips. In addition a design algorithm for the selection of the heat exchanger dimensions was presented.

Beir, *et al.* (1990) reported on a mechanical method for manufacturing microstructural bodies based on the surface shaping of foils by precision cutting with microtools. This technology had been applied to manufacture compact cross flow micro heat exchangers made of aluminium alloys, copper, stainless steel, and titanium. Electron beam welding, laser welding, and diffusion bonding of micro heat exchangers had been performed. Using these types of microheat exchangers with water as working fluid, it was possible to transfer in a volume of 1 cm^3 thermal powers of about 20 kW at mean logarithmic differential temperature of 60 K. This corresponded to volumetric heat transfer coefficients of more than $300 \text{ MW/m}^3\text{-K}$. The maximum volumetric heat transfer coefficient observed was 324 MW/m^3 , corresponding to a heat transfer coefficient from water to water of approximately $22.8 \text{ MW/m}^2\text{K}$ at a flow rate of 12.5 l/min.

Wang, *et al.* (1991) experimentally evaluated the thermal performance and hydraulic resistance of two micro heat exchangers using a hot/cold water test loop. The exchangers had 30 plates each on the cold and hot sides with the channel dimensions ranging between 0.3 and 4.5 mm. The effects of channel size and wall thermal conductivity were also discussed. The measured volumetric heat transfer coefficients were as high as $7 \text{ MW/m}^3\text{-K}$. The channel size and wall materials were found to have a strong influence on the heat transfer capability of a micro heat exchanger. Two heat exchangers one of Brass and the other of SS-316, with two channel patterns were fabricated. Volumetric heat transfer coefficients up to $2.3 \text{ MW/m}^3\text{-K}$ (SS 316) and $7 \text{ MW/m}^3\text{-K}$ (Brass) were measured in the test

range. The Nusselt number was found to be independent of the Reynolds number for SS-316 micro heat exchanger. This was mostly due to the effect of the difference in material conductivity on the thermal entry region.

Choi, *et al.* (1991) investigated the friction factor, inner wall surface roughness, and convective heat transfer coefficient for laminar and turbulent nitrogen gas flow in microtubes. The microtube inside diameter ranged from 3 μm to 81 μm . The experimental results indicated significant departures from the thermofluid correlations used for conventional-sized tubes. For microtubes having inside diameters smaller than 10 μm , the friction factor correlation, f^*Re , produced a value for the constant $C = 53$ rather than 64. The experimental results in turbulent flow indicated that traditional macro-scale assumptions, such as $J_H = f/8$ (the Colburn J factor), were not valid for microtubes having inside diameter less than 80 μm . The measured Nu numbers for convective heat transfer in microtubes for turbulent flow were as much as seven times the values predicted by the traditional macro scale analysis.

The experimental observations showed a slight increase in Nusselt number when compared to the Dittus-Boelter correlation for the turbulent flow. The measured heat transfer coefficients in laminar flow exhibited a Re number dependence, in contrast to the conventional prediction for fully laminar flow in which the Nu number is constant. The measured heat transfer coefficients in turbulent flow in microtubes were larger than predicted by conventional correlations for the smooth tubes. Neither the Colburn analogy nor the Petukhov analogies between momentum and energy transport were supported by the present data for microtubes. One suggested reason, as mentioned in fluid flow part, was the

suppression of the turbulent eddy motion in the radial direction as the diameters of the tubes are very small.

Choi, *et al.* (1992), performed an analysis to demonstrate that a liquid nitrogen cooled micro channel heat exchanger could be designed to maximise the heat transfer from silicon to the working fluid, to cool high-heat-load optical elements, like in the Advanced Photon Source (APS), a GeV third generation X-ray synchrotron radiation source. Insertion devices installed at the APS generate X-ray beams 10,000 times more intense than those generated by existing sources, but has an inherent problem of heat generation associated with it. The first optical element in the APS beam lines will absorb a tremendous amount of energy that is rapidly transformed to heat as it intercepts the beam. Therefore, cooling of the first optical element, with minimised flow induced vibrations is a critically important task. As silicon has a very high thermal conductivity at cryogenic temperatures, ten times greater than at the room temperature, allows the use of high aspect ratio silicon microchannels, in microchannel heat exchangers, that could lead to high heat removal rates, with sub cooled liquid nitrogen as the working fluid. Also, the thermal expansion coefficient of silicon at 125 K is zero, which is desirable as it significantly reduces the resultant strain in the first crystal due to thermally induced stresses, which acts to degrade the performance of an X-ray monochromator. Therefore the concept of microchannel cooling using cryogen appears to be ideal for cooling extremely high-heat-load X-ray optical elements.

The use of liquid nitrogen reduced the thermal resistance by a factor of nearly three when compared to water cooled sinks. It was predicted that a power density of 2000 W/cm² could be readily managed with the use of sub cooled liquid nitrogen in microchannel heat

exchangers. This heat removal rate is almost two orders of magnitude greater than that accomplished in pool boiling liquid nitrogen.

Peng and Wang (1993) conducted experimental investigations of the boiling characteristics of subcooled water flowing through microchannels with a rectangular cross-section of 0.6 x 0.7 mm. They found that the flow boiling and single-phase liquid convection characteristics are quite different from that of conventional cases. For single-phase liquid convection a steep increase in the heat flux was observed. The liquid subcooling and flow velocity affects the single-phase convection and the heat flux. They found that the single phase convective heat transfer for microchannels would be smaller than that for normally sized channels prior to the steep increase of heat flux, and become higher than that of ordinary cases after the steep increase. The nucleate boiling is greatly intensified, and the wall surface superheat for flow boiling may be much smaller than that of the normal case for the small wall heat flux. The velocity of the liquid subcooling appears to have no obvious effect on the flow nucleate boiling.

Peng, Peterson, Wang and others conducted experiments to investigate the heat transfer and flow characteristics of water flowing through rectangular microchannels having hydraulic diameter of 0.133-0.367 mm and H/W ratios of 0.333-1, machined on a stainless steel plate, to which a constant heat flux is applied. Their work can be summarized as follows:

1. The fluid flow and heat transfer characteristics in microchannels are different from the conventional sized channels. The laminar flow transition occurred at Reynolds Numbers of 200-700, and the flow became fully developed turbulent flow at Reynolds numbers of 400 -1500.

2. This critical Re for the laminar transition was strongly affected by the hydraulic diameter, decreasing with corresponding decrease in the microchannel dimensions and decreasing the transition range in magnitude.
3. For the laminar heat transfer regime, the Nusselt number was found to be proportional to $Re^{0.62}$ while the turbulent heat transfer case exhibited a typical relationship between Nu and Re , but with different empirical coefficients.
4. The friction behavior of both the laminar and turbulent flow was found to depart from the classical thermofluid correlations. The friction factor, f , was found to be proportional to $Re^{-1.98}$ rather than Re for the laminar condition, and proportional to $Re^{-1.72}$ for the turbulent flow.
5. The geometric parameters, hydraulic diameter, and H/W ratio were found to be the most important parameters and had a critical effect on the flow. They found that if the H/W ratio was increased the friction factor also increased. The reduction of the microchannel hydraulic radius decreases the friction factor significantly for a given H/W .
6. They found that there exists a special range of H/W , approximately 0.5, at which the experimental data are lower than the predictions obtained from classical correlations. Further reduction in the channel size increased the difference between the experimental and the theoretical friction factors at the critical Reynolds number, as the experimental value becomes smaller around the 0.5 range and larger when the ratio is not in this range.
7. The transitions (from laminar to transitional and transitional to turbulent) are influenced by liquid temperature, velocity and microchannel size. They found that the range of

transition zone, and the heat transfer characteristics of both the transition and the laminar regimes, are strongly affected by the liquid temperature, liquid velocity and the microchannel size, and hence are not only dependent on the Re.

8. They found that transition existed when the wall temperature or heating rate was increased. This transition is induced by the variation in the liquid thermophysical properties, due to the rise of the liquid temperature in the microchannels.
9. Besides, the single phase forced convection and flow-boiling characteristics were different from those in normally sized tubes and the heat transfer was intensified. No apparent partial nucleate boiling existed for subcooled flow boiling i.e., fully developed boiling was induced much earlier in the microchannels. The nucleate boiling is intensified and the wall surface superheat for flow boiling may be significantly smaller in microchannels than in the normal case for a given wall heat flux.
10. They found that there exists a transition region for the single-phase flow through microchannels, beyond which the heat transfer coefficient is nearly independent of the wall temperature. They also found that the heat transfer performance of the microchannels increased as the liquid velocity and the number of channels on the plate increased.

Hahn *et al.* (1997) designed high powered multi-chip modules by employing the planar embedding technique and microchannel water heat sinks. High performance liquid coolers of size 2"x2" were fabricated by laser cutting of channels with a pitch down to 200 μm . The heat transfer coefficients of the heat sink were in the range of $(2-8) \times 10^4 \text{ W/m}^2\text{-K}$. The heat sinks were thermally characterized. The thermal resistance, temperature distribution and pressure drop were investigated as functions of power, water flux and

channel geometry. Thermal simulation was used to demonstrate the advantages of the planar embedding technology and to study the influence of various design parameters. They investigated four samples of heat sinks, varying the ratio of channel to fin width (0.3, 0.6, 1 and 3) at constant channel pitch of 400 μm and constant channel depth. The thermal resistance of the heat sinks was in the region between 0.025 and 0.032 K/W with no significant variation in the power range from 200 to 700 W. At constant volume flow rate for water the thermal performance improved with decreasing channel width. The temperature variation on the cold surface responded only slightly to the increase of power. A significant influence of water flow was found for both: thermal resistance and temperature variation. The thermal performance increases significantly up to a flow of 60 l/h.

Bowers and Mudawar (1994), conducted experimental study of critical heat flux, (CHF) in mini-channel (diameter = 2.54mm) and microchannel (diameter = 510 μm) heat sinks of 1cm heated length. Tests were performed on a range of inlet subcooling and flow rate. Key findings of their study are:

1. Flow boiling in mini- and micro-channel heat sinks is an effective means of achieving high heat fluxes ($>200 \text{ W/cm}^2$) coupled with low flow rates ($<65 \text{ ml/min}$) and low-pressure drop ($<0.35 \text{ bar}$).
2. CHF for mini- and micro-channel heat sinks is not a function of inlet subcooling at low flow rates due to the fluid reaching the saturation temperature a short distance into the heated section of the channel.

3. The homogeneous equilibrium model accurately predicted the pressure drop for flow boiling in miniature heat sinks at low flow rates. The major component of pressure drop was the acceleration, which accounted for roughly 90%.
4. The flow boiling performance of both the mini-channel and micro-channel heat sinks are superior to the comparable single-phase technology; however, the mini-channel clearly has the practical advantage over the micro-channel. Mini-channel CHF values as high as 200 W/cm^2 were achieved with a negligible pressure drop of less than 0.01 bar compared to 0.23 bar for the micro-channel. Furthermore, the mini-channel heat sink could be fabricated using conventional drilling while microchannel fabrication requires special technology and is more susceptible to flow clogging.

Flik *et al.* (1991) theoretically developed the regime maps showing the boundary between the macro-scale and micro-scale heat transfer regimes. The maps relate the smallest geometric dimension to the temperature for conduction in solids, to temperature and pressure for convection in gases, and to the temperature of the emitting medium for radiative transfer. They concluded that the thermal conduction in a layer is microscale if the layer thickness is smaller than 7λ , for the conduction across the layer and 4.5λ , for the conduction along the layer, where λ , is the mean free path of the dominant carrier of heat. The dimension, which separates the microscale and macro-scale regimes for conduction in solids, increases as the number density of impurities and defects increases. The micro-scale regime boundary for gas convection is linearly related to T/p and varies little among gases.

2.3 References

1. Abramson, H.A., (1934), 'Electrokinetic phenomena and their application to biology and medicine', Chemical Catalog Company, New York, USA

2. Adamson, A. W., (1990), 'Physical chemistry of surfaces,' John Wiley and Sons, Inc. New York
3. Anderson, J. L., and Koh, W., (1977), 'Electrokinetic parameters for capillaries of different geometries,' J. Colloid and Interface Science, Vol. 59, No. 1, pp. 149-158
4. Anderson, J.L. and Quinn, J.A., 1972, 'Ionic mobility in microcapillaries,' Faraday Transactions I, Vol. 68, pp. 744-748
5. Beir W, Kellar W, et al., (1990), 'Manufacturing and testing of compact micro heat exchangers with high volumetric heat transfer coefficients,' ASME DSC Vol 19, pp. 189-197
6. Bikerman, J. J., (1958), 'Surface chemistry,' Academic Press Inc., New York
7. Bitsanis, I., Somers, S.A., Davis, T.D., and Tirrel, M., (1990), 'Microscopic dynamics of flow in molecularly narrow pores,' J. Chem. Phys., Vol. 93, No. 5, pp. 3427-3431
8. Bowers, M.B. and Mudawar, I., (1994), 'High flux boiling in low flow rate, low pressure drop mini-channel and micro-channel heat sinks', Int. J. Heat Mass Transfer, Vol. 37, No. 2, pp. 321-332
9. Burgreen, D., and Nakache, F.R., (1964), 'Electrokinetic flow in ultra fine capillary slits,' J. of Phys. Chem., Vol. 68, No. 5, pp. 1084-1091
10. Burgreen, D., and Nakache, F.R., (1963), 'Electrokinetic flow in capillary elements,' ASD-TDR-63-243.
11. Chan D.Y.C., and Horn, R.G., (1985), 'Drainage of thin liquid films,' J. Chem. Phys. Vol. 83, No. 10, pp. 5311-5324
12. Choi US, Rogers CS, and Mills DSM, (1992), 'High performance microchannel heat exchangers for cooling high heat load X-ray optical elements,' ASME DSC Vol 40, pp. 89-93
13. Choi SB, Barren RR, and Warrington RO, (1991), 'Fluid flow and heat transfer in micro tubes,' ASME DSC Vol 40, pp. 89-93
14. Davis, J. T., and Rideal, E. K., (1961), 'Interfacial phenomena,' Academic Press Inc., New York
15. Debye, P., and Cleland, R.L., (1959), 'Flow of liquid hydrocarbons in porous vycor,' J. of Applied Physics, Vol. 30, No. 6, pp. 843-849
16. Debye, P. and Huckel, E., (1923), Physik. Z., Vol. 24, pp. 185-305

17. Derjaguin, B.V., Popovskif, Y.M., and Altoiz, B.A., (1983), 'Liquid crystalline state of the wall-adjacent layers of some polar liquids,' J. of Colloid and Interface Science, Vol. 96, No. 2, pp. 492-503.
18. Dukhin, S.S., and Derjaguin, B.V., (1974), 'Surface and Colloid Science: Electrokinetic Phenomena,' Ed. Matijevic, E., (Chapter I by Dukhin, S.S.); Vol. 7, John Wiley and Sons, New York, USA
19. Flik MI, Choi BI, and Goodson KE, (1991), 'Heat transfer regimes in microstructures', ASME DSC Vol-32, Micromechanical Sensors, Actuators, and Systems, pp. 31-47
20. Freundlich, H., (1909), 'Kapillarchemie,' Akademischer Verlag
21. Gee, M.L., McGuiggan, P.M., Israelachvili, J.N., and Homola, A.M., (1990), 'Liquid to solid like transition of molecularly thin films under shear,' J. Chem. Phys. Vol. 93, No. 3, pp. 1895-1906
22. Goldberg N (1984), 'Narrow channel forced air sinks,' IEEE Trans Composite Hybrids and Manuf, CHMT-7, pp. 154-159
23. Guoy, L., (1910), J. of Phys., No 9, p. 456.
24. Guvenc, M.G., (1985), 'V-groove capillary for low flow control and measurement,' Micromachinig and Micropackaging of Transducers, Elsevier Science Publishers, Amsterdam.
25. Hahn, R., Kamp, A., Ginolas, A., Schmidt, M., Wolf, J., Glaw, V., Topper, M., Ehrmann, O., and Reichl, H., (1997), 'High power multichip modules employing the planar embedding technique and microchannel water heat sinks', Thirteenth IEEE SEMI-THERM Symposium, pp. 49-56
26. Heinbuch, U., and Fisccher, J., (1989), 'Liquid flow in pores: Slip, no-slip or multilayer sticking,' Physical Review A, Vol. 40, No. 2, pp. 1144-1146
27. Helmholtz, H., (1879), Ann, No. 7, p. 337
28. Hess, S., Loose, W., (1989), 'Slip flow and slip boundary coefficients of a dense fluid via nonequilibrium molecular dynamics,' Physica A, Vol. 162, pp. 138-144.
29. Horn, R.G., Smith, D.T., and Hailer, W., (1989), 'Surface forces and viscosity of water measured between silica sheets,' Chem. Phys. Lets., Vol. 162, pp. 404-408
30. Israelachvili, J.N., (1986), 'Measurement of the viscosity of liquids in very thin films,' J. of Colloid and Interface Sciences, Vol., 110 No. 1, pp. 263-271

31. Keyes RW, (1984), 'Heat transfer in forced convection through fins,' IEEE Trans on Elec Dev, Vol ED-31, pp 1218-1231
32. Koplik, J., Banavar, J., and Willemsen, J., (1989), 'Molecular dynamics of Fluid flow at solid surfaces,' Physics of Fluids A1, pp. 99-128
33. Koplik, J., Banavar, J., and Willemsen, J., (1988), 'Molecular dynamics of Poiseuille flow and moving contact lines,' Physical Review Letters, Vol. 60, No. 13, pp. 1282-1285
34. Levine, S., Marriott, J. R., Neale, G., and Epstein, N., (1975), 'Theory of electrokinetic flow in fine cylindrical capillaries at high zeta-potentials,' J. Colloid and Interface Science, Vol. 52, No. 1, pp. 136-149
35. Matijevic, E., (Ed. Vol. 7), (1974), 'Surface and Colloid Science' Vol. 1-7, (Various Editors), A Wiley-Interscience Publication, John Wiley and Sons, New York, USA.
36. Migun, N.P., and Prokhorenko, P.P., (1987), 'Measurement of the viscosity of polar liquids in microcapillaries,' Colloid J. of the USSR, Vol. 49, No. 5, pp. 894-897
37. Nakagawa, S., Shoji S., and Esashi, M., (1990), 'A micro-chemical analyzing system integrated on silicon chip,' Proceedings IEEE: Micro Electro Mechanical Systems, Napa Valley CA (90CH2832-4)
38. Peng, X.F., Wang, B.X., Peterson, G.P., and Ma, H.B., (1995), 'Experimental investigation of heat transfer in flat plates with rectangular microchannels,' Int. J. Heat Mass Transfer, Vol. 38 No. 1 pp. 127-137
39. Peng X. F. and Peterson, G. P., (1995), 'The effect of thermofluid and geometric parameters on convection of liquids through rectangular microchannels,' Int. J. of Heat Mass Transfer, Vol. 38 No. 4, pp. 755-758
40. Peng, X. F and. Wang, B. X (1994), 'Cooling characteristics with microchanneled structures,' Enhanced Heat Transfer, Vol. 1 No. 4 pp. 315 326
41. Peng, X.F., Peterson, G.P, and Wang, B.X. (1994), 'Frictional flow characteristics of water flowing through rectangular microchannels,' Experimental Heat Transfer, Vol. 7, pp. 249-264
42. Peng X.F. and Peterson G.P and Wang, B.X. (1994), 'Heat transfer characteristics of water flowing through microchannels,' Experimental Heat Transfer, Vol. 7, 265-283

43. Peng, X F and Wang, B. X, (1993), 'Forced convection and flow boiling heat transfer for liquid flowing through microchannels,' *Int. J. Heat and Mass Transfer*, Vol. 36, No. 14, pp. 3421-3427
44. Pfahler, J.N., (1992), 'Liquid transport in micron and submicron size channels,' Ph.D. Thesis, Department of Mechanical Engineering and Applied Mechanics, University of Pennsylvania, USA.
45. Quincke, G. (1859), 'Pogg. Ann.,' No. 107, p.-1
46. Reuss, F.F., (1809), 'Memoires de la Society Imperiale des Naturalistes de Moscou,' Vol. P. 327. (Cited in Abramson (1934)).
47. Rice, C. L., and Whitehead, R., (1965), 'Electrokinetic flow in a narrow cylindrical capillary,' *J. of Phys. Chem.*, Vol. 69, No. 11, pp. 4017-4024
48. Samalam VK, (1989), 'Convective heat transfer in microchannels', *J. Elect. Mat.* Vol. 18, pp.611-617
49. Smoluchowski, M., (1903), *Krak. Anz.*, p. 182; also in Graetz, 'Handbuch der Elektrizitat und des Magnetismus,' Vol. 2, Barth, Leipzig, 1921, p.336
50. Thompson, P.A., and Robbins, M.O., (1990), 'Shear flow near solids: Epitaxial order and flow boundary conditions,' *Physical Review A*, Vol. 41, No. 12, pp. 6830-6837
51. Tuckerman, D.B., (1984), 'Heat transfer microstructures for integrated cooling,' Ph.D. Thesis, Stanford University, Stanford, CA
52. Tuckerman, D. B. and Pease, R. F. W., (1982), 'Optimized convective cooling using micromachined structures,' *Electrochemical Society Extended Abstracts*, Vol. 82, pp. 197-198
53. Tuckerman, D. B. and Pease, R. F. W., (1981a), 'High performance heat sinking for VLSI,' *IEEE Electron Device Letters*, EDL-2, pp. 126-129.
54. Tuckerman, D. B. and Pease, R. F. W., (1981b), 'Errata,' *IEEE Electron Device Letters*, EDL-2, p. 213.
55. Tuckerman, D. B. and Pease, R. F. W., (1981c), 'Ultrahigh thermal conductance microstructures for cooling integrated circuits,' *Proc. 32nd Electronics Components Conf.*, pp. 145-149
56. Weisberg A, Bau HH, and Zemel J, (1990), 'Micro heat exchangers,' *ASME DSC Vol 19*, pp 159-170.

57. Weisberg A, and Bau HH, (1992), ' Analysis of microchannels for integrated cooling,' Int. J. Heat and mass Transfer, Vol 35, pp 2465-2474.
58. Wang JH, Yeh HY, and Shyu RJ, (1991), 'Thermal hydraulic characteristics of micro heat exchangers,' ASME DSC Vol. 32, 331-339.

Chapter 3 Heat Transfer and Fluid Flow in Parallel Plate Microchannels: Theoretical

3.1 Introduction

A variety of high-density, high-power and high-speed microelectronic devices require high rates of heat removal. The rate of heat dissipation is expected to be of the order of 100 W/cm^2 , Lai et al. (1993). To operate the electronic device at an optimum temperature, it is necessary to develop efficient heat removal methods. One such method is to use microchannel heat sinks. A microchannel heat sink is a structure with many microscale channels of large aspect ratios built on the back of the microchip. A liquid is forced through these microchannels to carry away the energy.

The concept of the microchannel heat sinks was introduced by Tuckermann and Pease (1981). A detailed review of several other research works on microchannel heat sinks can be found elsewhere, Philips (1990). To design an effective heat sink it is necessary to understand the flow characteristics in microchannels. Only after obtaining the velocity distribution can the energy equation be solved to determine the heat transfer characteristics. However, conventional transport theories cannot explain many phenomena associated with the microscale flow. For example, Eringen (1964) proposed a theory, which states that fluid flow in microchannels will deviate from that predicted by Navier-Stokes equations. Pfahler (1992) measured the friction coefficient in microchannels, and found a significantly higher flow rate than expected for both isopropanol and silicon oil. His results indicate that the polar nature of the fluid may play a role in the change in the observed viscosity. Choi et al. (1991) measured friction factors in microtubes of inside diameters 3 to $81 \text{ }\mu\text{m}$ using nitrogen gas. They found that for

diameters smaller than 10 μm , the friction factor constant is $C_f = 53$, instead of 64. Harley and Bau (1989) measured the friction factor in channels of trapezoidal and square cross-sections. They found experimentally that C_f ranged from 49 for the square channels to 512 for the trapezoidal channels. Peng et al. (1994) found experimentally that transition to turbulent flow began at $\text{Re} = 200$ to 700, and that fully turbulent convective heat transfer was reached at $\text{Re} = 400$ to 1500. They also observed that transitional Re diminished as the size of the microchannel decreased. Wang and Peng (1994) concluded that these effects were due to large changes in the thermophysical properties of the liquid due to high heat fluxes in small channels.

One possible explanation for these observed effects is that they are largely due to the interfacial effects such as interfacial electric double layer (EDL). These interfacial effects are ignored in macroscale fluid mechanics. However, most solid surfaces have electrostatic charges, *i.e.* an electrical surface potential. If the liquid contains very small amounts of ions, the electrostatic charges on the solid surface will attract the counterions in the liquid to establish an electrical field. The arrangement of the electrostatic charges on the solid surface and the balancing charges in the liquid is called the EDL, as illustrated in Figure 3.1, Hunter (1981). Because of the electrical field, the ionic concentration near the solid surface is higher than that in the bulk liquid. In compact layer, which is about 0.5nm thick, the ions are strongly attracted to the wall surface and are immobile. In diffuse double layer the ions are affected less by the electrical field and are mobile. The thickness of the diffuse EDL ranges from a few nanometers up to several hundreds of nanometers, depending on the electric potential of the solid surface, the bulk ionic concentration and other properties of the liquid.

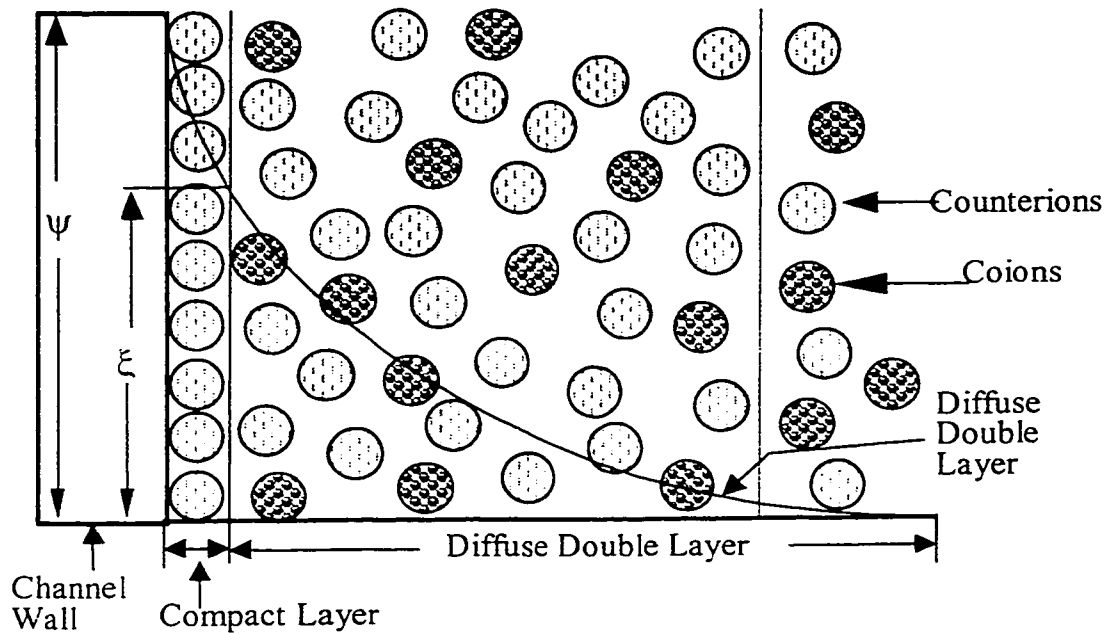


Figure 3.1: Schematic representation of the Electrical Double Layer at the Channel Wall.

When a liquid is forced through a microchannel under hydrostatic pressure, the ions in the mobile part of the EDL are carried towards one end. This causes an electrical current, called streaming current, to flow in the direction of the liquid flow. The accumulation of ions downstream sets up an electrical field with an electrical potential called the streaming potential. This field causes a current, called conduction current, to flow back in the opposite direction. When conduction current is equal to the streaming current, a steady state is reached. It is easy to understand that, when the ions are moved in the diffuse double layer, they pull the liquid along with them. However, the motion of the ions in the diffuse double layer is subject to the electrical potential of the double layer.

Thus, the liquid flow and associated heat transfer are affected by the presence of the EDL.

In macroscale flow, these interfacial electrokinetic effects are negligible as the thickness of the EDL is negligible compared to the hydraulic radius of the flow channel. However, in microscale flow the EDL thickness ($\sim 0.5 \mu\text{m}$) is comparable to the hydraulic radius of the flow channel. For submicron capillaries, the EDL thickness may be even larger than the radius of the capillary. Thus, EDL effects must be considered in the studies of microscale flow and heat transfer. There are few analytical studies in literature, which account for these effects on flow characteristics. Rice and Whitehead (1965) studied the effect of the surface potential on liquid transport through narrow cylindrical capillaries with the Debye-Huckel approximation to the surface potential distribution. Levine et al (1975) extended the Rice and Whitehead model to higher zeta potential by developing an analytical approximation to the solution of the Poisson-Boltzmann Equation.

3.2 Poisson-Boltzmann equation

Consider a fluid phase of infinite dilution containing positive and negative ions in contact with a planar positively charged surface. The surface bears a uniform electrostatic potential ψ_0 , which decreases as one proceeds out into the fluid, as shown in Figure 3.1. Far away from the wall, the concentration of the positive and negative ions is equal. The electrostatic potential ψ , at any point near the surface is related to the net number of electrical charges per unit volume ρ , in the neighborhood of the point, which measures the excess of the positive ions over negative ions or vice versa. According to the theory of electrostatics, the relation between ψ and ρ is given by the Poisson's Equation, which for a flat surface is, Hunter (1981)

$$\frac{d^2\psi}{dX^2} = -\frac{\rho}{\epsilon_o\epsilon} \quad (3.1)$$

The probability of finding an ion at some particular point will be proportional to the Boltzmann factor $e^{-ze\psi/k_bT}$. For the case of any fluid (1:1 electrolyte) consisting of two kinds of ions of equal and opposite charge z^+ , z^- , the number of ions of each type are given by the Boltzmann Equation

$$n^- = n_o e^{ze\psi/k_bT} \text{ and } n^+ = n_o e^{-ze\psi/k_bT}$$

The net charge density in a unit volume of the fluid is given by

$$\rho = (n^+ - n^-)ze = -2n_oze \sinh(ze\psi / k_bT) \quad (3.2)$$

Substituting Equation (3.2) in Equation (3.1), one obtains a non-linear second-order one-dimensional Poisson-Boltzmann Equation.

$$\frac{d^2\psi}{dX^2} = \frac{2n_oze}{\epsilon_o\epsilon} \sinh\left(\frac{ze\psi}{k_bT}\right) \quad (3.3)$$

Non-dimensionalizing the above Equation via

$$\bar{X} = \frac{X}{a}, \quad \bar{\psi} = \frac{ze\psi}{k_bT}, \quad \text{and } \bar{\rho}(\bar{X}) = \frac{\rho(X)}{n_oze} \quad (3.4)$$

a non-dimensional form of Equation (3.1) and Equation (3.3), after some simplification as:

$$\frac{d^2\bar{\psi}}{d\bar{X}^2} = -\frac{\kappa^2}{2} \bar{\rho}(\bar{X}) \quad (3.5)$$

$$\frac{d^2\bar{\psi}}{d\bar{X}^2} = \kappa^2 \sinh(\bar{\psi}) \quad (3.6)$$

Where $\kappa = (2n_o z^2 e^2 / \epsilon \epsilon_o k_b T)^{1/2}$ and $(a \kappa) = \kappa$. The quantity 'k' is called the Debye-Huckel parameter, while '1/k' is referred to as the characteristic thickness of the EDL.

3.2.1. Solution of the Poisson-Boltzmann equation

If the electrical potential is small compared to the thermal energy of the ions, *i.e.*, ($|ze\psi| < |k_b T|$) so that the exponential in Equation (3.6) can be approximated by the first terms in a Taylor series. This transforms Equation (3.6) to

$$\frac{d^2 \bar{\psi}}{d\bar{X}^2} = \kappa^2 \bar{\psi} \quad (3.7)$$

In the literature, this is called the Debye-Huckle linear approximation. The solution of the above Equation can easily be obtained. Consider a flow channel between two parallel plates as shown in Figure 3.2. If the electrical potential at the channel surface is small and the separation distance between the two plates is larger than the thickness of the EDL, so

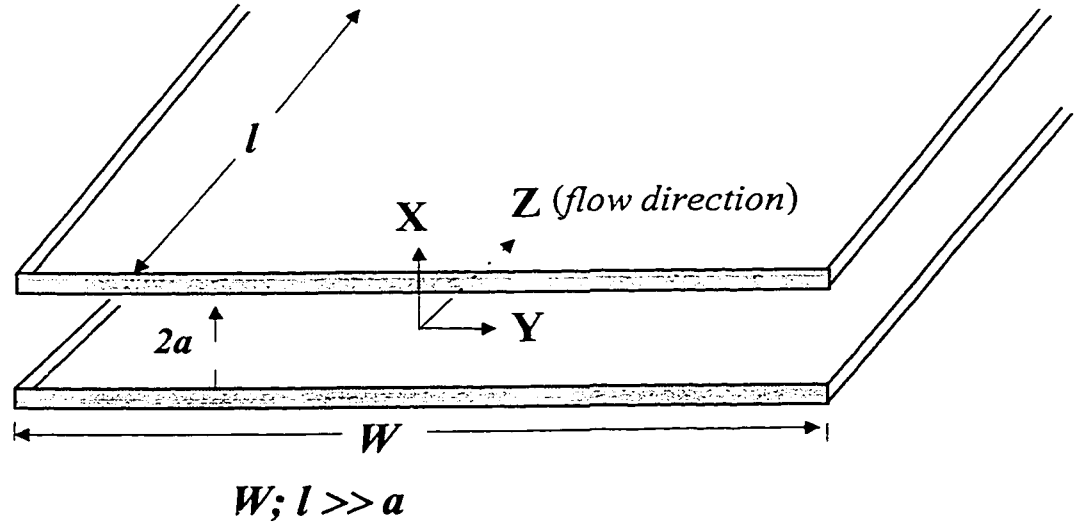


Figure 3.2: Schematic of a microchannel between two parallel plates that the EDLs near the two plates will not overlap, the appropriate boundary conditions are: at $\bar{X} = 0$, $\bar{\psi} \approx 0$ and at $\bar{X} \approx \pm 1$, $\bar{\psi} = \bar{\xi} = (ze\xi/k_b T)$. With these boundary conditions the solution is

$$\bar{\psi} = \frac{\bar{\xi}}{\sinh(\kappa)} |\sinh(\kappa \bar{X})| \quad (3.8)$$

3.3 Equation of motion

Consider a one-dimensional fully developed laminar flow through two parallel plates of unit width as shown in Figure 3.2. The forces acting on an element of fluid include the pressure force, the viscous force and the electric body force generated by the double layer electric field. The equation of motion is the Z-directional momentum equation.

$$\mu \frac{d^2 V_z}{dX^2} - \frac{dP}{dZ} - \rho(x) \frac{\partial \phi}{\partial Z} = 0$$

Where, ϕ is the potential at any point (X,Z). The last term represents the electrical body force term due to the presence of electrical double layer at the solid liquid interface. For a symmetrical (1:1) electrolyte flowing in a microchannel between two parallel plates, having a surface potential s , the total potential at a point (X,Z) is given as:

$$\phi = \phi(X, Z) = \psi(X) + [\phi_o - ZE_z]$$

Where,

$\psi(X)$ is the potential due to the double layer at the equilibrium state corresponding to no fluid motion and no applied external field

ϕ_o is the value of the imposed potential at $Z=0$

$\phi_o - ZE_z$ is the potential due to the field E_z in the absence of the double layer

E_z is the electrical field, constant (for fully developed flow field)

Therefore, after differentiating ϕ with respect to Z, the equation of motion is given as:

$$\mu \frac{d^2 \bar{V}_z}{d\bar{X}^2} - \frac{dP}{dZ} + E_z \rho(x) = 0 \quad (3.9)$$

Non-dimensionalize Equation (3.9) by making use of $\bar{E}_s = E_s / \xi$, $\bar{V}_z = V_z / V_o$. Where, V_o is arbitrarily chosen reference velocity. Replacing $\bar{\rho}(\bar{X})$ from Equation (3.5), and substitute in Equation (3.9) we obtain

$$\frac{d^2 \bar{V}_z}{d\bar{X}^2} + G_1 - \frac{2G_2 \bar{E}_s}{\kappa^2} \frac{d^2 \bar{\psi}}{d\bar{X}^2} = 0 \quad (3.10)$$

Where the two non-dimensional numbers are $\frac{a^2 P_z}{\mu V_o} = G_1$ and $\frac{\xi n_o z e a^2}{l \mu V_o} = G_2$. Note,

$E_z = E_s / l$ and let $P_z = -dP/dZ$. Integrating Equation (3.10) twice we get

$$\bar{V}_z + \frac{G_1 \bar{X}^2}{2} - \frac{2G_2 \bar{E}_s}{\kappa^2} \bar{\psi} = C_1 \bar{X} + C_2$$

The constants of integration C_1 and C_2 can be found by employing the appropriate boundary conditions, viz at $\bar{X} = \pm 1$, $\bar{V}_z = 0$, $\bar{\psi} = \bar{\xi}$. After evaluating the constants C_1 and C_2 , and substituting for $\bar{\psi}$ from Equation (3.8) the non-dimensional velocity distribution is:

$$\bar{V}_z = \frac{G_1}{2} (1 - \bar{X}^2) - \frac{2G_2 \bar{E}_s \bar{\xi}}{\kappa^2} \left\{ 1 - \left| \frac{\sinh(\kappa \bar{X})}{\sinh(\kappa)} \right| \right\} \quad (3.11)$$

3.4 The streaming potential

As seen from Equation (3.11), the velocity distribution can be calculated only if the streaming potential \bar{E}_s is known. As explained previously, in absence of an applied electric field when a liquid is forced through a channel under hydrostatic pressure an electrical field is generated. The potential of this electrical field is called the streaming potential, and is just sufficient to prevent any net current flow. Here, of course we do not

have an applied electric field, but an induced field. The total current I flowing through the microchannel is zero and is the sum of:

- (i) Current due to concentration gradient across the microchannel, I_n
- (ii) Current due to the fluid flow that is influenced by the pressure gradient and the imposed electric field, I_s , and
- (iii) Current due to the electric conductivity of the electrolyte solution within the microchannel, I_c .

As there is no concentration gradient, $I_n = 0$. The current due to the transport of charges by the liquid flow, called streaming current, is given by

$$I_s = \int_{A_c} V_z \rho(X) dA_c \quad (3.12)$$

After non-dimensionalizing V_z and $\rho(X)$ and substituting for $\bar{\rho}(\bar{X})$ from Equation (3.2), making use of the linear approximation, i.e. $\sinh(\bar{\psi}) = \bar{\psi}$, the nondimensional streaming current becomes

$$\bar{I}_s = \frac{I_s}{2V_o n_o z e a} = -2 \int_0^1 \bar{V}_z \bar{\psi} d\bar{X} \quad (3.13)$$

Substituting \bar{V}_z from Equation (3.11) and $\bar{\psi}$ from Equation (3.8), we obtain

$$\bar{I}_s = -2\alpha \left[\frac{G_1}{2} \{I_1 - I_2\} - \frac{2G_2 \bar{E}_s \bar{\xi}}{\kappa^2} I_3 + \frac{2G_2 \bar{E}_s \bar{\xi}}{\kappa^2 \sinh(\kappa)} I_4 \right] \quad (3.14)$$

where $\alpha = \bar{\xi} / \sinh(\kappa)$.

$$I_1 = I_3 = \int_0^1 \sinh(\kappa \bar{X}) d\bar{X} = \frac{\cosh(\kappa) - 1}{\kappa}$$

$$I_2 = \int_0^1 \bar{X}^2 \sinh(\kappa \bar{X}) d\bar{X} = \left(\frac{1}{\kappa} + \frac{2}{\kappa^2} \right) \cosh(\kappa) - \frac{2}{\kappa^2} \sinh(\kappa) - \frac{2}{\kappa^3}$$

$$I_4 = \int_0^1 \frac{\sinh^2(\kappa \bar{X})}{\sinh(\kappa)} d\bar{X} = \frac{\sinh(\kappa) \cosh(\kappa)}{2\kappa} - \frac{1}{2}$$

The streaming potential generated by the streaming current will produce a conduction current (which is the current due to the electric conductivity of the electrolyte) in the reverse direction, and is given by

$$I_c = \frac{E_s \lambda_o A_c}{l} \quad (3.15)$$

The electrical conductivity, λ_o is assumed constant. Non-dimensionalizing as before with $\bar{l} = l/a$, the non-dimensional conduction current is given by

$$\bar{I}_c = \frac{I_c}{\xi a \lambda_o} = \frac{\bar{E}_s \bar{A}_c}{\bar{l}} \quad (3.16)$$

At a steady state there will be no net current in the flow, i.e. $I_c + I_s = 0$. That is

$$\bar{I}_c + (2V_o n_o z e / \xi \lambda_o) \bar{I}_s = 0$$

Substituting for \bar{I}_c and \bar{I}_s from Equation (3.16) and Equation (3.14) the streaming potential is obtained as

$$\bar{E}_s = \frac{\alpha \kappa^2 G_1 G_3 (I_1 - I_2)}{\kappa^2 + 4 G_3 G_2 \xi \alpha \{I_3 - I_4 / \sinh(\kappa)\}} \quad (3.17)$$

Where the nondimensional factor $G_3 = \frac{V_o n_o z e l}{\xi \lambda_o}$.

3.5 Volume flow rate

The volume flow rate through the parallel plates can be obtained by integrating the velocity distribution over the cross sectional area, as

$$Q = \int_{A_c} V_z dA_c \quad (3.18)$$

In non-dimensional form, using Equation (3.11) the result is

$$\overline{Q} = \frac{2G_1}{3} - \frac{4G_2\overline{E}_s\overline{\xi}}{\kappa^2} + \frac{4G_2\overline{E}_s\overline{\xi}}{\kappa^3} \frac{(\cosh(\kappa) - 1)}{\sinh(\kappa)} \quad (3.19)$$

3.6 The electroviscous effect

As discussed previously, the EDL field at the solid surface exerts electrical forces on the ions in the liquid, and hence restricts the motion of these ions. Consequently the presence of the EDL field will reduce the liquid flow in comparison with the cases of no EDL effects. For steady flow under an applied pressure gradient (in the absence of an externally applied electric field), the volume flow rate is given by Equation (3.19). However, for flow between two parallel plates separated by a distance '2a' the volume flow rate can be written as

$$Q_p = \frac{2P_a a^3}{3\mu_a} \quad (3.20)$$

where μ_a , apparent viscosity, is introduced to account for the EDL effects. If the EDL effect is negligible then $\mu_a = \mu$. Non-dimensionalizing the volume flow rate and rearranging yields

$$\overline{Q}_p = \frac{2G_1\mu}{3\mu_a} \quad (3.21)$$

Equalizing Equation (3.19) with Equation (3.21), i.e. $\overline{Q} = \overline{Q}_p$, we obtain the ratio of the apparent viscosity to bulk viscosity.

$$\frac{\mu_a}{\mu} = \frac{\kappa^3 G_1}{\kappa^3 G_1 - 6G_2\overline{E}_s\overline{\xi}\kappa + 6G_2\overline{E}_s\overline{\xi}(\cosh(\kappa) - 1) / \sinh(\kappa)} \quad (3.22)$$

3.7 Friction constant

To calculate the friction constant, C_f , product of the friction factor and R_e the friction factor for flow between two parallel plates '2a' apart is given by

$$f = \frac{8\tau_w}{\rho_f V_{av}^2}$$

Where $V_{av} = \frac{Q}{A_c}$. The shear stress is given by

$$\tau_w = \left| \mu \frac{dV_z}{dX} \right|_{X=\pm a} = \left| \frac{\mu V_o}{a} \frac{d\bar{V}_z}{d\bar{X}} \right|_{\bar{X}=\pm 1}$$

Differentiating Equation (3.11) once and substituting for $(d\bar{V}_z/d\bar{X})$, we obtain with

$Re = \rho_f V_{av} a / \mu$ the friction constant C_f as

$$C_f = f Re = \frac{8V_o}{V_{av}} \left(G_1 + \frac{2G_2 \bar{E}_s \bar{\xi}}{\kappa} \coth(\kappa) \right) \quad (3.23)$$

3.8 Energy equation

Starting from the general form of the energy equation, performing an order of magnitude analysis to the fully developed flow in the microchannel produces Equation (3.24).

$$\rho_f c_p (V_z \frac{\partial T}{\partial Z}) = k_f (\frac{\partial^2 T}{\partial X^2} + \frac{\partial^2 T}{\partial Z^2}) + \mu (\frac{\partial V_z}{\partial X})^2 \quad (3.24)$$

With $\alpha_t = \frac{k_f}{c_p \rho_f}$, and $Pr = \frac{\mu c_p}{k_f}$, Equation (3.24) reduces to

$$V_z \frac{\partial T}{\partial Z} = \alpha_t \left(\frac{\partial^2 T}{\partial X^2} + \frac{\partial^2 T}{\partial Z^2} + \frac{Pr}{c_p} (\frac{\partial V_z}{\partial X})^2 \right) \quad (3.25)$$

Non-dimensionalize Equation (3.25) via

$$\bar{\alpha}_t = \frac{\alpha_t}{V_o a}, \quad \bar{V}_z = \frac{V_z}{V_o}, \quad \bar{Z} = \frac{Z}{a}, \quad \bar{X} = \frac{X}{a}, \quad \theta = \frac{T_w - T}{T_w - T_i}$$

$$\frac{\bar{V}_z}{\bar{\alpha}_t} \frac{\partial \theta}{\partial \bar{Z}} - (\frac{\partial^2 \theta}{\partial \bar{X}^2} + \frac{\partial^2 \theta}{\partial \bar{Z}^2}) + Br (\frac{\partial \bar{V}_z}{\partial \bar{X}})^2 = 0 \quad (3.26)$$

where $B_r = \text{Pr } E_c$ and $E_c = \frac{V_o^2}{c_p(T_w - T_i)}$

Equation (3.26) cannot be solved analytically. Therefore, a numerical solution is sought by using the central finite difference method. In the present work, it is assumed that both plates have constant and equal temperatures, and the inlet temperature of the fluid is known. The solution obtained leads to the temperature distribution in the X-Z plane of the channel.

3.8.1. Heat transfer coefficient

According to the energy balance,

$$-k_f \left. \frac{\partial T}{\partial X} \right|_{X=\pm a} = h(T_w - T_m) \quad (3.27)$$

$$\text{where } T_m = \frac{1}{V_{av} A_c} \int V_z T dA_c \quad (3.28)$$

Non-dimensionalizing Equation (3.27) we obtain

$$Nu = \frac{2ha}{k_f} = \frac{2}{\theta_m} \left. \frac{\partial \theta}{\partial \bar{X}} \right|_{\bar{X}=\pm 1} \quad (3.29)$$

where $\theta_m = \frac{T_w - T_m}{T_w - T_i}$. The derivatives $\left. \frac{\partial \theta}{\partial \bar{X}} \right|_{\bar{X}=\pm 1}$ are calculated numerically using the

standard three point formulae. Also the average Nusselt number is calculated as

$$Nu_{av} = \frac{1}{\bar{Z}} \int_0^1 Nu d\bar{Z} \quad (3.30)$$

3.9 Results and discussion

The mathematical model developed in the previous sections was applied to predict the fluid flow and heat transfer characteristics through a microchannel. Looking at

the preceding theory, one will find that in addition to the non-dimensional electrokinetic separation distance κ , three more non-dimensional parameters, G_1 , G_2 and G_3 , also play important roles in such a microchannel flow. $\kappa = (a/k)$ characterizes the ratio of the distance between the two plates to the double layer thickness and is a function of both the channel size and the fluid properties. $G_1 = a^2 P_z / \mu V_o$ represents the ratio of the mechanical force to viscous force. $G_2 = \xi n_o z e a^2 / l \mu V_o$ represents the ratio of EDL force to viscous force. $G_3 = V_o n_o z e l / \xi \lambda_o$ characterizes the ratio of the streaming current to conduction current. For given values of these three non-dimensional parameters an estimation of flow and heat transfer characterizing parameters such as velocity, streaming potential, ratio μ_s / μ , and Nu can be obtained.

To obtain an estimation of these parameters, consider fully developed laminar flow of an infinitely diluted, 10^{-6}M ($n_o = 6.022 \times 10^{20} \text{ m}^{-3}$) aqueous 1:1 electrolyte (e.g. KCl) solution through a microchannel. The separation distance is $25\mu\text{m}$ and the channel is 1 cm long. At room temperature, the physical and electrical properties of the liquid are $\epsilon = 80$, $\lambda_o = 1.2639 \times 10^{-7} \text{ (1/\Omega m)}$, $\mu = 0.90 \times 10^{-3} \text{ (kg/ms)}$. A pressure difference of $4.095 \times 10^5 \text{ Pa}$, and an arbitrarily chosen reference velocity $V_o = 1 \text{ m/s}$ are considered. With these, a set of values $G_1 = 5.009$, $G_2 = 7.95 \times 10^{-5}$, $G_3 = 1.6 \times 10^8$, and $\kappa = 40.8$ is obtained for a fixed value of $\xi = 50 \text{ mV}$. Predictions are made for velocity distribution, streaming potential, apparent viscosity and local and average Nusselt numbers.

3.9.1. Prediction of potential distribution

Equation (3.6) was solved with the linear approximation for the potential distribution of the solid-liquid interfacial EDL field. The solution Equation (3.8), gives very close values to the exact analytical solution for small electrostatic potentials at the

wall. A comparison of the potential distribution based on linear approximation with the exact potential distribution can be found elsewhere, (Hunter (1981), Adamson (1990)). The linear solution predicts slightly lower values of the potential at the wall compared to exact solution but at a small distance from the wall the two solutions overlap. The variation of non-dimensional potential distribution $\bar{\psi}$ with the nondimensional distance for various values of κ is shown in Figure 3.3. For any given electrolyte, a large κ implies either a large separation distance between the two plates or small EDL thickness. It can

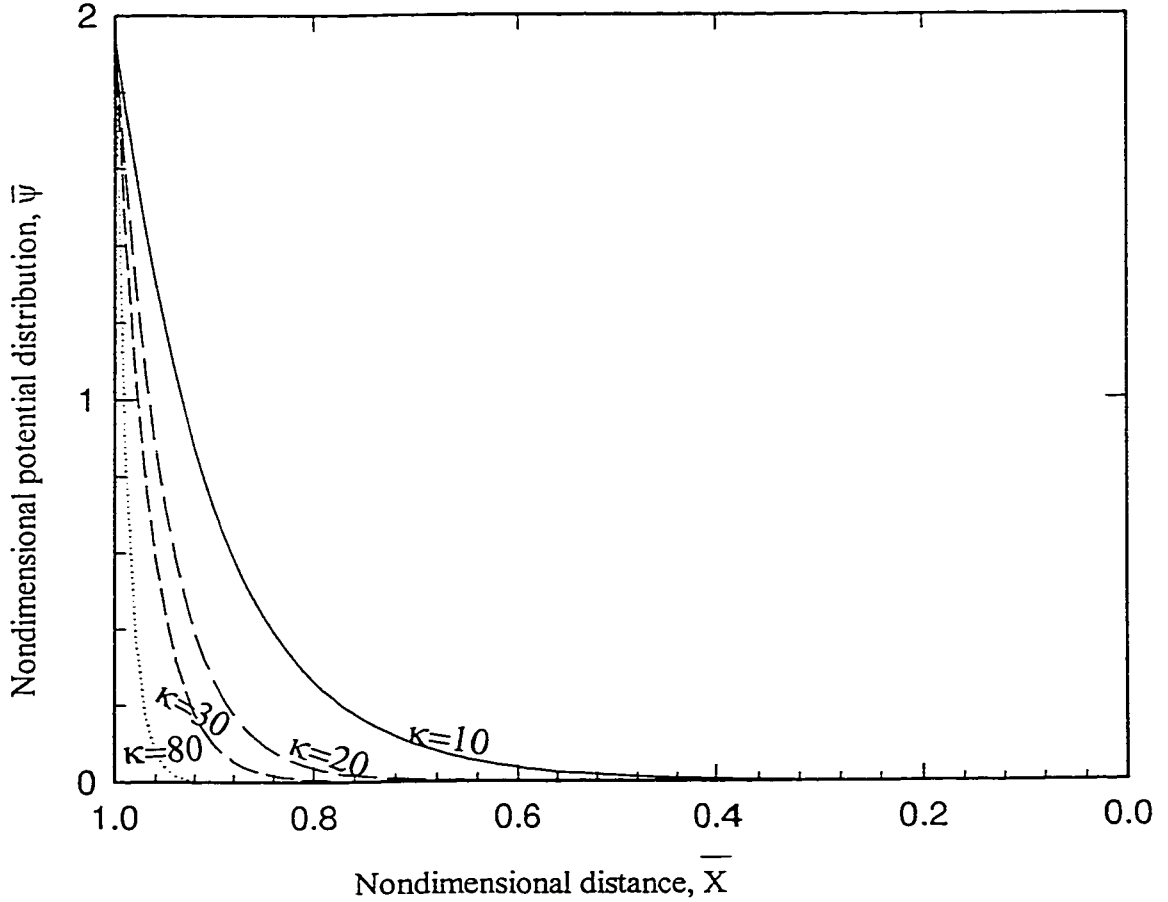


Figure 3.3: Nondimensional electrostatic potential distribution near the channel wall for $\xi=50\text{mV}$. $\bar{X}=0$, center of the channel, $\bar{X}=1$, the channel wall

be seen that as κ increases the double layer field exists only in the region close to the channel wall. For example, for $\kappa \approx 80$, the double layer occupies only 8% of the channel cross-sectional area. Therefore the smaller the κ the more predominant is the effect of the double layer field.

3.9.2. Velocity distribution and streaming potential

To obtain \bar{V}_z , \bar{E}_s is to be determined first. This can be calculated for any given values of G_1 , G_2 , G_3 , ξ and κ from Equation (3.17). As $G_1 \propto P_z$, thus a higher pressure implies a higher G_1 . $E_s \propto G_1$, thus the higher the pressure the higher the streaming potential. Figure 3.4, shows the variation of \bar{E}_s with G_1 for various values of κ and ξ . It is observed that as G_1 increases the streaming potential increases. Also for a given value

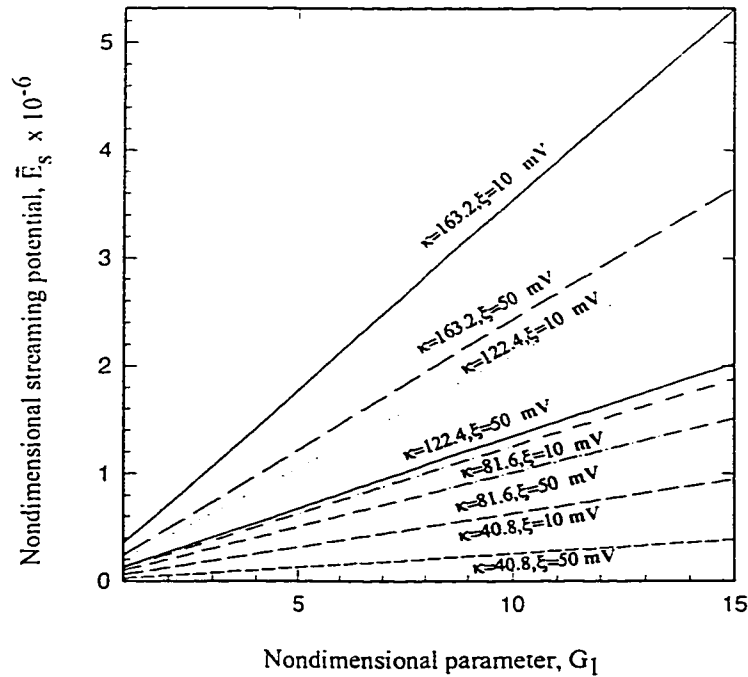


Figure 3.4: Nondimensional streaming potential variation with G_1 for various values of κ and ξ

of ξ , \bar{E}_s increases with κ . This is because, a larger electrokinetic separation distance corresponds to a large volume transport and thus more ions are carried to the end of the channel which result in higher charge accumulation. As seen from Figure 3.4 as ξ increases \bar{E}_s decreases. This is due to the strong effect of the double layer potential of the channel wall. If the zeta potential is higher, then more ions are attracted by the oppositely charged ions in the double layer and less ions are carried to the downstream with the flow; resulting in a lower charge accumulation at the ends of the channel.

For fixed values of G_1 , G_2 , G_3 , and ξ , the variation of velocity for different values of κ is shown in Figure 3.5. As seen, the velocity profiles are parabolic in shape and that

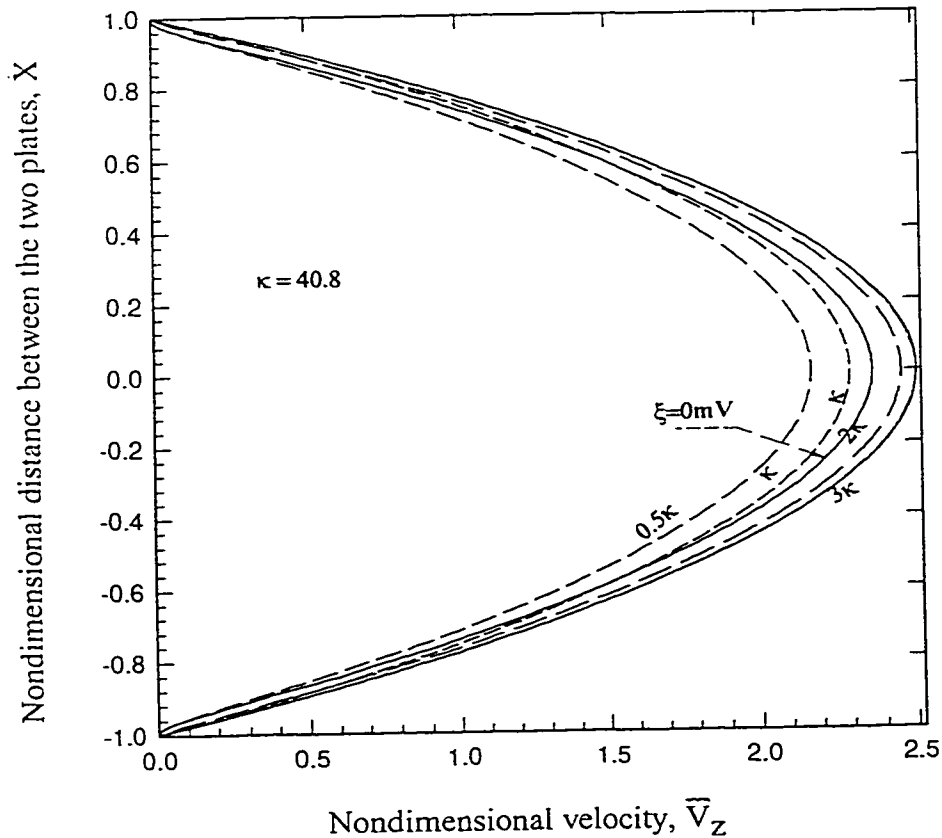


Figure 3.5 : Nondimensional velocity distribution for various κ and $\xi=50$ mV

as κ increases the velocity increases. The reason for this is that increasing κ implies either a large separation distance between the plates or a smaller EDL thickness resulting in larger portion of fluid not being affected by the EDL. However, if the EDL effect is absent ($\xi=0\text{mV}$, κ), Figure 3.5 shows that the velocity is higher than when it is present ($\xi=50\text{mV}$, κ). Thus the EDL modifies the velocity profile which would affect the pressure drop and heat transfer.

3.9.3. Predictions for friction constant

The product of the friction factor and Re as given by Equation (3.23) was computed for various values of ξ . Without considering the effects of the EDL the friction constant $C_f = 24$, as given by the conventional theory. But as can be seen from Figure 3.6, as ξ increases C_f also increases. For $\kappa=40.8$ at $\xi=100\text{mV}$, the value of the $C_f=28.22$. As

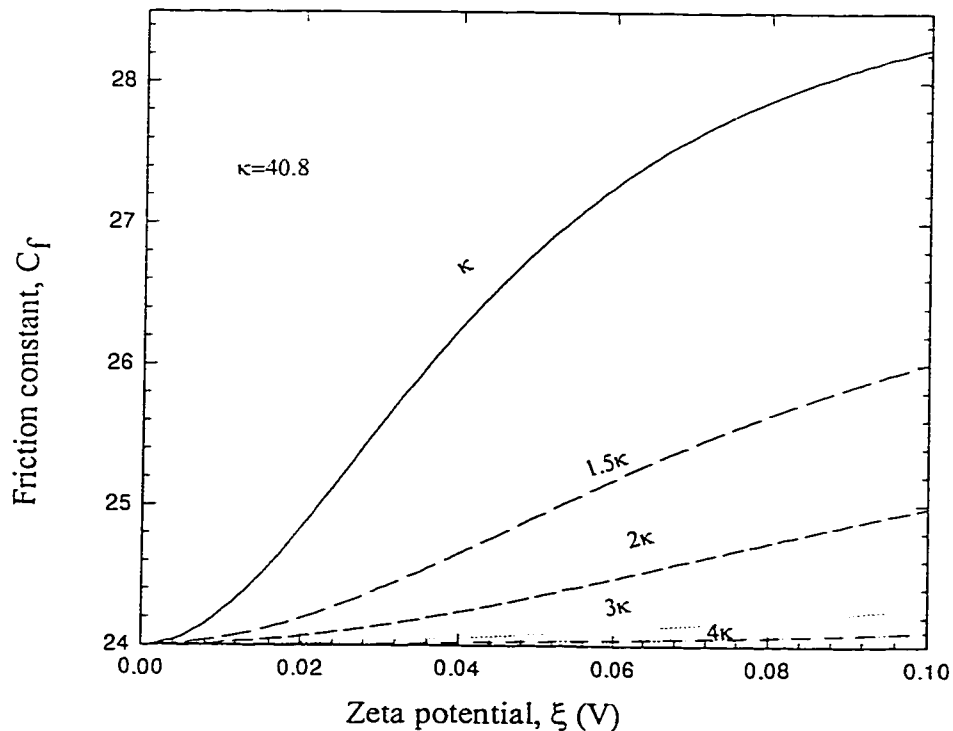


Figure 3.6: Variation of C_f with ξ for different values of κ

κ increases the values of C_f tend towards the conventional value of 24. For $\kappa = 163.2$, the maximum value of C_f at $\xi=100\text{mV}$ is 24.1. Therefore, for small κ the friction constant is higher depending on the zeta potential. Therefore, both the channel size and the fluid properties will affect the friction constant.

3.9.4. Predictions for apparent viscosity

As explained above, the streaming potential drives ions to move opposite to the flow direction and these moving ions drag the surrounding liquid molecules with them. This generates a reduced volume flow rate as given by Equation (3.19). Comparing this reduced volume flow rate with the flow rate derived by using conventional theory results in an apparent viscosity, that is greater than the bulk viscosity. Using Equation (3.22) the ratio of the apparent viscosity to the bulk viscosity, μ_a / μ , is plotted as a function of κ in Figure 3.7. It is observed that for $\xi=50\text{mV}$, the value of the ratio is approximately 3.75

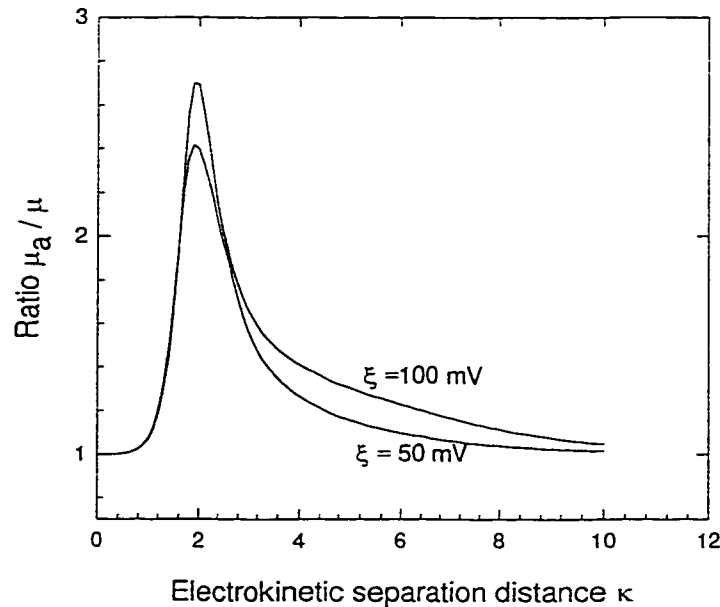


Figure 3.7: Variation of the ratio of apparent viscosity to bulk viscosity with electrokinetic separation distance, κ .

when $\kappa=2$, and then decreases as κ increases approaching a constant value equal to one for very large values of κ . For lower values of ξ the trend is the same except the value of the ratio is lower. This pattern has also been reported by Rice and Whitehead (1965) and Levine et al (1975).

3.9.5. Predictions for heat transfer

To predict the behavior of heat transfer in microchannels, the energy equation was solved numerically. Here, a hydrodynamically developed and thermally developing flow with constant and equal wall temperatures was considered. The EDL at the solid-liquid interface results in reduced velocity, which directly effects the heat transfer in the channel. To analyze the heat transfer behavior in microchannels it is important to consider the effect of Re on temperature profile at various cross-sections along the channel length. Figures 3.8a and 3.8b, show temperature profiles for Re=2.83 and Re=56.5, respectively. One can observe distinct difference in the two figures. At the entrance of the channel, marked as inlet in the figures, the temperature profiles are very steep compared to profiles at the exit. For Re=2.83, the temperature profile has a parabolic shape like the fully developed velocity profile. However, for Re=56.5, the temperature profile resembles a turbulent velocity profile shape. A steep temperature profile at the entrance implies a higher value of the derivative $\partial\theta/\partial\bar{X}$ at $\bar{X}=\pm 1$. In addition, θ_m is also maximum at the entrance of the channel. According to Equation (3.29), Nu has a maximum value at the channel entrance. Along the flow channel, both $\partial\theta/\partial\bar{X}$ at $\bar{X}=\pm 1$ and θ_m decrease. However, the value of the derivative $\partial\theta/\partial\bar{X}$ decreases much faster than θ_m , which results in a lower Nu. This can be seen in Figure 3.9, in which Nu is plotted for various values of κ and ξ along the channel length. For

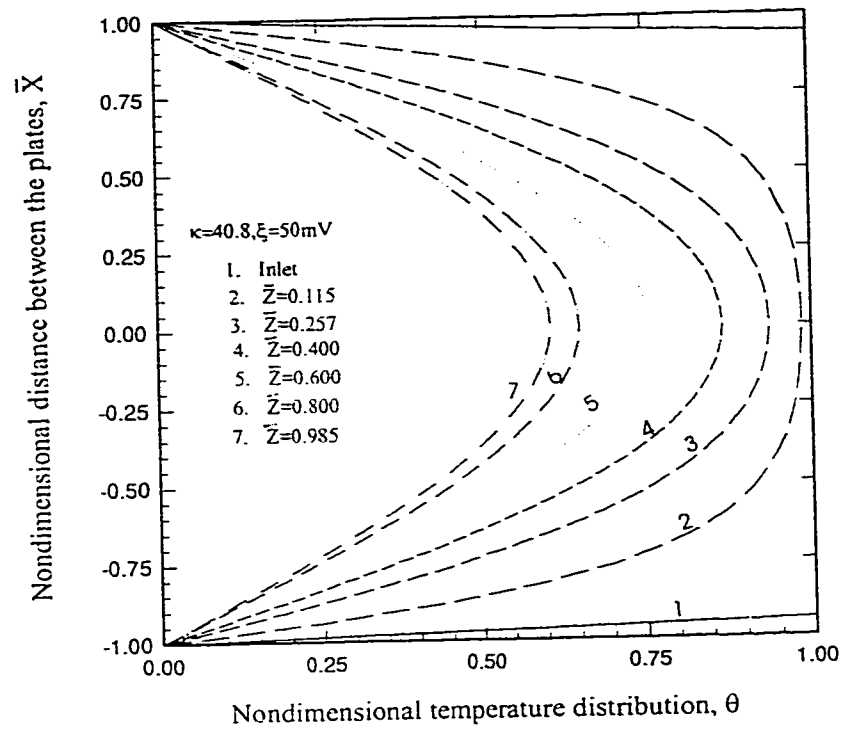


Figure 3.8a: Temperature profile at various cross-sections for $Re=2.83$

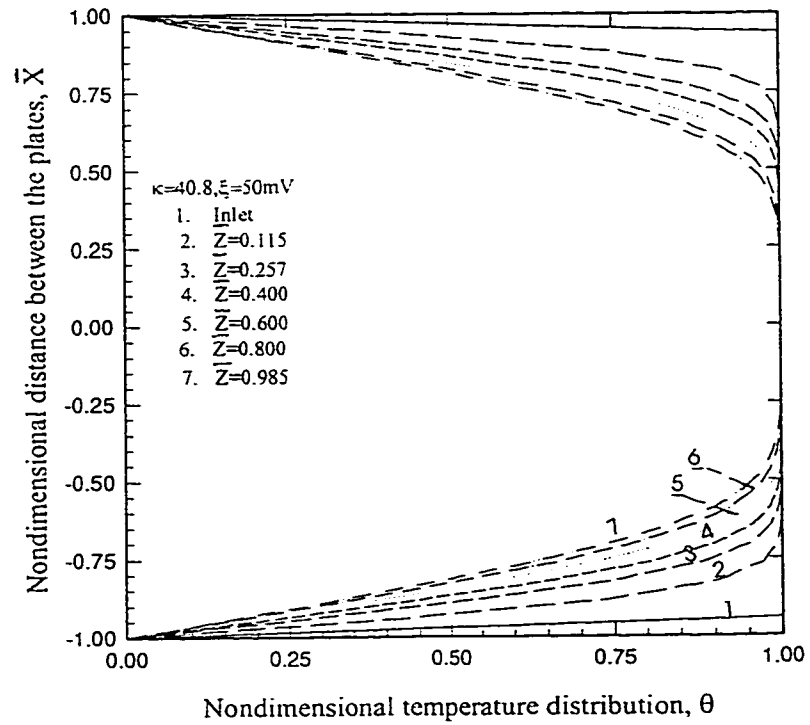


Figure 3.8b : Temperature profile at various cross-sections for $Re=56.5$

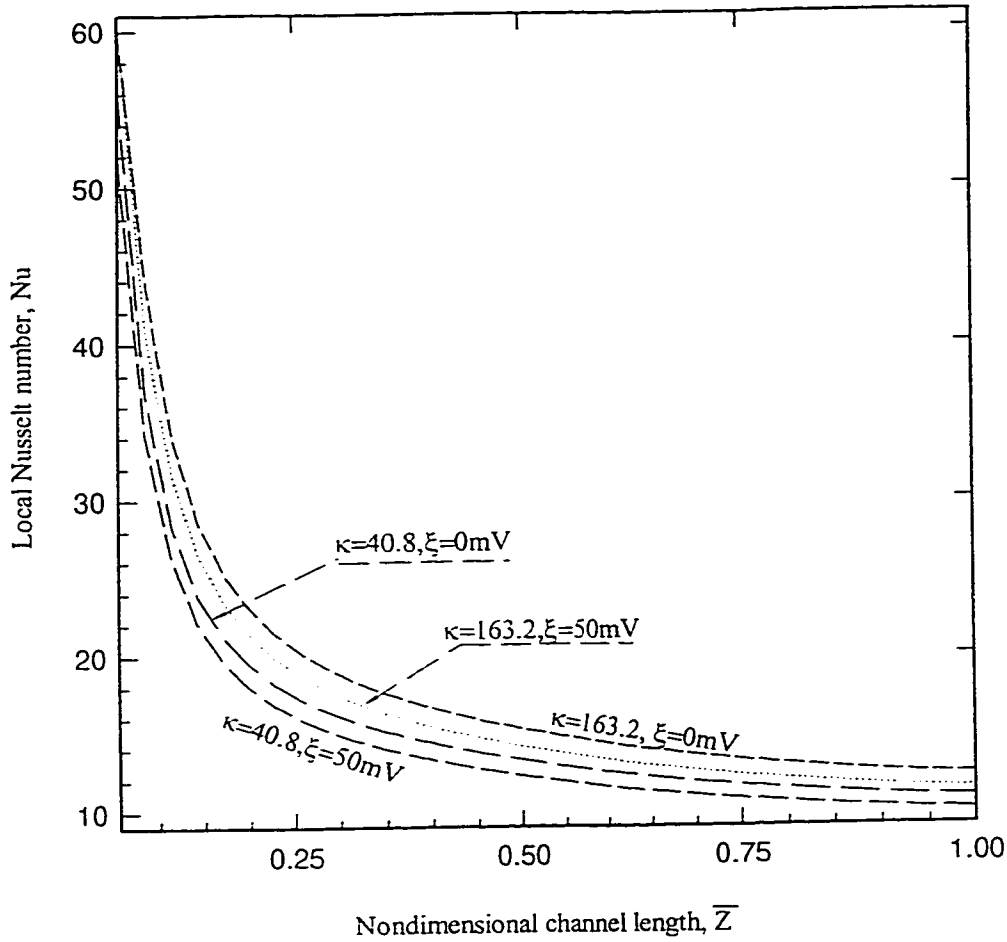


Figure 3.9: Variation of local Nusselt Number along the channel length

$\kappa=40.8$ and 163.2 if there are no double layer effects *i.e.*, $\xi=0$, a higher value of Nu , *i.e.*, higher heat transfer rate, is obtained. For the same value of κ , Nu decreases as ξ increases. As κ increases (for example, for the same channel size with a weaker EDL field or a smaller EDL thickness), the value of Nu increases as can be seen from Figure 3.9. The variation of the average Nusselt number, Nu_{av} as given by Equation (3.30), with the Reynolds number, Re , is shown in Figure 3.10. It is observed that as Re increases, the

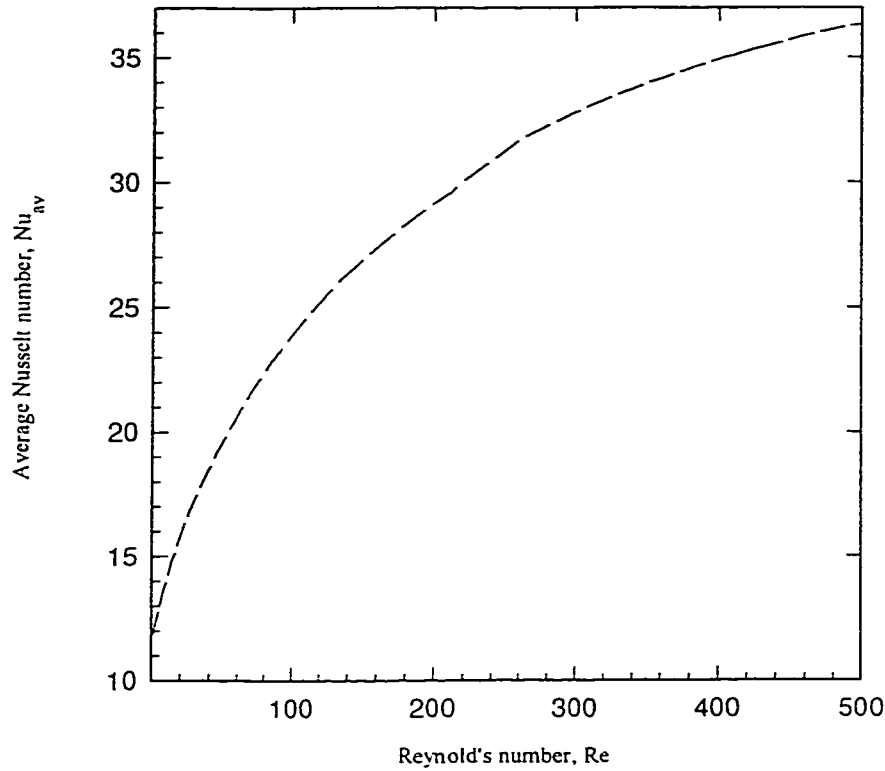


Figure 3.10: Variation of average Nusselt number with Reynold's for $\kappa=40.8$ and $\xi = 50\text{mV}$

Nu_{av} also increases. The above predictions are in agreement with the work of Wang and Peng (1994). Peng et al (1994), Wang and Peng (1994) and Peng et al (1995) showed experimentally that fluid properties and geometry of the microchannels all have significant influence on heat transfer performance and characteristics. As we have demonstrated in this work, the heat transfer dependence on fluid properties and on the channel's geometry may be understood as the EDL effects, as the parameters G_2 , G_3 and κ are functions of channel geometry and fluid properties. The EDL has a significant

effect on Nu and hence heat transfer rate. Without considering this effect, we may very well overestimate the heat transfer rate in microscale channels.

3.10. Summary

The effects of the EDL at the solid-liquid interface on liquid flows and heat transfer through a microchannel between two parallel plates was studied. Generally, the EDL near the channel wall tends to restrict the motion of ions and hence the liquid molecules in the diffuse EDL region. The induced streaming potential will drive the ions and hence the liquid molecules to move opposite to the flow direction. It is seen that for higher electrokinetic separation distance κ , the influence of the double layer is predominant only at the region near the channel wall. For small κ the double layers have a significant effect on the liquid flow. The streaming potential increases with an increase in κ , while it decreases for higher surface or zeta potentials. The EDL and the streaming potential act against the liquid flow resulting in a higher apparent viscosity. The apparent viscosity can be several times higher than the bulk viscosity of the liquid when the electrokinetic separation distance κ is very small. The heat transfer is also affected by EDL. The EDL results in a reduced velocity of flow than in conventional theory, thus affecting the temperature distribution and reducing the Reynolds number. It is seen that without the double layer a higher heat transfer rate is predicted, while as with a small zeta potential at the surface of the channel the heat transfer rate is comparatively smaller. Thus in our opinion it is very important to consider the effects of the EDL on liquid flows and heat transfer in microchannels. Otherwise, we would overestimate the fluid flow and heat transfer capability of the system.

3.11. References

1. Adamson A.W., (1990), *Physical chemistry of surfaces*, John Wiley, New York.
2. Choi S.B., Barron R.F. and Warrington R.O., (1991), Fluid flow and heat transfer in microtubes, *ASME Proc.* **32**, 123-134.
3. Eringen A., Simple microfluids, (1964), *Int. J. Eng. Sci.*, **2**, 205-217.
4. Harley J. and Bau H., (1989), Fluid flow in micron and submicron size channels, *IEEE Trans. THO249-3*, 25-28.
5. Hunter R.J., (1981), *Zeta potential in Colloid Science: Principles and Applications*, Academic Press New York.
6. Lai J., Carrejo J.P., and Majumdar A., (1993), Thermal imaging and analysis at submicrometer scale using atomic force microscope, *ASME-HTD* **253**, 13-20.
7. Levine S., Marriott J.R., Neale G. and Epstein N., (1975), Theory of electrokinetic flow in fine cylindrical capillaries at high zeta potential, *J. Colloid Sci.*, **52**(1), 136-149.
8. Peng X.F., Peterson G.P. and Wang B.X., (1994), Heat transfer characteristics of water flowing through microchannels, *Experimental Heat Transfer*, **7**, 265-283.
9. Peng X.F., Wang B.X., Peterson G.P. and Ma H.B., (1995), Experimental investigation of heat transfer in flat plates with rectangular microchannels, *Int. J. Heat Mass Transfer*, **38** (1), 127-137.
10. Pfahler J.N., (1992), Liquid transport in micron and submicron channels, Ph.D. Thesis, University of Pennsylvania, PA
11. Philips R.J., (1990), Microchannel heat sinks, In *Advances in thermal modeling of electronic components and systems* (Edited by A. Bar-Cohen and A.D. Kraus), Vol. II Chap. 3. ASME Press, New York.
12. Rice C.L. and Whitehead R., (1965), Electrokinetic flow in narrow cylindrical capillaries, *J. Phys. Chem.* **69**, 4017-4023.
13. Tuckermann D.B., and Pease R.F.W., (1981), High performance heat sinks for VLSI, *IEEE Electron Device Let.* Vol-EDL-2 (5), 126-129.
14. Wang B.X. and Peng X.F., (1994), Experimental investigation on liquid forced convection heat transfer through microchannels, *Int. J. Heat Mass Transfer*, **37** (Suppl.1), 73-82.

Chapter 4 Flow Characteristics of Water Through a Microchannel Between Two Parallel Plates with Electrokinetic Effects

4.1 Introduction

Liquid flows through microchannels have wide industrial applications such as design of microfluidic systems and micro heat sinks. As characteristic dimensions of channels decrease to micrometer ranges, the fluid flow behavior in these microchannels is strongly influenced by the wall/ interfacial effects. The flow characteristics are different from the normal situation described by the Navier-Stokes Equations. For example, Eringen (1964) proposed a theory that states that fluid flow in micro-channels will deviate from that predicted by Navier-Stokes Equations. Tuckermann and Pease (1981, 1982) investigated experimentally and theoretically the fluid flow through microchannels. They found that the flow friction measurements were slightly higher than those predicted by the classical theories. Pfahler (1992) measured the friction coefficient in microchannels, and found a significantly higher flow rate than expected for both isopropanol and silicon oil. His results indicate that the polar nature of the fluid may play a role in the change in the observed viscosity. Choi *et al.* (1991) measured friction factor in microtubes of inside diameters 3 to 81 μm using nitrogen gas. They found that for diameters smaller than 10 μm , the friction coefficient C_f , product of the friction factor f and Reynolds number Re , was equal to 53 instead of 64. Harley and Bau (1989) measured the friction factor in channels of trapezoidal and square cross-sections. They found experimentally that the friction coefficient C_f ranged from 49 for square channels to 512 for the trapezoidal channels. Peng *et al.* (1994a, 1994b) and Wang and Peng

(1994) found experimentally that transition to turbulent flow began at $Re = 200$ to 700 , and that fully turbulent convective heat transfer was reached at $Re = 400$ to 1500 . They also observed that transitional Re diminished as the size of the microchannel decreased. Rice and Whitehead (1965) studied the effect of the surface electrical potential on liquid transport through narrow cylindrical capillaries with the assumption of the small surface electrical potential. Levine *et al.* (1975) extended the Rice and Whitehead model to higher surface electrical potential for flows in cylindrical capillaries.

In our previous work, Mala *et al.* (1996), the surface potential effects on flow characteristics in microchannels were studied theoretically. It was concluded that the effect of the electrical double layer (*EDL*) on velocity distribution, friction coefficient, apparent viscosity and heat transfer can not be neglected in microscale fluid flow and heat transfer. Most solid surfaces bear electrostatic charges *i.e.* an electrical surface potential. If the liquid contains very small amounts of ions, the electrostatic charges on the solid surface will attract the counterions in the liquid to establish an electrical field. The arrangement of the electrostatic charges on the solid surface and the balancing charges in the liquid is called the *EDL*. The *EDL* is composed of the compact layer and diffuse double layer. The compact layer is about $0.5nm$ thick. In the compact layer, the ions are strongly attracted to the wall surface and are immobile. In diffuse double layer the ions are affected less by the electrical field and are mobile. The thickness of the diffuse *EDL* generally ranges from a few nanometers up to several hundreds of nanometers, depending on the electric potential of the solid surface, the bulk ionic concentration and other properties of the liquid. The electrical potential at the boundary between the compact layer and the diffuse layer is called the zeta potential, ξ .

When a liquid is forced through a microchannel under hydrostatic pressure, the ions in the mobile part of the *EDL* are carried towards one end. This causes an electrical current, called streaming current, to flow in the direction of the liquid flow. The accumulation of ions downstream sets up an electrical field with an electrical potential called the streaming potential. This field causes a current, called conduction current, to flow back in the opposite direction. When conduction current equals streaming current a steady state is reached. It is easy to understand that, when the ions are moved in the diffuse double layer, they pull the liquid along with them. The motion of the ions in the diffuse double layer is subject to the electrical potential of the double layer and the streaming potential. Thus liquid flow characteristics are affected by the presence of *EDL*.

In macroscale flow, interfacial electrokinetic effects are negligible as the thickness of the *EDL* is negligible compared to the hydraulic radius of the flow channel. However, in microscale flow the *EDL* thickness may be comparable to the hydraulic radius of the flow channel. For pure water and pure oils, the thickness of *EDL* can be as large as several microns. Thus, *EDL* effect will be significant for flows in small microchannels. An experimental study of *EDL* effects on microchannel flows was undertaken recently and is reported in this chapter. The experimental results are compared with the results obtained from the developed mathematical model. Good agreement between the experimental and computed results has been found.

4.2 Mathematical model

In our experimental studies, the channels were made of glass and silicon. These glass and silicon plates are highly smooth and homogenous. The average surface roughness of these microchannel plates was measured at Alberta Microelectronic Center

with a surface Profilometer. The magnitude of the average roughness was found to be less than 10 nm. Therefore, the effects of surface roughness on flow in such microchannels were not considered. The mathematical model characterizing the fluid flow through a microchannel between two highly smooth parallel plates with only *EDL* effects is described in the following sections.

4.2.1 Poisson-Boltzmann equation

For a fluid phase, containing positive and negative ions in contact with a planar positively or negatively charged surface the *EDL* field distribution is given by the Poisson-Boltzmann equation as derived in last chapter, equations (3.1 to 3.8). For reference purposes only, the non-dimensional form of Poisson's equation, Poisson-Boltzmann equation and the solution of Poisson-Boltzmann are rewritten below.

Non-dimensional Poisson's equation:

$$\frac{d^2 \bar{\psi}}{d\bar{X}^2} = -\frac{\kappa^2}{2} \bar{\rho}(\bar{X}) \quad (4.1)$$

Non-dimensional Poisson-Boltzmann equation:

$$\frac{d^2 \bar{\psi}}{d\bar{X}^2} = \kappa^2 \sinh(\bar{\psi}) \quad (4.2)$$

For the condition of electrical potential being small compared to the thermal energy of the ions, *i.e.*, ($|ze\psi| < |k_b T|$) and the same boundary conditions as described in the previous chapter, the solution of the Poisson-Boltzmann equation is:

$$\bar{\psi} = \frac{\bar{\xi}}{\sinh(\kappa)} |\sinh(\kappa \bar{X})| \quad (4.3)$$

4.2.2 Equation of motion

Consider a one-dimensional fully developed, steady state, laminar flow through two parallel plates of unit width as shown in Figure 4.1. The equation of motion with the electrical body force term (due to the electrical double layer potential distribution at the solid liquid interface) has also been derived in chapter 3. As the geometry and the conditions are the remain same only the final solution is written below:

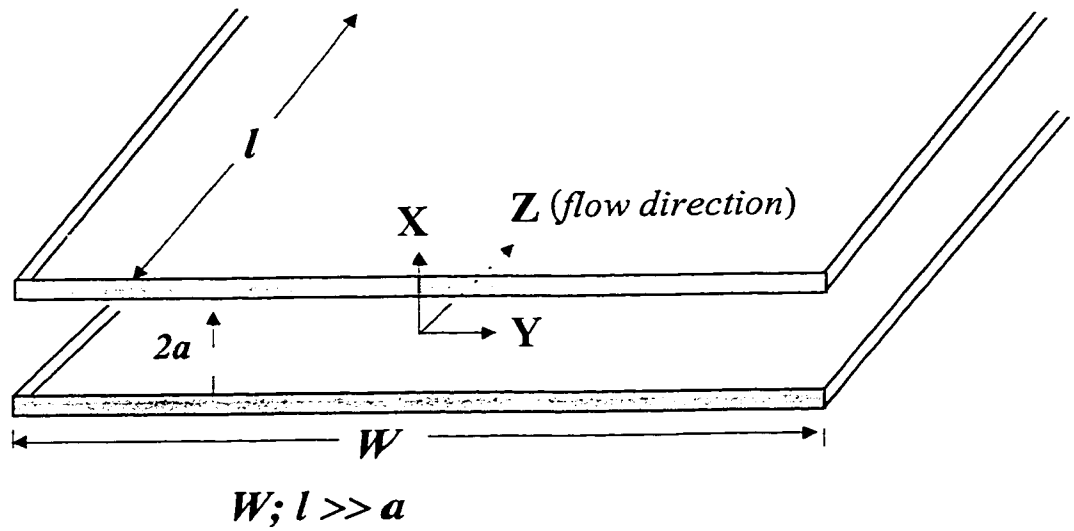


Figure 4.1: Schematic of a microchannel between two parallel plates

$$\bar{V}_z = \frac{G_1}{2}(1 - \bar{X}^2) - \frac{2G_2\bar{E}_s\bar{\xi}}{\kappa^2} \left\{ 1 - \frac{\bar{\psi}}{\bar{\xi}} \right\} \quad (4.4)$$

Substituting for $\bar{\psi}$ from Equation (4.3) the non-dimensional velocity distribution is:

$$\bar{V}_z = \frac{G_1}{2}(1 - \bar{X}^2) - \frac{2G_2\bar{E}_s\bar{\xi}}{\kappa^2} \left\{ 1 - \left| \frac{\sinh(\kappa\bar{X})}{\sinh(\kappa)} \right| \right\} \quad (4.5)$$

4.2.3 The streaming potential

As seen from Equation (4.5), the velocity distribution can be calculated only if the streaming potential \bar{E}_s is known. In absence of an applied electric field, when a liquid is forced through a channel under hydrostatic pressure an electrical field is generated as explained in the introduction. The potential of this electrical field is called the streaming potential. The current due to the transport of charges by the liquid flow, called streaming current, is given by

$$I_s = \int_{A_c} V_z \rho(X) dA_c \quad (4.6)$$

Nondimensionalizing V_z and $\rho(X)$ we obtain

$$\bar{I}_s = \frac{I_s}{2n_o V_o z e a} = \int_0^1 \bar{V}_z \bar{\rho}(\bar{X}) d\bar{X} \quad (4.7)$$

Substituting for $\bar{\rho}(\bar{X})$ from Equation (4.1), the nondimensional streaming current becomes

$$\bar{I}_s = -\frac{2}{\kappa^2} \int_0^1 \bar{V}_z d\left(\frac{d\bar{\psi}}{d\bar{X}}\right) = \bar{V}_z \left. \frac{d\bar{\psi}}{d\bar{X}} \right|_0^1 - \int_0^1 \frac{d\bar{\psi}}{d\bar{X}} d\bar{V}_z \quad (4.8)$$

With the boundary conditions viz. $\bar{X}=1, \bar{V}_z=0$ and $\bar{X}=0, d\bar{\psi}/d\bar{X}=0$, the first term on right hand side of Equation (4.8) becomes zero. Therefore, the streaming current reduces to

$$\bar{I}_s = \frac{2}{\kappa^2} \int_0^1 \frac{d\bar{\psi}}{d\bar{X}} d\bar{V}_z \quad (4.9)$$

Using Equation (4.4), Equation (4.9) can be written as:

$$\bar{I}_s = \frac{2}{\kappa^2} \left[-G_1 \int_0^1 \bar{X} d\bar{\psi} + \frac{2G_2 \bar{E}_s}{\kappa^2} \int_0^1 \left(\frac{d\bar{\psi}}{d\bar{X}} \right)^2 d\bar{X} \right]$$

the integrals are evaluated by using Equation (4.3) and are given as

$$\int_0^1 \bar{X} d\bar{\psi} = \bar{\xi} \left(1 - \frac{\cosh(\kappa) - 1}{\kappa \sinh(\kappa)} \right)$$

$$\int_0^1 \left(\frac{d\bar{\psi}}{d\bar{X}} \right)^2 d\bar{X} = \left(\frac{\kappa \bar{\xi}}{\sinh(\kappa)} \right)^2 \left(\frac{\sinh(\kappa) \cosh(\kappa)}{2\kappa} + \frac{1}{2} \right)$$

Finally, the nondimensional streaming current is given by

$$\bar{I}_s = -\frac{2G_1 \bar{\xi} \beta_1}{\kappa^2} + 4G_2 \bar{E}_s \beta_2 \left(\frac{\bar{\xi}}{\kappa \sinh(\kappa)} \right)^2 \quad (4.10)$$

Where $\beta_1 = 1 - \frac{\cosh(\kappa) - 1}{\kappa \sinh(\kappa)}$ and $\beta_2 = \frac{\sinh(\kappa) \cosh(\kappa)}{2\kappa} + \frac{1}{2}$

The streaming potential generated by the streaming current will produce conduction current in the reverse direction, and is given by

$$I_c = \frac{\lambda_b E_s A_c}{l} + \frac{\lambda_s E_s P_s}{l} \quad (4.11)$$

Where λ_b and λ_s are the bulk and surface conductivity respectively. I_c can be rewritten as

$$I_c = \frac{E_s A_c \lambda_r}{l}$$

$$\lambda_r = \lambda_b + \frac{\lambda_s P_s}{A_c} \quad (4.12)$$

Nondimensionalizing as before with $\bar{l} = l/a$, the nondimensional conduction current is

$$\bar{I}_c = \frac{I_c}{\xi \lambda_r a} = \frac{\bar{E}_s \bar{A}_c}{\bar{l}} \quad (4.13)$$

At a steady state, there will be no net current in the flow, i.e. $I_c + I_s = 0$. Using I_c from Equation (4.13) and I_s from Equation (4.7) we obtain after some simplification

$$\bar{I}_c + (2V_o n_o z e / \xi \lambda_r) \bar{I}_s = 0$$

Substituting for \bar{I}_c and \bar{I}_s from Equation (4.13) and Equation (4.10) the streaming potential is obtained.

$$\bar{E}_s = \frac{2G_1 G_3 \bar{\xi} \beta_1}{\kappa^2 + 4\beta_2 G_2 G_3 (\bar{\xi} / \sinh(\kappa))^2} \quad (4.14)$$

Where the non-dimensional factor $G_3 = V_o n_o z e l / \xi \lambda_\tau$.

In the classical theory of electrokinetic flow, the effect of *EDL* on the liquid flow and the effects of surface conductance are not considered. The streaming potential is related to the zeta potential and liquid properties through the following equation, Hunter (1981)

$$\frac{E_s}{\Delta P} = \frac{\varepsilon \varepsilon_o \xi}{\mu \lambda_\tau} \quad (4.15)$$

Equation (4.14) can be rearranged in a form similar to Equation (4.15) by substituting back the values of the nondimensional parameters, *i.e.*,

$$\frac{E_s}{\Delta P} = \frac{\varepsilon \varepsilon_o \xi}{\mu \lambda_\tau} \Phi \quad (4.16)$$

Where the correction factor Φ to the classical theory is given as

$$\Phi = \frac{\beta_1}{1 + \frac{\beta_2 \kappa^2 \varepsilon^2 \varepsilon_o^2 \xi^2}{\sinh^2(\kappa) a^2 \mu \lambda_\tau}} \quad (4.17)$$

If $\Phi = 1$ and $\lambda_\tau = \lambda_b$, Equation (4.16) becomes the classical equation.

4.2.4 Volume flow rate and apparent viscosity

The volume flow rate through the parallel plates can be obtained by integrating the velocity distribution over the cross sectional area, as

$$Q = \int_{A_c} V_z dA_c$$

Using Equation (4.5) the volume flow rate in non-dimensional form is

$$\bar{Q} = \frac{2G_1}{3} - \frac{4G_2\bar{E}_s\bar{\xi}}{\kappa^2} + \frac{4G_2\bar{E}_s\bar{\xi}}{\kappa^3} \frac{(\cosh(\kappa) - 1)}{\sinh(\kappa)} \quad (4.18)$$

For steady flow under an applied pressure gradient (without an externally applied electric field), the volume flow rate is given by Equation (4.18). This reduced rate of flow will results in an apparent viscosity $\mu_a (> \mu)$. As shown in chapter 3, equating the reduced volume flow rate as given by equation (4.18) with the conventional volume flow rate yields the ratio of apparent viscosity to bulk viscosity which is rewritten as under:

$$\frac{\mu_a}{\mu} = \frac{\kappa^3 G_1}{\kappa^3 G_1 - 6G_2\bar{E}_s\bar{\xi}\kappa + 6G_2\bar{E}_s\bar{\xi}(\cosh(\kappa) - 1) / \sinh(\kappa)} \quad (4.19)$$

4.2.5 Friction coefficient

The friction coefficient, C_f , is the product of the friction factor f and Re . The friction factor and the Re number for the flow between two parallel plates with a separation distance '2a' is given by

$$f = \frac{8\tau_w}{\rho_f V_{av}^2} \quad \text{and} \quad Re = \frac{\rho_f V_{av} a}{\mu}$$

Where $V_{av} = \frac{Q}{A_c}$. The shear stress is given by

$$\tau_w = \left| \mu \frac{dV_z}{dX} \right|_{X=\pm a} = \left| \frac{\mu V_o}{a} \frac{d\bar{V}_z}{d\bar{X}} \right|_{\bar{X}=\pm 1}$$

Differentiating Equation (4.5) once for $(d\bar{V}_z / d\bar{X})$, we obtain the friction coefficient C_f as

$$C_f = f Re = \frac{8V_o}{V_{av}} \left(G_1 + \frac{2G_2\bar{E}_s\bar{\xi}}{\kappa} \coth(\kappa) \right) \quad (4.20)$$

4.2.6 Experiments

The measurements of electrokinetic effects on liquid flows through microchannels between two parallel plates were conducted by using an electrokinetic analyzer (EKA) (A.Paar GmbH, Graz, Austria). Primary parameters measured by EKA are the pressure drop and the electrical potential across a channel (the streaming channel) through which a testing aqueous electrolyte solution flows. The measured electrical potential is the streaming potential. The streaming channels are made of the material to be investigated. In this study, the solid plates used to form the microchannels are P-type Silicon and 0211-Glass. All solid plates are 10 mm wide and 20 mm long. In each experiment, a pair (either silicon or glass) of plates were mounted parallel in a specially designed measuring cell (Institute of Polymer Research, Dresden, Germany) to form the streaming channel. Aqueous KCl solutions of several different concentrations and Millipore water were used in the measurements. The EKA performs the measurements automatically. In each measurement, a closed tubing circuit and a gearwheel pump circulate an electrolyte solution through the streaming channel under a constant pressure difference. The constant pressure difference (between 20 and 350 mbar) is kept for at least 60 seconds to ensure a steady state of the flow. The streaming potential is measured when the steady state is reached. Temperature, pH, volume flow rate, conductance of the solution, and the total electrical resistance of the streaming channel are also measured in each measurement. For a given pressure difference, a given channel height and a given ionic concentration, the above described measurement were repeated for at least three times. The accuracy of the measured data is better than 1%. All measurements were done at 25 °C.

4.3 Data analysis

The measured data included the total electrical resistance of the microchannels, the pressure drop, bulk conductivity, streaming potential and the flow rate.

4.3.1 Calculation of $\lambda_s P_s$

The product $\lambda_s P_s$ can be calculated from the measured electrical resistances from the following Equation

$$\frac{1}{R_T} = \frac{1}{R_b} + \frac{1}{R_s}$$

The surface and bulk electrical resistances in the above equation are given by $\frac{1}{R_s} = \frac{\lambda_s P_s}{l}$

and $\frac{1}{R_b} = \frac{\lambda_b A_c}{l}$, respectively. Thus, rearranging the above equation yields

$$\lambda_s P_s = l \left(\frac{1}{R_T} - \frac{\lambda_b A_c}{l} \right) \quad (4.21)$$

The total resistance R_T of the channel and the bulk conductivity λ_b are measured directly in the experiments. Once $\lambda_s P_s$ is known, the total conductivity λ_T can be calculated from Equation (4.12). Note that $\lambda_s P_s$ is constant for a given solid-solution system.

4.3.2 Determination of channel height and zeta potential

A difficulty encountered in this experiment is to measure accurately the distance between the plates, i.e. the channel height '2a'. If there is no (or negligible) *EDL* effect on the liquid flow, then the channel height can easily be determined from the measured volume flow rate by using the Poiseuille flow rate equation, Equation (4.25). This is the case for high concentration solutions or large flow channels, where the effect of the *EDL* is negligible. In the case of infinitely diluted solutions, like Millipore water, the *EDL* and

surface conductivity effects are significant. In this case, the flow rate is given by Equation (4.18). Equation (4.18) can be used to compute the actual channel height using two sets of experimental data of volume flow rate, pressure drop and streaming potential for a fixed microchannel height and solution concentration. For example, for Millipore water flowing through a silicon channel, two volume flow rates Q_1 and Q_2 corresponding to $\Delta P = 15$ kPa and $\Delta P = 35$ kPa are measured as 1.04×10^{-7} m³/s and 2.75×10^{-7} m³/s respectively. The corresponding streaming potentials are measured to be $E_{s1} = -0.4065$ V and $E_{s2} = -0.68705$ V. Once E_s , ΔP and Q are known, Equation (4.18) has two unknowns, the zeta potential ξ and the half channel height a (involved in the parameter κ). One should realize the fact that for a given solution and the solid plates (the channel walls) system, ξ is a constant, independent of the pressure difference and the channel height. Therefore, by equating ξ in the two-flow rate Equations, Q_1 and Q_2 , the half channel height can be determined by

$$a = \left(\frac{3l\mu}{2w} \frac{E_{s1}Q_2 - E_{s2}Q_1}{E_{s1}\Delta P_2 - E_{s2}\Delta P_1} \right)^{\frac{1}{3}} \quad (4.22)$$

From Equation (4.22) the channel height in the above example is 60.65 μ m. This value of channel height is used to calculate the ξ potentials from Equation (4.18). For a given solution and the solid plate system, only one channel height and the zeta potential is determined by using the flow rate Equation (4.18) as described above. Because once the zeta potential is known, the channel heights in all other cases of the same solid-liquid system can be determined from Equation (4.16) by using the measured E_s , ΔP and the liquid properties.

4.3.3 Total resistance, streaming potential and zeta potential

Figure 4.2 shows the variation of the measured total electrical resistance with the channel height for both P-type silicon and glass. For high ionic concentrations the resistance decreases as the channel height increases for the silicon channels whereas it remains approximately constant for the glass channels. For Millipore water, however, the resistance remains approximately same for the silicon channels but decreases for the glass channels. The resistance is much higher for glass surfaces than silicon surfaces as shown in the figure.

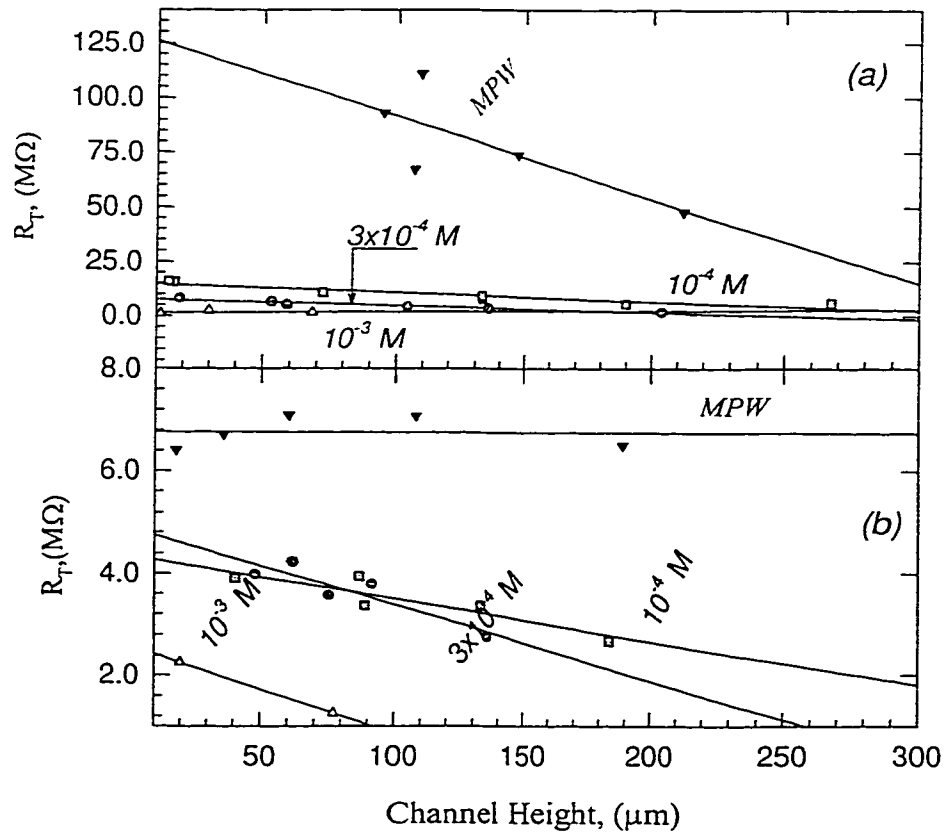


Figure 4.2: Variation of the channel's total electrical resistance with the channel height, (a): Glass and (b): Silicon channels

Figure 4.3 shows the variation of the measured streaming potential, E_s , with channel height for various ionic concentrations, and channel materials. It is observed that for Millipore water the streaming potential decreases rapidly as the channel height increases. The rate of decrease is more for glass than for P-type silicon. For solutions with higher concentrations the streaming potential remains approximately constant independent of the channel material and the channel height.

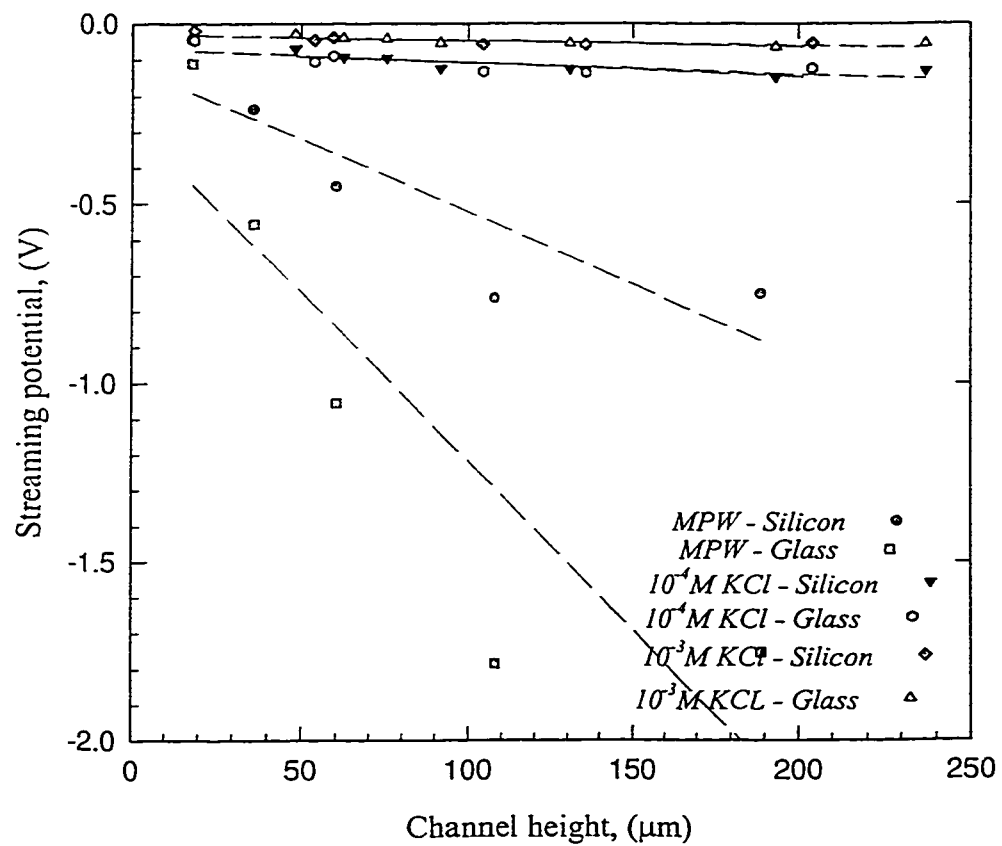


Figure 4.3: Variation of streaming potential with the channel height for various solution concentrations and channel materials

Figure 4.4 shows the variation of ξ with ionic concentration for silicon and glass surfaces. It is found that by considering the surface conductivity effect the values of ξ are significantly higher at low concentrations, especially for Millipore water. For P-type silicon, $\xi=12mV$ is obtained from the classical theory, *i.e.* Equation (4.15), which does not consider the effect of surface conductivity and the *EDL* effect on flow.. This value of ξ is significantly lower than $\xi=200.7mV$, obtained from Equation (4.16), which considers the effects of surface conductivity and the *EDL* effect on flow. Therefore, to estimate the correct value of ξ for solutions with low ionic concentrations, the *EDL* effect on flow and the surface conductivity should always be considered.

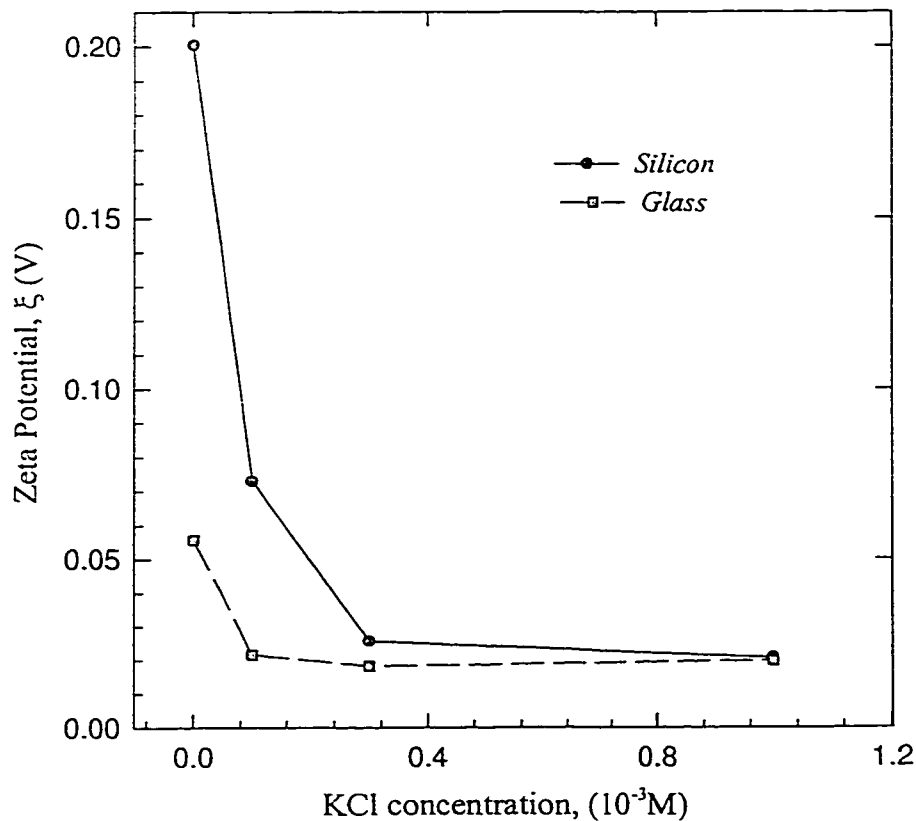


Figure 4.4: Zeta potential variation with ionic concentration for silicon and glass materials

4.4 Correction factor Φ

The correction factor Φ given by Equation (4.17), is computed for Millipore water. Figure 4.5 shows the variation of Φ with channel height. For high concentration solutions the value of electrokinetic separation distance κ ($\kappa = a/k$) is very large. This makes β_1 and the denominator of Equation (4.17) approaches unity as the concentration increases; therefore $\Phi=1$ for highly concentrated solutions. For Millipore water, which is infinitely diluted, the κ value is smaller and the values of Φ are significantly lower than

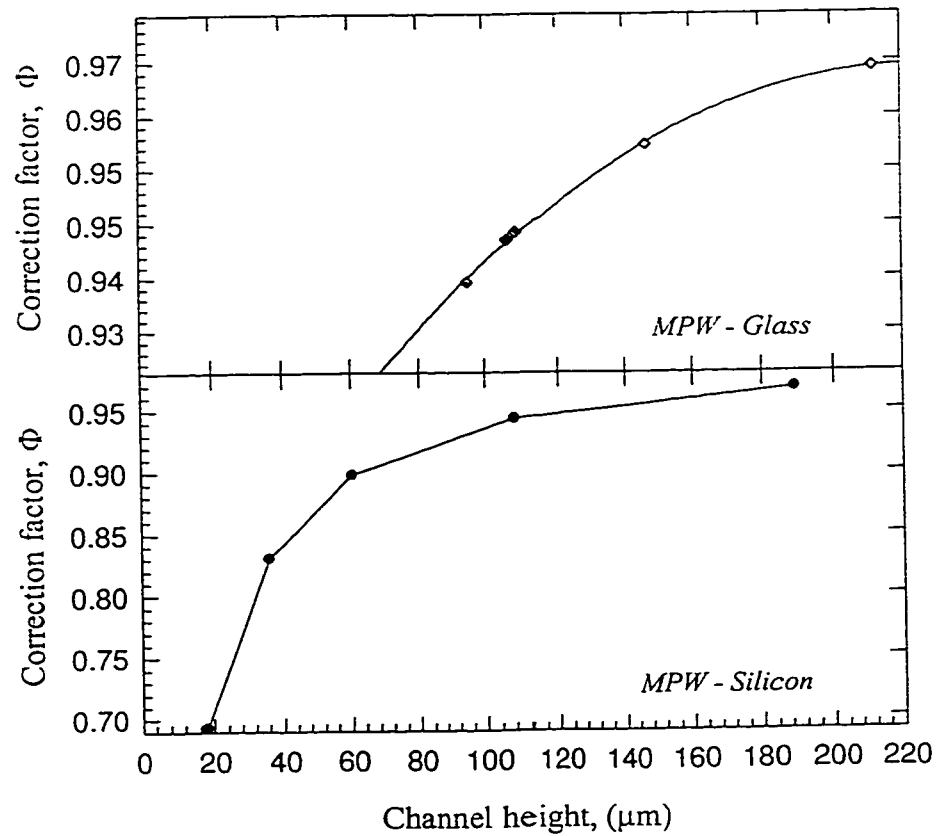


Figure 4.5: Variation of Φ with channel height for silicon and glass channels with Millipore water as the working fluid

unity. As can be seen from the Figure 4.5, for silicon channels Φ changes from 0.69 to 0.97 as the channel height increases. However, for glass channels, the values of Φ are much higher ranging from 0.91 to 0.98. This is because the silicon channels have higher zeta potential and lower total electrical resistance of the channel with the liquid than that of glass channels, as shown in Figures 4.2 and 4.4. Therefore, the classical equation, Equation (4.15), holds only for highly concentrated solutions and the correction should be applied if working with diluted solutions and “pure” liquids.

4.5 Volume flow rate

The volume flow rates have been measured in the experiments. In order to verify the model developed, the measured flow rates are compared with the prediction of Equation (4.18). Equation (4.18) gives the reduced volume flow rate due to presence of the *EDL* field. If the *EDL* effect is negligible such as in the case of high ionic concentration solutions, then the second and third terms on right hand side of Equation (4.18) vanish, resulting in the classical Poiseuille flow equation. Therefore, only Millipore water’s flow rates are compared with the predictions of Equation (4.18) as plotted in Figures 4.6a and 4.6b as a function of channel height and different pressure drop. It can be seen that the volume flow rates obtained experimentally and the theoretical predictions are in good agreement with each other. This indicates that the mathematical model developed in this study is correct. In Figure 4.6c the difference between the classical and reduced volume flow rates is shown. The difference is larger for silicon surfaces than for the glass surfaces. Also as the channel height increases the difference between the classical and reduced volume flow rates decreases, more so for

silicon than for glass. This is because the silicon surface has a higher zeta potential and surface conductivity than the glass surface.

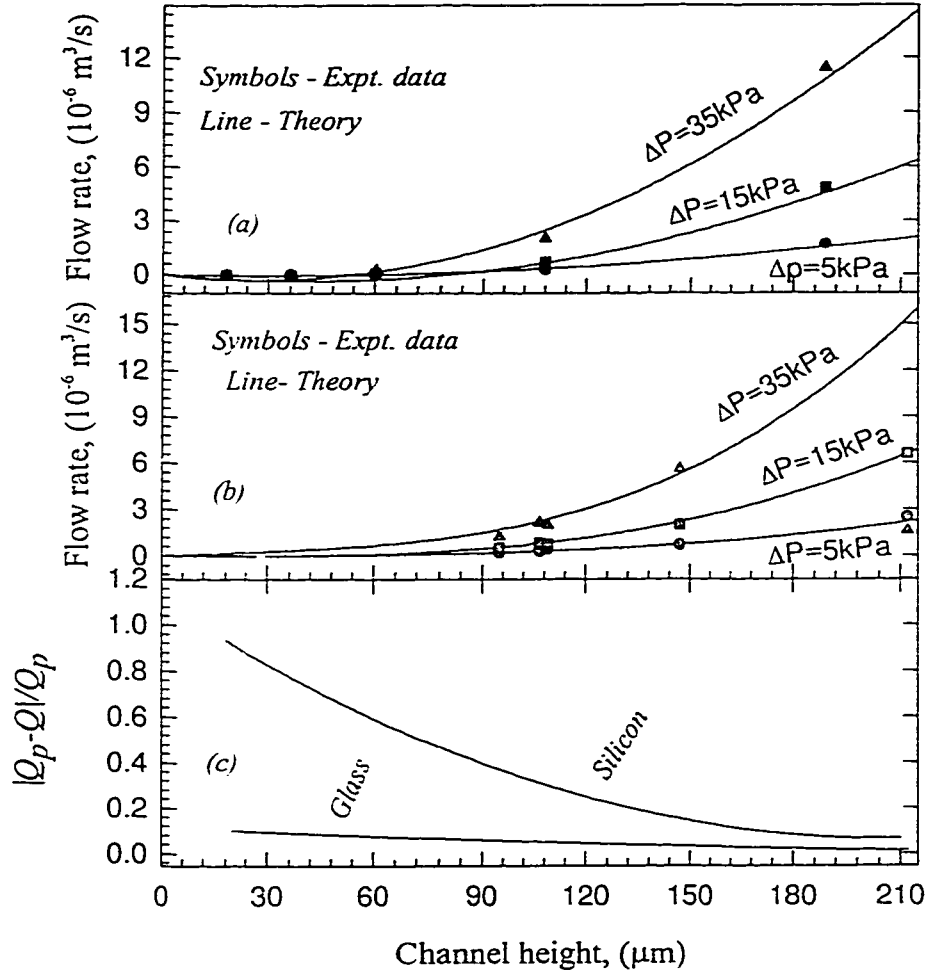


Figure 4.6: A comparison of volume flow rate of Millipore water between Experimental data and the predictions of equation (4.24) (a): in silicon channels (b): glass channels, and (c): predictions of equation (4.24) and (4.26)

4.6 Velocity distribution

The nondimensional velocity distribution \bar{V}_z in the microchannels can be computed by using Equation (4.5) and the data of the streaming potential, E_s , zeta potential ξ and the channel height. Figure 4.7 shows the nondimensional velocity

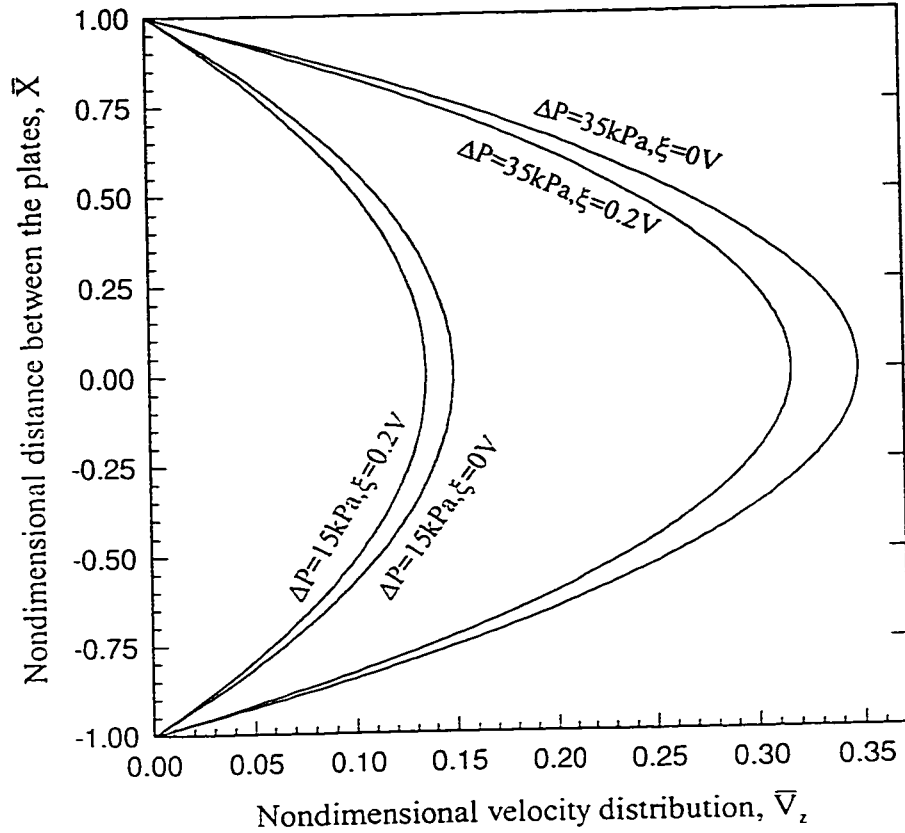


Figure 4.7: Nondimensional velocity distribution of Millipore water in a 20 μm channel for various ΔP and ξ .

distribution for a 20 μm silicon channel with Millipore water as the working fluid for two values of ΔP . As can be seen from the figure, the velocity profiles are parabolic in shape and that as ΔP increases the velocity increases. For the same values of ΔP the velocity is higher if $\xi=0V$ i.e. the *EDL* effect is absent, compared to when *EDL* effect is considered, i.e. for a finite value for ξ . Thus *EDL* effect results in a lower velocity compared to what is obtained by conventional theory.

4.7 Friction coefficient

The product of the friction factor f and Re as given by Equation (4.20) was computed for various values of ξ (20~200mV). We know from classical theory (no *EDL*

effect) that $C_f=24$ for channels between two parallel plates. Using Equation (4.20) and the measured experimental data C_f is calculated and is shown in Figure 4.8. For the case of small values of ξ and high ionic concentrations, the friction coefficient C_f is approximately 24. But as ξ increases and the ionic concentration decreases C_f also increases. For $\xi=200\text{mV}$ with Millipore water as the working fluid $C_f=24.56$. This may be understood as follows. As a liquid is forced through a microchannel under a pressure gradient, the charges in the mobile part of the double layer are carried downstream, and a streaming potential is established. This potential produces a backflow of ions and hence the liquid. The net result is a reduced flow in the forward direction. The liquid appears to

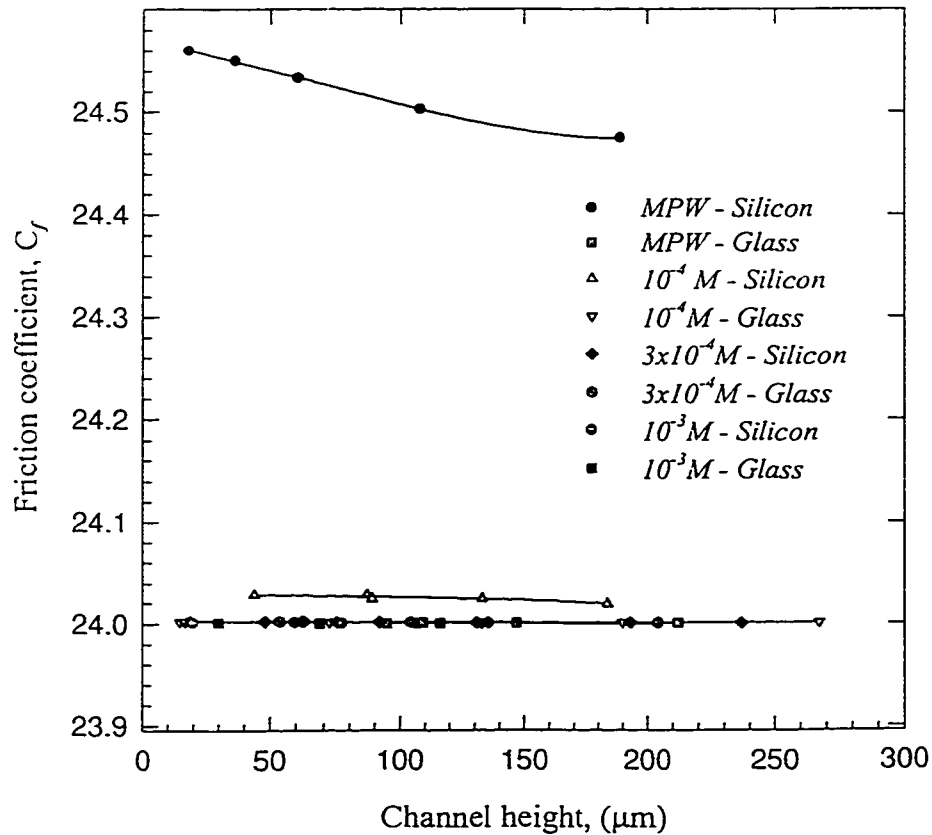


Figure 4.8: Variation of friction coefficient with channel height

exhibit an enhanced viscosity called apparent viscosity, if the flow rate is compared with the flow rate in the absence of the double layer effects. This apparent viscosity results in a higher friction coefficient. When the ionic concentration increases, the *EDL* field will be compressed, *i.e.*, the thickness of *EDL* field will be reduced. Therefore the value of friction coefficient is closer to 24 at higher ionic concentrations. For a given ionic concentration, the higher the ξ values, the stronger the *EDL* effect on flow, and hence the higher the friction coefficient value. As the channel height increases the friction coefficient value approaches the conventional value of $C_f=24$ as is shown in the figure. These results are qualitatively in agreement with the results obtained by Peng *et al.* (1994a) in their experiments through rectangular microchannels.

4.8 Concluding remarks

The effect of *EDL* at the solid-liquid interface on liquid flows through a microchannel between two parallel plates was studied experimentally and theoretically. Generally, the *EDL* near the channel wall tends to restrict the motion of ions and hence the liquid molecules in the diffuse *EDL* region. The induced streaming potential drives the ions and hence the liquid molecules to move in the opposite direction to the flow. The following conclusions can be drawn:

1. For solutions with high ionic concentrations, the thickness of the electrical double layer (characterized by the Debye-Huckel parameter, *i.e.*, $1/k$) is very small, normally a few nanometers. Therefore, the *EDL* effects on flow in microchannels are negligible. However, for infinitely diluted solutions such as the Millipore water used in this study, the thickness of the *EDL* is considerably large (about $1\mu\text{m}$). Therefore, the *EDL* effects on flows in microchannels become significant.

2. The theory developed in this work can describe the flow characteristics in microchannels, as supported by the good agreement between the flow rates measured in the experiments and that predicted by the theory. Overall, the volume flow rates for Millipore water are significantly lower than that predicted by the conventional fluid dynamics theory due to the *EDL* effects. The friction coefficient for flows in microchannels will increase as the zeta potential increases and as the ionic concentration decreases. However, from the experimental data and our model calculations, for microchannels with hydraulic diameters greater than few hundreds of micrometers the EDL effect would be negligible.

4.9 References

1. Choi, S.B., Barron, R.F. and Warrington, R.O., 1991, 'Fluid flow and heat transfer in microtubes', *ASME Proc.*, 32, 123-134
2. Eringen, A., 1964, 'Simple microfluids', *Int. J. Eng. Sci.*, 2, 205-217
3. Harley, J. and Bau, H., 1989, 'Fluid flow in micron and submicron size channels', *IEEE Trans.*, THO249-3, 25-28
4. Hunter, R. J., 1981, 'Zeta potential in Colloid Science: Principles and Applications', Academic Press New York, USA
5. Levine, S., Marriott, J. R., Neale, G. and Epstein, N., 1975, 'Theory of electrokinetic flow in fine cylindrical capillaries at high zeta potential', *J. Colloid Sci.*, 52(1), 136-149
6. Mala, G. M., Li, D. and Dale, J.D., 1996, 'Heat transfer and fluid flow in microchannels', *Int. J. Heat Mass Transfer*, (Accepted for Publication)
7. Peng, X. F., Peterson, G. P. and Wang, B.X., 1994a, 'Frictional flow characteristics of water flowing through rectangular microchannels', *Experimental Heat Transfer*, 7, 249-264
8. Peng, X. F., Peterson, G. P. and Wang, B. X., 1994b, 'Heat transfer characteristics of water flowing through microchannels', *Experimental Heat Transfer*, 7, 265-283

9. Peng, X. F., Wang, B. X., Peterson, G.P. and Ma, H. B., 1995, 'Experimental investigation of heat transfer in flat plates with rectangular microchannels', *Int. J. Heat Mass Transfer*, 38 (1), 127-137
10. Pfahler, J. N., 1992, 'Liquid transport in micron and submicron channels', Ph.D. Thesis, University of Pennsylvania, PA. USA
11. Rice C. L. and Whitehead, R., 1965, 'Electrokinetic flow in narrow cylindrical capillaries', *J. Phys. Chem.* 69, 4017-4023
12. Tuckermann, D. B. and Pease, R. F. W., 1981, 'High performance heat sinks for VLSI', *IEEE Electron Device Let.* Vol-EDL-2 (5), 126-129
13. Tuckermann, D. B. and Pease, R. F. W., 1982, 'Optimized convective cooling using micromachined structures', *J. Electrochem. Soc.* 129 (3), C98
14. Wang, B. X and Peng, X. F., 1994, 'Experimental investigation on liquid forced convection heat transfer through microchannels', *Int. J. Heat Mass Transfer*, 37 (Suppl.1), 73-82

Chapter 5 Flow Characteristics of Water in Microtubes

5.1 Introduction

Over the years, significant attention has been given to liquid flow in microchannels due to the development in microfluidic devices and systems. Components such as liquid cooled microchannel heat sinks, micro-pumps, micro-valves and actuators have been miniaturized, integrated and assembled forming various microfluidic devices and systems. The fundamental understanding of flow characteristics such as velocity distribution and pressure loss is essential in design and process control of microfluidic devices.

Peiyi and Little (1983) measured the friction factors for the flow of gases in fine channels, $130\ \mu\text{m}$ to $200\ \mu\text{m}$ wide. Their results showed different characteristics from that predicted by conventional theories of fluid flow. They attributed these differences largely to surface roughness of the microchannels. Wu and Little (1983, 1984) measured friction and heat transfer of gases in microchannels. They observed different experimental results of convective heat transfer from that obtained in conventional macroscale channels. They found that friction factors were larger than those obtained from the traditional Moody charts and indicated that the transition from laminar to turbulent flow occurred much earlier at Reynolds number of about $400\text{--}900$ for various tested configurations.

Tuckermann (1984) conducted one of the initial investigations of liquid flow and heat transfer characteristics in microchannels. He observed that the flow rates approximately followed Poiseuille flow predictions. Pfahler, et al (1990) conducted an experimental investigation of fluid flow in microchannels. They found that for large flow

channels the experimental observations were in rough agreement with the conventional theory whereas for small channels the deviations increased. Later, Pfahler (1991) presented measurements of friction factor or apparent viscosity of isopropyl alcohol and silicon oil flowing in microchannels. He observed that for larger channels the experimental results indicated a very good agreement with the predictions of classical theory. However, as the channel size decreased, the apparent viscosity began to decrease from the theoretical value for a given pressure drop, though distinctly different behaviors were observed between the polar isopropyl alcohol and non-polar silicon oil. Choi, et al (1991) investigated the friction factor, convective heat transfer coefficient and the effects of inner wall surface-roughness for laminar and turbulent flow in microtubes. Their experimental results were significantly different from the correlations in the conventional theories.

Wang and Peng (1994) experimentally studied the forced convection of liquid in microchannels, $0.2\text{mm}\sim 0.8\text{mm}$ wide and 0.7mm deep. They found that the transition from laminar to turbulent flow occurred when $Re < 800$, and that the fully developed turbulent convection was initiated in the Reynolds number range of $1000\text{--}1500$. Peng et al (1994a, 1994b) reported experimental investigation of forced flow convection of water in rectangular microchannels with hydraulic diameters ranging from 0.133 to 0.367 mm and aspect ratios from 0.333 to one . Their results indicated that the upper limits of the laminar flow and the beginning of the fully developed turbulent heat transfer regimes occurred at Reynolds number ranges of $200\sim 700$ and $400\sim 1500$, respectively. The transitional Reynolds number diminishes and the transition range becomes smaller as the

microchannel dimensions decrease. They found that the geometrical parameter such as height to width ratio also affects the flow characteristics in microchannels.

As the fluid flow characteristics in microchannels are quite different from those predicted by using the relationships established for macro-channels, it is therefore necessary to undertake fundamental investigations to understand the difference in these characteristics. The objective of this work is to investigate experimentally the characteristics of water flow in microtubes and attempt to explain the obtained results.

5.2 Experimental apparatus, procedure and results

The experimental apparatus is shown in Figure 5.1. The apparatus consists of a precision pump, a microfilter, a flow meter, a pressure transducer, tube inlet and outlet assemblies and a PC data acquisition system. The pump used is a high precision pump (*Ruska Instruments*) having a flow rate range of 2.5 to 560 ± 0.02 cc/hr. A 0.1-micron microfilter is placed between the pump and the microtube inlet to eliminate any particles and bubbles. Deionized water at room temperature is used as the working fluid. Two types of microtubes were used in this study, stainless steel (SS) (Small Parts Inc.) and fused silica tubes (FS) (Chromatographic Specialties). The pressure gauge and the pressure transducer measure the pressure inside the pump cylinder and the pressure across the microtube, respectively. During a run of the measurements, the pump is set to maintain a desired constant flow rate and the required pressure drop is measured. The flow rates were measured by three different ways: (1) read directly from the pump scale, (2) measured by the flow sensor, and (3) measured by collecting the liquid from the tube in specified time interval. The difference between the three flow rates was found to be less than $\pm 1.0\%$. For every measurement, pressure, time and flow-rate were measured and

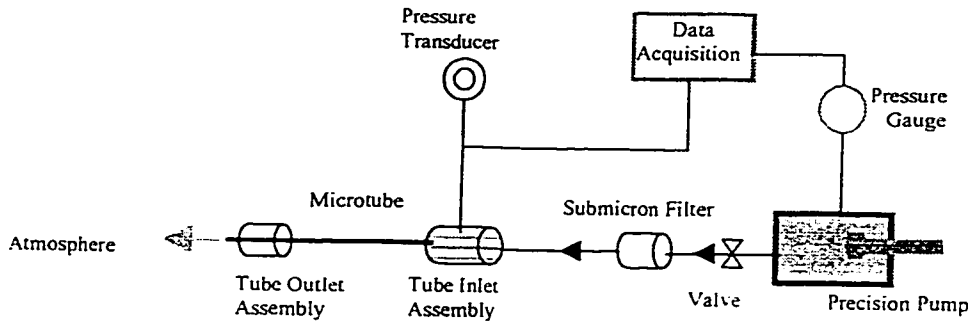


Figure 5.1: Schematic of experimental set up for flow in Stainless steel and Fused silica microtubes.

the data was acquired automatically by the data acquisition system. For every measurement, the flow was considered to have reached a steady state when the pressure drop value did not change any further. For smaller flow rates, it took longer time to reach a steady state compared to higher flow rates. At a steady state, the flow measurements were conducted for approximately 30 minutes. The data reported in this paper are for steady states. Each measurement was repeated at least three times.

The internal diameters of the microtubes used in this study range from $50\ \mu\text{m}$ to $254\ \mu\text{m}$, and the details are given in Table 5.1. The experiments were performed with various flow rates, which yield Re up to 2500. In each test, the flow rate was kept constant and the pressure difference required to force the liquid through the microtube was measured. From conventional theory the pressure drop-volume flow rate correlation is given by the Poiseuille flow equation:

Table 5.1: Dimensions of stainless steel and fused silica microtubes

Stainless Steel microtubes				Fused Silica microtubes			
Diameter $D \pm 2 \mu\text{m}$	$\text{Length of the tubes (cm)} \pm 0.005$			Diameter $D \pm 2 (\mu\text{m})$	$\text{Length of the tubes (cm)} \pm 0.005$		
	Shorter l_1	Longer l_2	Dif. Δl		Shorter l_1	Longer l_2	Dif. Δl
63.50	3.0	5.50	2.50	50.0	2.85	5.30	2.45
101.6	4.0	6.10	2.10	76.0	3.20	5.90	2.70
130.0	4.2	8.15	3.95	80.0	3.7	6.30	2.60
152.0	4.8	8.00	3.20	101.0	3.30	6.20	2.90
203.0	3.5	6.10	2.60	150.0	3.40	6.45	3.05
254.0	5.0	8.80	3.80	205.0	3.20	6.10	2.90
				250.0	3.10	6.20	3.10
Mean surface roughness of both the Stainless Steel and Fused Silica microtubes $\pm 1.75 \mu\text{m}$							

$$Q = \frac{\pi R^4}{8\mu l} \Delta P \quad (5.1)$$

Equation (5.1) is based on the assumption that the inlet and outlet losses are negligible. Therefore, to make an accurate comparison with the Poiseuille flow theory, the experimental pressure drop results should also be without any inlet and outlet losses. To achieve this, for every tube diameter, experiments were performed with two different tube lengths. The inlet and outlet losses are same for both lengths of the tubes as both have one end open to the atmosphere and the other is placed in the same inlet assembly. For the shorter tube, $l=l_1$, $\Delta P=\Delta P_1$, and for the longer tube, $l=l_2$, $\Delta P=\Delta P_2$. For two microtubes of the same material and diameter, the difference $\Delta P=(\Delta P_2 -\Delta P_1)$ can be obtained for the same flow rate. This ΔP should be the pressure drop required to force the liquid through a microtube of length $\Delta l=l_2 -l_1$ with no inlet and outlet losses.

In Figure 5.2, the experimentally measured value of the pressure gradient for each tube is plotted as a function of the Reynolds number for both *SS* and *FS* microtubes. The Reynolds number is related to the volumetric flow rate by:

$$Re = \frac{4}{\pi} \frac{Q}{Dv} \quad (5.2)$$

For graphical clarity, the error bars are shown only for some data points. The experimental results are also compared to the predictions of Poiseuille flow, Equation (5.1), shown by dotted lines in Figure 5.2.

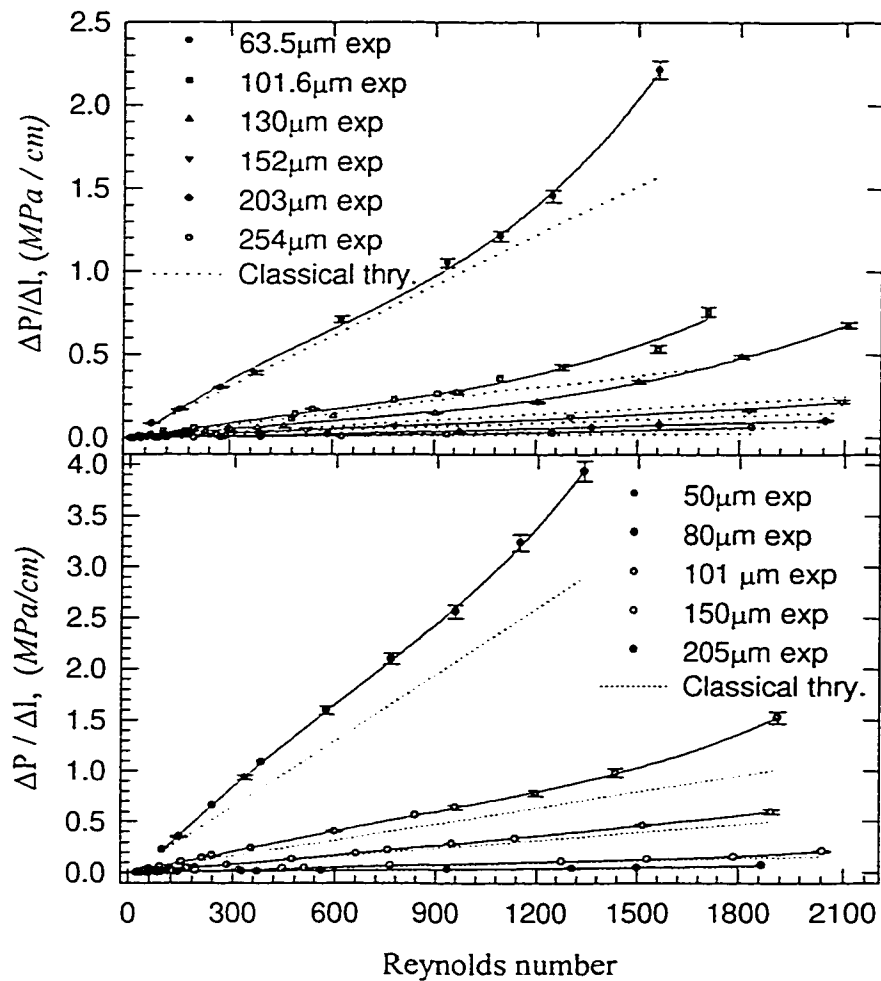


Figure 5.2: Experimentally measured pressure gradient $\Delta P / \Delta l$ vs Re for (a) Stainless Steel and (b) Fused Silica microtubes and comparison with the classical theory, Equation (5.1)

An uncertainty analysis of the experimental results was performed. The uncertainties in the microtube diameter, differential pressure and flow rate measurements were found to be less than $\pm 2\%$. The resulting maximum uncertainties for other parameters are: average velocity, $\pm 4.5\%$, Reynolds number, $\pm 3\%$, and friction factor $\pm 9.2\%$. The repeatability test showed that the maximum standard deviation was $\pm 2.5\%$ for the measured pressure drop.

From the conventional theory, the flow in a circular pipe driven by a pressure gradient is called the Hagen-Poiseuille flow. Under “usual” conditions, the critical Reynolds number based on the tube diameter is $Re_{crit} = 2300$, above which the flow is turbulent and below which the flow is laminar. However, this critical Reynolds number is influenced by external disturbances. If the flow is kept undisturbed, the flow can remain laminar for very large values of Reynolds number up to $50,000$, Hinze (1975). If finite amplitude disturbances are introduced, turbulence can occur for Re as low as about 2000 , as reported by Schlichting (1968). Below this value, the flow remains laminar even in the presence of very strong disturbances. Therefore, one would expect that, for laminar flow, *i.e.* $Re < 2000$, the experimental pressure drop-volume flow rate relationship be in a reasonable agreement with Equation (5.1).

As shown in Figure 5.2, the theoretical curves as predicted by Equation (5.1) are linear as expected, and fall below the experimental curves. For small Re (which implies small volumetric flow rate) the pressure gradient required is approximately equal to that predicted by Equation (5.1). As the Re increases, the measured pressure gradient is significantly higher than that predicted by Equation (5.1). The difference increases as the diameter of the tube decreases. The difference in pressure gradient is slightly larger for

the *FS* tubes than the *SS* tubes. In addition, for the same *Re*, the pressure gradient required for the microtubes with smaller diameters is significantly higher than that required for microtubes of larger diameters. Clearly, for both the *SS* and *FS* microtubes, the $\Delta P/\Delta l \sim Re$ relationship deviates from the conventional theory, and the deviation depends on the diameter of the microtubes. However, from Figure 5.2, the difference between the measured $\Delta P/\Delta l \sim Re$ relationships and the predictions of the conventional theory is less significant when the microtube diameter is above $150 \mu m$.

Then the question is, although the flow seems to be in the laminar range, why is there such a difference in the pressure drops between the experimental results and Equation (5.1). As per our understanding, there are at least two possible explanations. Either, the flow is not laminar *i.e.*, there is an early transition from laminar to turbulent flow, or the pressure difference is due to the surface roughness effects on microtube flow. In the case that the flow is not laminar, the Poiseuille Flow Equation can not be used, instead the full Navier-Stokes Equations should be used. If the difference is due to the surface roughness effects, then an appropriate correction should be applied to the momentum equation, which would incorporate the surface roughness effects. These two possible explanations are discussed in detail in the following sections.

5.3 Early transition to turbulence

From conventional theory, we know that when the Reynolds number increases to certain values, the internal flow undergoes a remarkable transition from laminar to turbulent regime. The origin of turbulence and the accompanying transition from laminar to turbulent flow is of fundamental importance to the science of fluid mechanics. In a flow at low Reynolds number through a straight pipe of uniform cross section and smooth

walls, every fluid particle moves with a uniform velocity along a straight path. Viscous forces slow the particles near the wall in relation to those in the center core. The flow is well ordered and particles travel along neighboring layers (laminar flow). However, this orderly pattern of flow ceases to exist at higher Reynolds number and strong mixing of the particles from different layers takes place. The fluctuation of streamlines at a fixed point causes an exchange of momentum in transverse direction. As a consequence, the velocity distribution over the cross section is considerably more uniform than in laminar flow. The most essential feature of the transition from laminar to turbulent flow is a noticeable change in the pattern of flow resistance. In laminar flow, the longitudinal pressure gradient, which maintains the motion, is proportional to the first power of average velocity, as can be seen from Equation (5.1). By contrast, in turbulent flow this pressure gradient becomes nearly proportional to the square of the average velocity of flow, Schlichting (1968). This increase in the resistance to flow results from the turbulent mixing motion.

The pressure gradient $(\Delta P/\Delta l)$ required to force liquid through a straight pipe of uniform cross-section generally has a relationship with the volume flow rate, $(\Delta P / \Delta l) \propto Q^n$, where Q is related to Re by Equation (5.2). In laminar region, $n=1$; in transitional flow region $1 < n < 2$ and in the turbulent flow region $n \geq 2$, Schlichting (1968). However, the experimental results obtained in this study for flow in microtubes in the conventional laminar flow region, *i.e.*, $Re < 2300$, exhibit a nonlinear relationship between $(\Delta P/\Delta l)$ and Q . It is observed from Figure 5.2, for both the *SS* and *FS* microtubes, that the $(\Delta P/\Delta l) \sim Re$ exhibit three distinct regions. For values of $Re \leq 300 \sim 500$, depending on the diameter of the microtube, the relation $(\Delta P/\Delta l) \sim Q$ is

approximately linear. For $300 \sim 500 \leq Re \leq 1000 \sim 1500$ the experimental results indicate that the value of the exponential 'n' is in the range $1 < n < 2$. For higher values of $Re \geq 1000 \sim 1500$, the measured $(\Delta P/\Delta l) \sim Q$ relation yield $n \geq 2$. As an example, these three distinct regions are shown separately in Figure 5.3, for a $130 \mu m$ SS microtube.

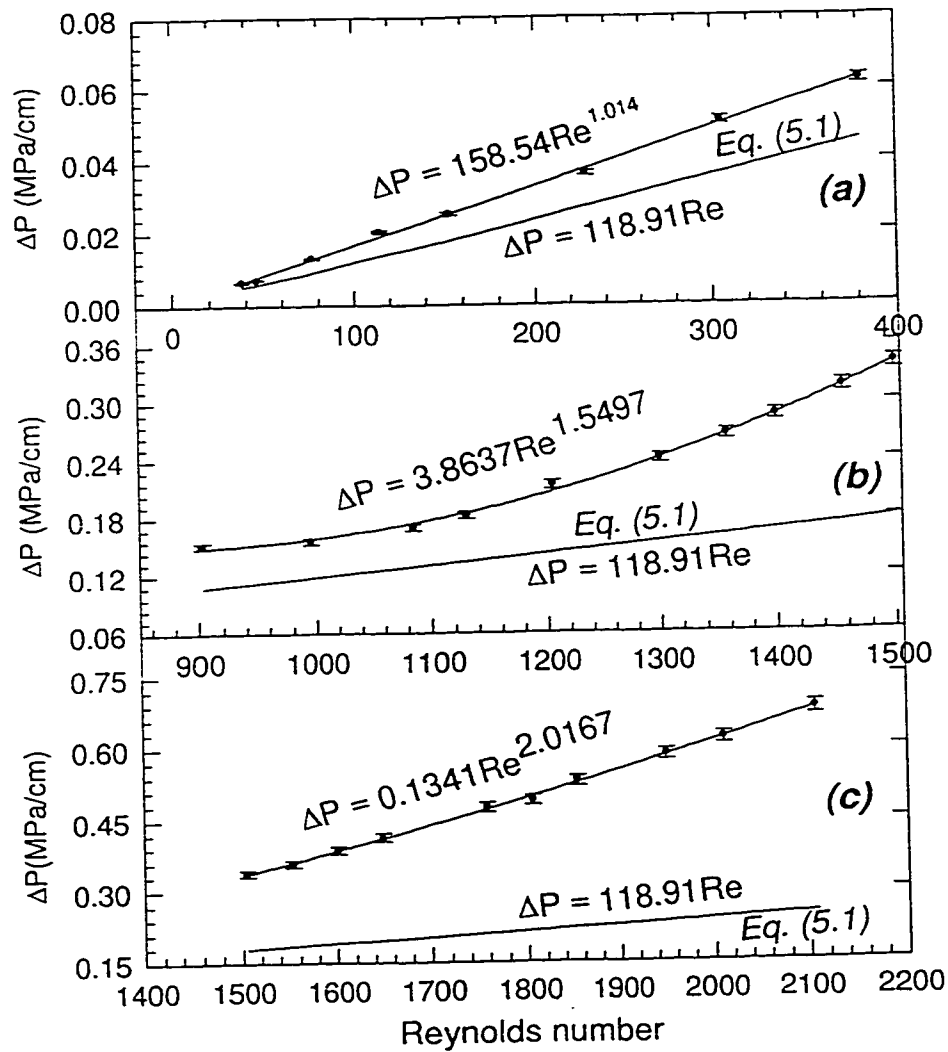


Figure 5.3: Experimentally obtained correlations of ΔP vs. Re in (a) $Re < 500$, (b) $900 < Re < 1500$ and (c) $Re > 1500$ flow regions of a $130 \mu m$ SS microtube and comparison with classical theory, Equation (5.1)

Figure 5.3a shows that in a small Re region there is a rough agreement between the experimental results and that predicted by the conventional laminar flow theory. A relation as given below correlates the experimental data for range of $Re < 650$

$$\Delta P / \Delta l = 121.77 Re^{1.014} \quad (5.3)$$

Whereas the theoretical prediction given by Equation (5.1) can be rewritten as

$$\Delta P / \Delta l = 118.91 Re \quad (5.4)$$

However, with an increase in Re the flow characteristics in the microtube seem to change from laminar to transitional flow, as shown in Figure 5.3b. The following relation correlates the experimental data in the range of $650 < Re < 1500$

$$\Delta P / \Delta l = 19.25 Re^{1.5497} \quad (5.5)$$

The exponent in the above relation increases to 1.5497 from 1.014. This transitional flow pattern starts from $Re \approx 500$ up to $Re \approx 1500$. For $Re > 1500$, the flow seems to be a fully developed turbulent flow as shown in Figure 5.3c, and the experimental data can be correlated by:

$$\Delta P / \Delta l = 0.1341 Re^{2.0167} \quad (5.6)$$

The exponent changes from less than 2 to greater than 2. For all the microtubes similar relations to Eqs. (5.3) to (5.6) can be obtained, except the range of Re values varies somewhat, depending on the diameter and the material of the microtube. Overall, from this analysis, it may be concluded that for microtubes there is an early transition from laminar to turbulent flow mode at $Re \geq 300 \sim 900$, and the flow changes to fully developed turbulent flow at $Re \geq 1000 \sim 1500$.

5.4 Friction characteristics

For a constant volume flow rate Q , the pressure gradient $\Delta P/\Delta l$ required to force the liquid through the microtube was measured. As discussed earlier the measured value of the $\Delta P/\Delta l$ is greater than that predicted by Equation (5.1). The coefficient of flow resistance f , also known as friction factor, for a pipe of a length l and a diameter D is related to the pressure gradient by the Darcy-Weisbach Equation as

$$f = \frac{\Delta P}{l} \frac{2D}{\rho u_{ave}^2} \quad (5.7)$$

For fully developed laminar flow in a macroscale pipe, Equation (5.7) can be shown to be

$$f = \frac{64}{Re} \quad (5.8)$$

Using the measured $\Delta P/\Delta l$ and Q data, we can determine the friction factor, f_{exp} in the experiment by using Equation (5.7). The variation of friction factor, f_{exp} , with the Re , for some SS and FS microtubes is shown in Figure 5.4. The pattern of f_{exp} vs. Re for the other microtubes is similar. As seen from the Figure 5.4, these curves exhibit three distinct regions. For small Re the friction factor decreases linearly with Re on the semi-log plots. When the Re becomes large, *i.e.* $Re \geq 1500$, the slope of the curve decreases and approaches zero. Between these two regions, the friction factor exhibits transitional characteristics. The regions are arbitrarily marked as I, II and III. In region I, there is a rough agreement between classical theory and experimental results, for Re up to about 500. Therefore, the Region I may be considered as the laminar flow region. As the Re increases, the deviation from the theoretical prediction increases as can be seen in region II for the Re range of approximately 500 ~ 1500. In region III, the difference between the theoretical and the experimental data is very large. However, as can be seen from the

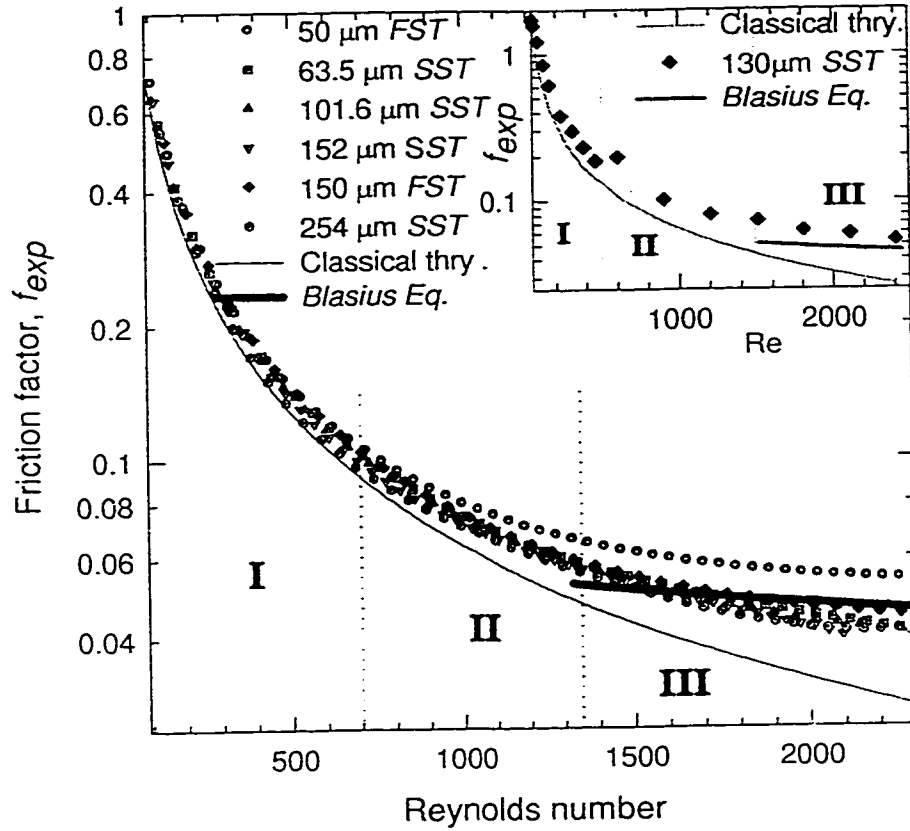


Figure 5.4: Friction factor f_{exp} vs. Re for some SS and FS microtubes and comparison with the classical theory, Equations (5.9) and (5.10).

Figure, that in this region the experimental data more or less follows the Blasius Equation, Schlichting (1968), given as:

$$f_{Blasius} = 0.3164 Re^{-0.25} \quad (5.9)$$

The Blasius Equation gives the friction factor for turbulent flow in smooth pipes for $Re \leq 10^5$. Thus, Blasius Equation can be used to determine the friction factor in microtubes for $Re \geq 1500$ with reasonable accuracy. Such friction characteristics have also been observed by Peng et al (1994b).

From the conventional theory we know that the product of the friction factor and the Reynolds number, $f^*Re = C$, has a constant value of $C=64$, for laminar flow ($Re < 2300$) in pipes. However, for flow in microtubes f^*Re is not equal to a constant. A friction constant ratio C^* is introduced as:

$$C^* = \frac{f_{exp} Re}{f_{th} Re} = \frac{f_{exp}}{f_{th}} \quad (5.10)$$

As can be seen from Figure 5.5, C^* is always greater than 1. The value of C^* changes as the Re increases. Tuckermann (1984) also observed such a dependence of friction constant on Reynolds number.

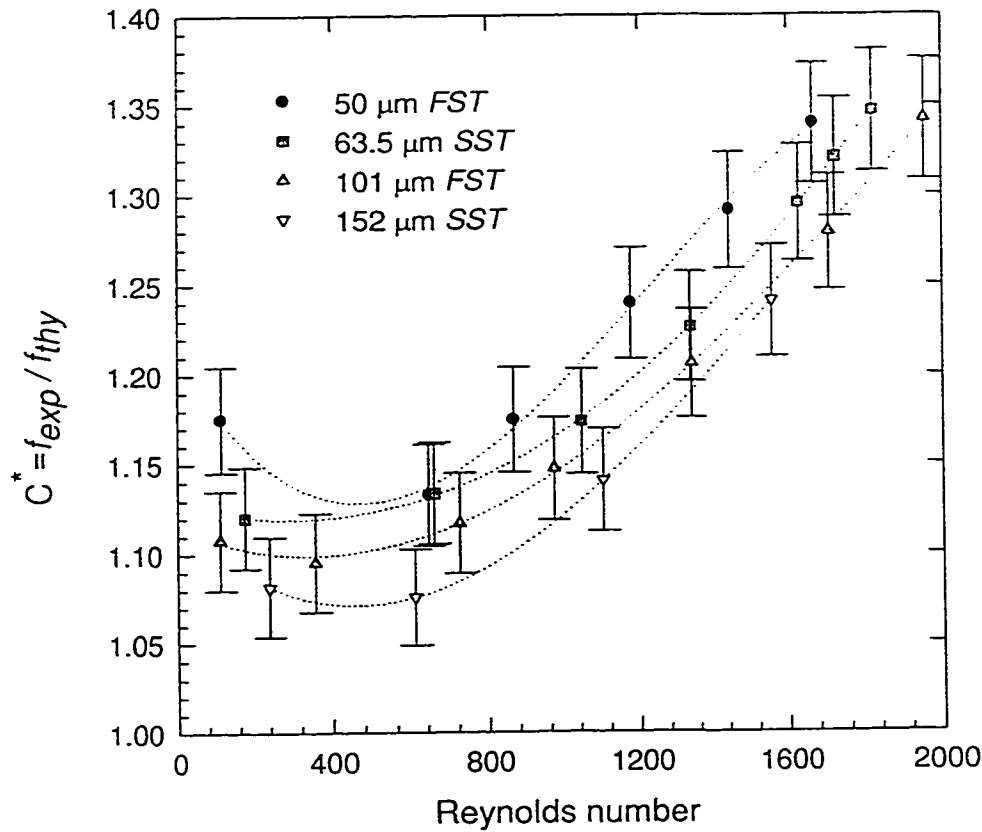


Figure 5.5: Friction constant ratio C^* (Equation 5.10) vs Re for some SS and FS microtubes

5.5 Effects of surface roughness:

As discussed before, the microtubes used in this study are of two different materials; stainless steel and fused silica. Stainless steel is a conducting material, thus no electrical double layer effects. Fused silica is non-conducting thus electrical double layers effects would be present. In principle, we should have included the effects of electrical double layer on flow in these microtubes. However, the microtube diameters are larger, all above 50 μm . Theoretically, it has been proved that the electrical double layer effects are negligible for such large microtubes. Hence, only the surface roughness effects are considered.

The presence of surface roughness affects the laminar velocity profile and decreases the transitional Reynolds number. This has been shown by a number of experiments and a comprehensive review can be found elsewhere (Merkle *et al*, 1974 and Tani, 1969). In the present work, based on Merkle's modified viscosity model the effects of the surface roughness on laminar flow in microtubes are considered in terms of a roughness-viscosity function. Generally, the roughness increases the momentum transfer in the boundary layer near the wall. This additional momentum transfer can be accounted for by introducing a roughness-viscosity μ_R in a manner similar to the eddy-viscosity concept in the turbulent flow model. Apparently, the roughness-viscosity μ_R should have a higher value near the wall and gradually diminish towards the center of the channel. The roughness viscosity μ_R should also be proportional to the Re . The ratio of the roughness-viscosity to the fluid viscosity is proposed to take the following form:

$$\frac{\mu_R}{\mu} = A Re_k \frac{r}{k} \left(1 - \exp \left(- \frac{Re_k r}{Re k} \right) \right)^2 \quad (5.11)$$

According to Merkle (1974), the velocity at the top of the roughness element is given by

$$U_k = \left(\frac{\partial u}{\partial r} \right)_{r=R} k \quad (5.12)$$

Then the roughness Reynolds number is defined as (Merkle, 1974):

$$\text{Re}_k = \frac{U_k k}{\nu} = \left(\frac{\partial u}{\partial r} \right)_{r=R} \frac{k^2}{\nu} \quad (5.13)$$

With Equation (5.12) and (5.13) all the parameters except for the coefficient A in the roughness-viscosity function, Equation (5.11), can be determined from the flow field, dimensions of the channel and the surface roughness. The coefficient A has to be determined by using the experimental data. By introducing the roughness-viscosity in the momentum equation in a manner similar to the eddy viscosity in the turbulent flow, the momentum equation for steady state laminar flow through a cylindrical channel becomes:

$$\frac{dP}{dx} = \frac{1}{r} \frac{\partial}{\partial r} \left((\mu + \mu_R) r \frac{\partial u}{\partial r} \right) \quad (5.14)$$

Dividing both sides of Equation (5.14) by μ and using the viscosity ratio Equation (5.11), we obtain

$$\frac{1}{\mu} \frac{dP}{dx} = \frac{1}{r} \frac{\partial}{\partial r} \left(\left(1 + A \text{Re}_k \frac{r}{k} \left(1 - \exp \left(- \frac{\text{Re}_k r}{\text{Re} k} \right) \right)^2 \right) r \frac{\partial u}{\partial r} \right) \quad (5.15)$$

Equation (5.15) can be further written as

$$E_3(r) = E_1(r) \frac{\partial u}{\partial r} + E_2(r) \frac{\partial^2 u}{\partial r^2} \quad (5.16)$$

Where

$$E_3(r) = \frac{r}{\mu} \frac{dP}{dx}$$

$$\begin{aligned}
E_1(r) &= 2A \text{Re}_k \frac{r}{k} \left(1 - \exp \left(-\frac{\text{Re}_k r}{\text{Re}_k k} \right) \right) \\
&\quad \left[\left(1 - \exp \left(-\frac{\text{Re}_k r}{\text{Re}_k k} \right) \right) + \frac{\text{Re}_k r}{\text{Re}_k k} \exp \left(-\frac{\text{Re}_k r}{\text{Re}_k k} \right) \right] + 1 \\
E_2(r) &= r \left(1 + A \text{Re}_k \frac{r}{k} \left(1 - \exp \left(-\frac{\text{Re}_k r}{\text{Re}_k k} \right) \right)^2 \right)
\end{aligned} \tag{5.17}$$

Equation (5.16) is the modified momentum equation that accounts for the effects of surface roughness in a laminar flow. The equation is a second-order, one-dimensional non-linear differential equation and can not be solved analytically. Therefore, a finite difference solution is sought with the following boundary conditions:

$$\text{At } r = 0, \quad \frac{\partial u}{\partial r} = 0, \text{ and } r = R, \quad u = 0 \tag{5.18}$$

The derivatives are written in central difference and are substituted back in Equation (5.16). The resulting system of equations is solved by using successive overrelaxation scheme, which is given as:

$$u_i^{j+1} = u_i^j + \omega (\bar{u}_i^j + u_i^{j-1}) \tag{5.19}$$

Where 'i' is the computational index and 'j' is the iteration index. If the roughness height is zero then solution of Equation (5.16) should reduce to the conventional Poiseuille flow solution. This condition is fulfilled as can be seen from Equation (5.17). For $k=0$, the roughness Reynolds number is zero, which yields $E_1(r)=1$, and $E_2(r)=r$; thus Equation (5.16) reduces to the conventional equation, for which the velocity distribution is given by:

$$u = \frac{\Delta P}{4\mu L} (R^2 - r^2) \tag{5.20}$$

Assuming an initial value of the coefficient A , Equation (5.16) can be numerically solved to obtain the velocity distribution in the microtubes by using the measured pressure gradient $\Delta P/\Delta l$ for dP/dx . Once the velocity profile is known, the volume flow rate can be calculated. Since the experimentally measured volume flow rate Q_{exp} and the pressure gradient $(dP/dx)_{exp}$ are known, the value of A is adjusted until the percentage difference between the calculated volume flow rate and the measured volume flow rate is smaller than $\pm 2\%$. Physically, the effects of the surface roughness depend on the shape and the distribution of the roughness elements. For the microtubes used in this work, the mean roughness height of $\pm 1.75 \mu m$ for each tube is provided by the manufacturers, but the shape and the distribution of the roughness elements are not known. As expected, the A value varies from tube to tube and ranges from 0.01 to 1 for all the microtubes used in this work. However, an empirical relationship was found as follows:

$$A = 0.1306 \left(\frac{R}{k} \right)^{0.3693} \exp \left\{ \text{Re} \left(6 \times 10^{-5} \frac{R}{k} - 0.0029 \right) \right\} \quad (5.21)$$

With this correlation, the roughness-viscosity function, given by Equation (5.11) can be computed. As mentioned earlier, the roughness-viscosity is higher near the wall and approaches to zero in the center of the channel. Figure 5.6, shows the roughness-viscosity ratio vs. the nondimensional radius for some microtubes at $Re=950$.

Figure 5.7 shows the comparison of the volume flow rates predicted by the roughness viscosity model (Equations 5.11, 5.14 and 5.21) with the measured volume flow rates. As can be seen clearly from Figure 5.7, the curves predicted by the model and the experimental curves are in an excellent agreement with each other. This implies that the roughness-viscosity model proposed in the present work may be used to interpret the

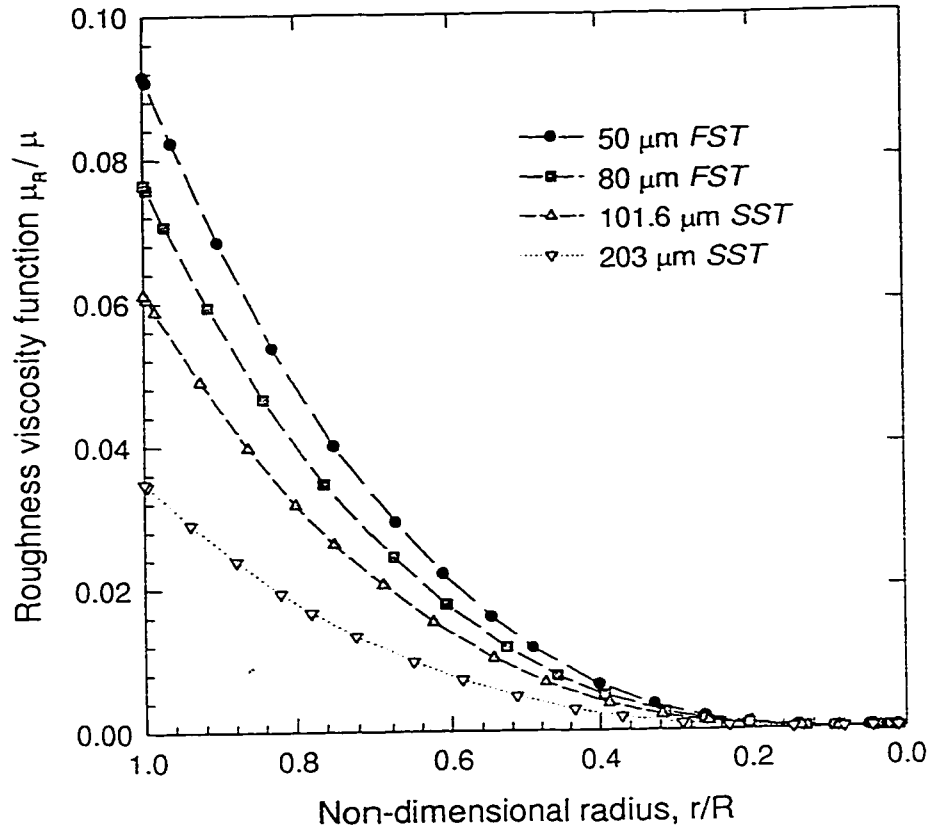


Figure 5.6: Variation of roughness viscosity ratio with non-dimensional radius for some SS and FS microtubes at various $Re = 950$

flow characteristics in microtubes. For the purpose of comparison, Figure 5.7, also shows the volume flow rates predicted by using the Poiseuille flow equation and the measured pressure gradient.

The velocity distribution in the microtubes obtained by using the roughness-viscosity model (*RVM*) and the experimental pressure gradient is shown in Figure 5.8. The velocity is plotted as the ratio of the local velocity to the average velocity with the non-dimensional radius of the microtubes, for different diameters and Reynold numbers.

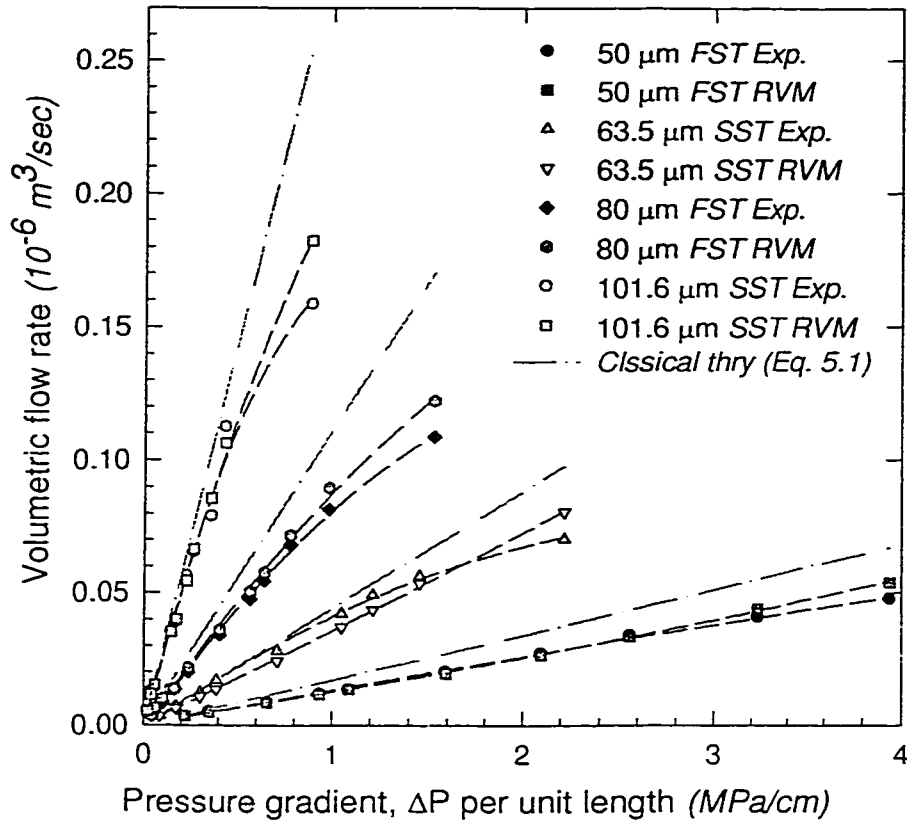


Figure 5.7: Comparison of volume flow rates predicted by roughness viscosity model (RVM) with the measured flow rates for some SS and FS microtubes and comparison with Eq(5.1).

As seen from Figure 5.8, the Poiseuille flow and the *RVM* velocity profiles are parabolic. However, the velocity predicted by *RVM* is smaller than that predicted by the Poiseuille flow equation. As shown in Figure 5.7, the roughness-viscosity model predicts the volumetric flow rates well. If the higher flow resistance is due to the surface roughness, one may expect that the velocity distribution resembles the *RVM* velocity profile in Figure 5.8.

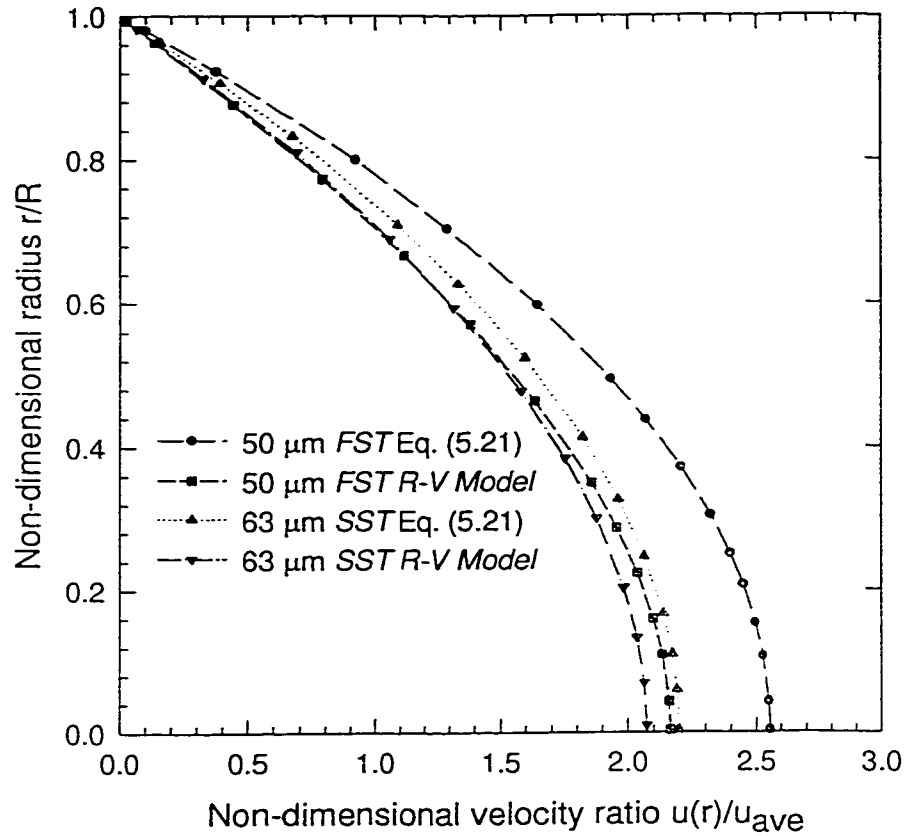


Figure 5.8: Comparison of roughness viscosity model and Poiseuille flow velocity distribution for some FS and SS microtubes

5.6 Summary

Flow characteristics of water flowing through cylindrical microtubes of stainless steel and fused silica were studied. The diameter of the microtubes ranges from 50 μm to 254 μm . It was observed that for a fixed volume flow rate, the pressure gradient required to force the liquid through the microtube is higher than that predicted by the conventional theory. For small flow rates, *i.e.* small Reynolds numbers, the conventional theory and

the experimental data are in a rough agreement. However, as the Reynolds number increases a significant deviation from the conventional theory was observed. The deviation increases as the diameter of the microtubes decreases. The flow behaviors also depend on the material of the microtubes. The friction factor and the friction constant are higher than that predicted by the conventional theory. The conventional friction constant value was found to depend on Reynolds number. Two possible reasons for this higher flow resistance are discussed. According to the measured $(\Delta P/\Delta l) \sim Q$ relationships and the conventional fluid mechanics theory, it seems that there is an early transition from laminar to turbulent flow. However, these phenomena may also be explained as the surface roughness effects by using a surface roughness-viscosity model proposed in this work.

5.7 References

1. Choi, S. B., Baron, R. R. and Warrington, R. O., 1991, 'Fluid flow and heat transfer in microtubes', *ASME DSC*, 40, 89-93
2. Harley, J. and Bau, H., 1989, 'Fluid flow in micron and submicron size channels', *IEEE Trans.*, Vol. THO249-3, 25-28
3. Hinze, J. O., 1975, '*Turbulence*', McGraw Hill, New York, 707
4. Merkle, C. L., Kubota, T. and Ko, D. R. S., 1974, '*An analytical study of the effects of surface roughness on boundary-layer transition*', AF Office of Scien. Res. Space and Missile Sys. Org., AD/A004786.
5. Peiyi, W. and Little, W. A., 1983, 'Measurement of friction factors for the flow of gases in very fine channels used for microminiature Joule-Thomson refrigerators', *Cryogenics*, **23**, 273-277
6. Peng, X. F. Peterson, G. P. and Wang, B. X., 1994a, 'Heat transfer characteristics of water flowing through microchannels', *Exp. Heat Transfer*, 7, 265-283
7. Peng, X. F. Peterson, G.P. and Wang, B. X., 1994b, 'Frictional flow characteristics of water flowing through microchannels', *Exp. Heat Transfer*, 7, 249-264

8. Pfahler, J. Harley, J. Bau, H. H. and Zemel, J., 1990, 'Liquid and gas transport in small channels', *ASME DSC*, **19**, 149-157
9. Pfahler, J. Harley, J. Bau, H. and Zemel, J., 1991, 'Gas and liquid flow in small channels', *ASME DSC*, **32**, 49-60
10. Schlichting, H., 1968, '*Boundary Layer Theory*', McGraw Hill, New York, 433
11. Tani, I., 1969, '*Boundary-Layer Transition*', Annual Reviews of Fluid Mechanics, Vol. I, Annual Reviews, Inc., Palo Alto, California.
12. Tuckerman, D. B., 1984, '*Heat transfer microstructures for integrated circuits*', Ph.D. Thesis, Dept. of Electrical Engineering, Stanford University, USA
13. Wang, B. W. and Peng, X. F., 1994, 'Experimental investigation on forced flow convection of liquid flow through microchannels', *Int. J. Heat Mass Transfer*, **37** (Suppl. 1) 73-82
14. Wu, P. Y. and Little, W. A., 1983, 'Measurement of friction factor for the flow of gases in very fine channels used for microminiature Joule-Thompson refrigerators', *Cryogenics*, **23**, 273-277
15. Wu, P. Y. and Little, W. A., 1984, 'Measurement of the heat transfer characteristics of gas flow in fine channel heat exchanger used for microminiature refrigerators', *Cryogenics*, **24**, 415-423

Chapter 6 Electrical Double Layer Potential Distribution In a Rectangular Microchannel

6.1 Introduction

The electrokinetic phenomena are of considerable importance in many fields of science and engineering. In particular, it exerts a strong influence on the flow behavior of a fluid in microchannels and capillaries. From early nineteenth century, the development of research in electrokinetic phenomena has contributed substantially to our understanding of the nature of the surface electric charge and the electrical nature of the interfacial layer. To understand the electrokinetic phenomena, we need to understand the relation between the surface electrostatic potential and the charge in the neighborhood of the interface. Most solid surfaces bear electrostatic charges. When a charged surface is in contact with an electrolyte, the electrostatic charges on the solid surface will influence the distribution of nearby ions in the electrolyte solution. Ions of opposite charges to that of the surface are attracted towards the surface, while the ions of like charges are repelled from the surface, and thus an electric field is established. The charges on the solid surface and the balancing charges in the liquid is called the 'Electric Double Layer' (*EDL*). The sign and magnitude of the *EDL* field depend on the nature of the surface and the liquid, Dukhin (1974). Helmholtz (Hunter, 1981) introduced the *EDL* as a 'molecular condenser', which has long been recognized as an inadequate representation of the situation. The charges in the solution are the ions that are spread out in space as a result of their thermal energy, forming a diffuse double layer. The theory of such diffuse double layer was developed by Gouy and Chapman in early 1900s and later modified by Stern, Hunter(1981). Stern proposed a model in which the *EDL* inner boundary is given by

approximately one hydrated ion radius. The inner boundary is referred to as the Stern plane. The gap between the Stern plane and the surface is denoted as the Stern layer in which the ions are considered to be immobile. The electrical potential changes from the surface potential to the Stern plane potential within the Stern layer and it decays to zero far away from the Stern plane. Ions whose centers are located beyond the Stern plane form the diffuse mobile part of the *EDL*. Consequently, the boundary where the mobile diffuse double layer starts is located about one or two radii away from the surface. This boundary is referred to as the shear plane. It is on this plane where the no-slip fluid flow boundary condition is assumed to apply. The potential at the shear plane is referred to as the electrokinetic potential, more commonly known as the zeta (ξ) potential, which is marginally different in magnitude from the Stern potential.

When a liquid is forced to flow through a microchannel under a hydrostatic pressure difference, the ions in the mobile part of the *EDL* are carried towards the downstream end. This causes an electrical current, called the streaming current, to flow in the direction of the liquid flow. The accumulation of ions downstream, however, will set up an electrical field with an electrical potential called the streaming potential. This field produces a backward ion flow called the conduction current. When the ions move in a liquid, they pull the liquid molecules to move with them. Thus the streaming potential will produce a liquid flow in the direction opposite to the pressure driven flow. Therefore, the presence of the *EDL* field has great influence on liquid flows in microchannels. In order to estimate the electrokinetic effects on microchannel flows, it is essential to understand and to describe the *EDL* field in the microchannels.

The *EDL* field is described by the Poisson-Boltzmann equation which is a two-dimensional, nonlinear, second order partial differential equation. The hyperbolic sine term makes the second order differential equation exponentially nonlinear; therefore, a general analytical solution is not possible. There are many studies in literature dealing with the solution of Poisson-Boltzmann equation. Rice and Whitehead (1965) have calculated analytically the correction factor that must be applied to Smoluchowski's results. Levine *et. al.*(1975), extended the Rice and Whitehead model to higher zeta potentials. Levine and Bell (1966), Bresler (1970), Levine (1975), Strauss and Bowen (1987) and Bowen and Jenner (1995) suggested various analytical and numerical techniques to solve the Poisson-Boltzmann equation for varying conditions. However, most of the work in this area dealt only with one dimensional *EDL* field, which holds only for channels with cylindrical and slit-shaped cross-sections. There are not any studies in literature regarding the solution of Poisson-Boltzmann equation for rectangular channels. This is, in part, due to mathematical difficulties in solving the nonlinear, two-dimensional Poisson-Boltzmann equation. However, in practice, microchannels used in electronic cooling, miniaturized chemical analysis and biomedical diagnostic instruments, are made by modern micromachining technology. The cross-section of the microchannels is close to rectangular shape. In such a situation, the two-dimensional Poisson-Boltzmann equation is required to describe the *EDL* field in the rectangular microchannels. In this chapter the two-dimensional, nonlinear Poisson-Boltzmann equation is solved for rectangular channels in two ways: (1) analytically with the use of Debye-Huckel approximation, and (2) numerically to obtain a complete solution without any assumption. The results of these two different approaches are compared and discussed.

6.2 Poisson-Boltzmann equation

Consider a liquid phase containing positive and negative ions in contact with a planar positively or negatively charged surface. The surface bears a uniform electrostatic potential, which decreases as one proceeds out into the fluid. Far away from the wall, the concentration of the positive and negative ions is equal. The electrostatic potential Ψ , at any point near the surface is related to the net number of electrical charges per unit volume ρ , in the neighborhood of the point, which measures the excess of the positive ions over negative ions or vice versa. According to the theory of electrostatics, the relation between Ψ and ρ is given by the Poisson's equation, Hunter (1981), which for a flat surface is

$$\nabla^2 \Psi = -\frac{\rho}{\epsilon \epsilon_0}$$

where ϵ is the dielectric constant of the medium and ϵ_0 is the permittivity of vacuum.

For a rectangular channel, with width W and depth H as shown in Figure 6.1, the Poisson equation can be written as:

$$\frac{\partial^2 \Psi}{\partial X^2} + \frac{\partial^2 \Psi}{\partial Y^2} = -\frac{\rho}{\epsilon \epsilon_0} \quad (6.1)$$

The probability of finding an ion at a particular point is proportional to the Boltzmann factor $e^{-ze\Psi/k_b T}$. For any fluid consisting of two kinds of ions of equal and opposite charge z^+ , z^- , the number of ions of each type are given by the Boltzmann equation, Hunter (1981).

$$n^- = n_0 e^{ze\Psi/k_b T} \text{ and } n^+ = n_0 e^{-ze\Psi/k_b T}$$

The net charge density in a unit volume of the fluid is given by

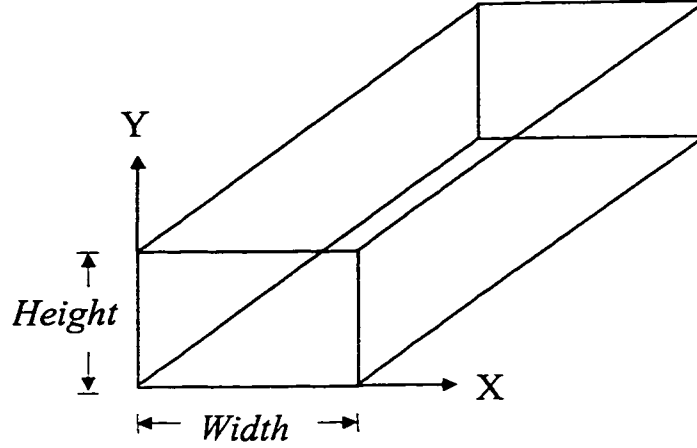


Figure 6.1: Schematic of a rectangular microchannel

$$\rho = (n^+ - n^-)ze = -2n_o ze \sinh(ze\Psi/k_b T) \quad (6.2)$$

Substituting Equation (6.2) in Equation (6.1), we obtain a nonlinear second-order two-dimensional Poisson-Boltzmann equation.

$$\frac{\partial^2 \Psi}{\partial X^2} + \frac{\partial^2 \Psi}{\partial Y^2} = \frac{2n_o ze}{\epsilon \epsilon_o} \sinh\left(\frac{ze\Psi}{k_b T}\right) \quad (6.3)$$

Nondimensionalizing Equation (6.1) via

$$x = \frac{X}{d_h}, \quad y = \frac{Y}{d_h}, \quad \psi = \frac{ze\Psi}{k_b T} \quad (6.4)$$

Where, d_h is the hydraulic diameter, defined as the ratio of four times the cross-sectional area to wetted perimeter. Using Equation (6.4) we obtain a nondimensional form of the Poisson-Boltzmann equation as:

$$\frac{\partial^2 \psi}{\partial x^2} + \frac{\partial^2 \psi}{\partial y^2} = \kappa^2 \sinh(\psi) \quad (6.5)$$

Where $\kappa = d_h * k$ and $k = (2n_o z^2 e^2 / \epsilon \epsilon_o k_b T)^{1/2}$. 'k' is called the Debye-Huckel parameter, while '1/k' is referred to as the characteristic thickness of the *EDL*.

Due to the symmetry of a rectangular channel, we will consider only one quarter of the rectangular channel for a linear approximate analytical solution and full channel cross-section for the complete numerical solution. Equation (6.5) is subjected to the following boundary conditions:

$$\text{at } x = \frac{\overline{W}}{2}; \quad \frac{\partial \psi}{\partial x} = 0 \quad \text{and at } x = \overline{W}; \quad \psi = \overline{\xi}_2 \quad (6.5a)$$

$$\text{at } y = \frac{\overline{H}}{2}; \quad \frac{\partial \psi}{\partial y} = 0 \quad \text{and at } y = \overline{H}; \quad \psi = \overline{\xi}_1 \quad (6.5b)$$

where

$\overline{W} = \frac{W}{d_h}$, is the non-dimensional channel width, $\overline{H} = \frac{H}{d_h}$, is the non-dimensional channel

height and $\overline{\xi}_i = \frac{ze\xi_i}{k_b T}$ ($i = 1, 2$), is the non-dimensional zeta potential at the channel walls.

For comparison between the linear approximate analytical solution and complete numerical solution, all surfaces of the channel are assumed to have the same zeta potential.

6.3 Solution of the Poisson-Boltzmann equation

Equation (6.5), a two-dimensional, second-order, nonlinear partial differential equation, can not be solved analytically. Therefore, approximate solutions and complete numerical solutions are sought. Here we discuss two types of solutions viz. the analytical approximate solution by linearizing the Poisson-Boltzmann equation and a complete numerical solution by employing successive overrelaxation with grid clustering.

6.3.1 Linear approximate analytical solution

If the electrical potential is small compared to the thermal energy of the ions, *i.e.*, $(|ze\Psi| < |k_b T|)$ so that the exponential in Equation (6.5) can be approximated by the first terms in a Taylor series. This transforms Equation (6.5) to

$$\frac{\partial^2 \Psi}{\partial x^2} + \frac{\partial^2 \Psi}{\partial y^2} = \kappa^2 \Psi \quad (6.6)$$

In literature this is called the Debye-Huckel linear approximation, Hunter (1981). This approximation is valid only for small values of electrostatic potential Ψ . At room temperature, the condition $(|ze\Psi| < |k_b T|)$ requires $\Psi < 25 \text{ mV}$.

By using the separation of variables method, the solution to the linearized Poisson-Boltzmann equation, Equation (6.5), with the boundary conditions Equations (6.5a) and (6.5b) can be obtained. Therefore, the non-dimensional electrical potential distribution in the rectangular microchannel is of the form

$$\begin{aligned} \psi(x, y) = & 4\bar{\xi}_1 \sum_{m=1}^{\infty} \frac{(-1)^{m+1} \cosh\left[\sqrt{1 + \frac{(2m-1)^2 \pi^2}{\kappa^2 \bar{W}^2}} \kappa(y - 0.5\bar{H})\right]}{(2m-1)\pi \cosh\left[\sqrt{1 + \frac{(2m-1)^2 \pi^2}{\kappa^2 \bar{W}^2}} \frac{\kappa \bar{H}}{2}\right]} \cos\left[\frac{(2m-1)\pi}{\bar{W}}(x - 0.5\bar{W})\right] \\ & + 4\bar{\xi}_2 \sum_{n=1}^{\infty} \frac{(-1)^{n+1} \cosh\left[\sqrt{1 + \frac{(2n-1)^2 \pi^2}{\kappa^2 \bar{H}^2}} \kappa(x - 0.5\bar{W})\right]}{(2n-1)\pi \cosh\left[\sqrt{1 + \frac{(2n-1)^2 \pi^2}{\kappa^2 \bar{H}^2}} \frac{\kappa \bar{W}}{2}\right]} \cos\left[\frac{(2n-1)\pi}{\bar{H}}(y - 0.5\bar{H})\right] \end{aligned} \quad (6.7)$$

In practice, most solid-liquid surfaces have a surface electrical potential larger than 25 mV . Therefore, the above linearized solution is not applicable theoretically. For situations of higher surface electrical potentials, the two-dimensional nonlinear Poisson-Boltzmann equation, Equation (6.5) has to be solved without using the Debye-Huckel assumption. The numerical solution is the only way to do so.

6.3.2 Complete numerical solution by successive overrelaxation:

Equations (6.5) is solved numerically by five point central difference with successive overrelaxation. The finite difference equation for the left hand side terms in Equation (6.5) are:

$$\frac{\partial^2 \psi}{\partial x^2} = \frac{\psi_{i+1,j}^{k+1} - 2\psi_{i,j}^{k+1} + \psi_{i-1,j}^{k+1}}{\Delta x^2} \quad (6.8a)$$

$$\frac{\partial^2 \psi}{\partial y^2} = \frac{\psi_{i,j+1}^{k+1} - 2\psi_{i,j}^{k+1} + \psi_{i,j-1}^{k+1}}{\Delta y^2} \quad (6.8b)$$

for $i = 1, 2, \dots, m$, and $j = 1, 2, \dots, n$.

The functions on the right hand side of Equation (6.5) can be written as:

$$\sinh \psi_{i,j}^k = \frac{1}{2} \{ e^{\psi_{i,j}^k} - e^{-\psi_{i,j}^k} \}$$

The right hand side of the above equation can be expanded as, Ames (1977,1965)

$$e^{\psi_{i,j}^k} = e^{\psi_{i,j}^{k+1}} + [\psi_{i,j}^{k+1} - \psi_{i,j}^k] e^{\psi_{i,j}^k} \quad (6.9a)$$

$$e^{-\psi_{i,j}^k} = e^{-\psi_{i,j}^{k+1}} - [\psi_{i,j}^{k+1} - \psi_{i,j}^k] e^{-\psi_{i,j}^k} \quad (6.9b)$$

Substituting Equations (6.8) and (6.9) in Equation (6.5), the finite difference form of the nonlinear Poisson-Boltzmann equation becomes:

$$\begin{aligned} \psi_{i+1,j}^{k+1} + \psi_{i-1,j}^{k+1} + \gamma \psi_{i,j+1}^{k+1} + \gamma \psi_{i,j-1}^{k+1} - 2(1-\gamma) \psi_{i,j}^{k+1} - \kappa^2 \psi_{i,j}^{k+1} \sinh \psi_{i,j}^k \\ = \kappa^2 (\sinh \psi_{i,j}^{k+1} - \psi_{i,j}^k \cosh \psi_{i,j}^k) \end{aligned} \quad (6.10)$$

Where $\gamma = (\frac{\Delta x}{\Delta y})^2$

The above equation can be solved for $\psi_{i,j}^{k+1}$ by successive overrelaxation, *i.e.*, using the value of ψ obtained in the k^{th} iteration, where k is the outer iteration index, represented as $\psi_{i,j}^k$ to update its value in next, *i.e.*, $(k+1)^{th}$ iteration, represented as $\psi_{i,j}^{k+1}$,

Ames (1977). A complete numerical solution of the Poisson-Boltzmann equation can be obtained in this way.

It should be realized that the electrical potential of the *EDL* field decays sharply within a small distance near the channel wall; thereafter, the electrical potential approaches zero very slowly. In order to obtain more information about the *EDL* field and reduce the truncational error it is desirable to use smaller grid size (step size) in the region near the channel wall where the *EDL* potential has a very sharp gradient, and to use larger grid size in the region of some distance away from the wall. This is achieved by employing the following grid clustering scheme, Anderson et al (1984).

The x coordinate is transformed into \hat{x} :

$$\hat{x} = \alpha + (1 - \alpha) \frac{\ln\{(\beta_x + [x(2\alpha + 1)/W] - 2\alpha) / (\beta_x - [x(2\alpha + 1)/W] + 2\alpha)\}}{\ln\{(\beta_x + 1) / (\beta_x - 1)\}} \quad (6.11a)$$

and y coordinate is transformed into \hat{y} :

$$\hat{y} = \alpha + (1 - \alpha) \frac{\ln\{(\beta_y + [y(2\alpha + 1)/H] - 2\alpha) / (\beta_y - [y(2\alpha + 1)/H] + 2\alpha)\}}{\ln\{(\beta_y + 1) / (\beta_y - 1)\}} \quad (6.11b)$$

In this transformation using $\alpha=0.5$ the mesh will be refined equally near both the boundaries *e.g.* $\hat{x}=0$ and at $\hat{x}=\overline{W}$. β_x and β_y are called as the stretching parameters ($\beta_x = \beta_y = 1.0000001$, were used here) and control the degree of clustering in x and y directions, respectively. Equation (6.5) is written in terms of the computational grid (\hat{x}, \hat{y}) as:

$$\frac{\partial^2 \psi}{\partial \hat{x}^2} \left(\frac{\partial \hat{x}}{\partial x} \right)^2 + \frac{\partial \psi}{\partial \hat{x}} \frac{\partial^2 \hat{x}}{\partial x^2} + \frac{\partial^2 \psi}{\partial \hat{y}^2} \left(\frac{\partial \hat{y}}{\partial y} \right)^2 + \frac{\partial \psi}{\partial \hat{y}} \frac{\partial^2 \hat{y}}{\partial y^2} = \kappa^2 \sinh \psi \quad (6.12)$$

The finite difference form of Equation (6.12) for the solution of the nondimensional electrical potential is

$$\psi_{i,j}^{k+1} = \frac{\chi_{i+1,j} \psi_{i+1,j}^{k+1} + \chi_{i-1,j} \psi_{i-1,j}^{k+1} + \chi_{i,j+1} \psi_{i,j+1}^{k+1} + \chi_{i,j-1} \psi_{i,j-1}^{k+1} - \phi_{i,j}^k}{\chi_{i,j} + \kappa^2 \cosh \psi_{i,j}^k} \quad (6.13)$$

where,

$$\begin{aligned} \chi_{i+1,j} &= \left(\frac{1}{(\Delta \hat{x})^2} \left(\frac{\partial \hat{x}}{\partial x} \right)^2 + \frac{1}{2\Delta \hat{x}} \frac{\partial^2 \hat{x}}{\partial x^2} \right) \\ \chi_{i-1,j} &= \left(\frac{1}{(\Delta \hat{x})^2} \left(\frac{\partial \hat{x}}{\partial x} \right)^2 - \frac{1}{2\Delta \hat{x}} \frac{\partial^2 \hat{x}}{\partial x^2} \right) \\ \chi_{i,j} &= \left(\frac{2}{(\Delta \hat{x})^2} \left(\frac{\partial \hat{x}}{\partial x} \right)^2 + \frac{2}{(\Delta \hat{y})^2} \left(\frac{\partial \hat{y}}{\partial y} \right)^2 \right) \\ \chi_{i,j+1} &= \left(\frac{1}{(\Delta \hat{y})^2} \left(\frac{\partial \hat{y}}{\partial y} \right)^2 + \frac{1}{2\Delta \hat{y}} \frac{\partial^2 \hat{y}}{\partial y^2} \right) \\ \chi_{i,j-1} &= \left(\frac{1}{(\Delta \hat{y})^2} \left(\frac{\partial \hat{y}}{\partial y} \right)^2 - \frac{1}{2\Delta \hat{y}} \frac{\partial^2 \hat{y}}{\partial y^2} \right) \\ \phi_{i,j}^k &= \kappa^2 \left(\sinh \psi_{i,j}^k - \psi_{i,j}^k \cosh \psi_{i,j}^k \right) \end{aligned}$$

Equation (6.13) results in a set of algebraic equations that are solved by successive overrelaxation, as explained previously, through Equation (6.14)

$$\psi_{i,j}^{k+1} = \psi_{i,j}^k + \omega(\psi_{i,j}^{k+1} - \psi_{i,j}^k) \quad (6.14)$$

Where ω is the relaxation parameter.

6.4 Results and discussion

Using the above described linearized analytical solution and the complete numerical solution methods, the two-dimensional Poisson-Boltzmann equation was solved for *EDL* field in rectangular microchannels. The liquid is a dilute aqueous 1:1

electrolyte solution ($concentration=10^{-6} M$) at a temperature of $18^{\circ}C$. A rectangular microchannel of cross-sections $30 \mu m$ wide and $20 \mu m$ high with different zeta potentials of $150 mV$, $75 mV$ and $25 mV$ is considered.

For this microchannel, the *EDL* potential in the diffuse double layer region is calculated. For $\xi=150 mV$, the potential distribution is given in Figure 6.2. For the same value of zeta potential, the electrical potential distribution with linear approximation is shown in Figure 6.2a, and the nonlinear electrical potential distribution calculated by the complete numerical solution is shown in Figure 6.2b. As can be observed from the two figures, there is a very steep decrease in the potential in the case of the complete solution, while the linear solution predicts a more gradual decay of the potential, for example, consider the channel height direction. In the case of the complete solution, the potential becomes zero at a nondimensional distance 0.08 from the channel wall whereas for the linear case the potential becomes approximately zero at a nondimensional distance 0.25 from the channel wall. This implies that the linear approximation predicts much higher values of the potential than that predicted by the complete solution in the region close to the wall. In Figure 6.3 the potential distribution for $\xi=75 mV$ is shown for both the linear solution, Figure 6.3a, and the complete solution, Figure 6.3b. A similar pattern to Figure 6.2 is observed. However, at $\xi= 25 mV$, the prediction by the linear solution and the complete solution are relatively close to each other. This is shown in Figure 6.4. Figure 6.4a shows the potential distribution of linear solution while Figure 6.4b shows the potential distribution of the complete solution. This implies that the linear approximation may be used only for the zeta potentials less than $25 mV$ without causing significant error.

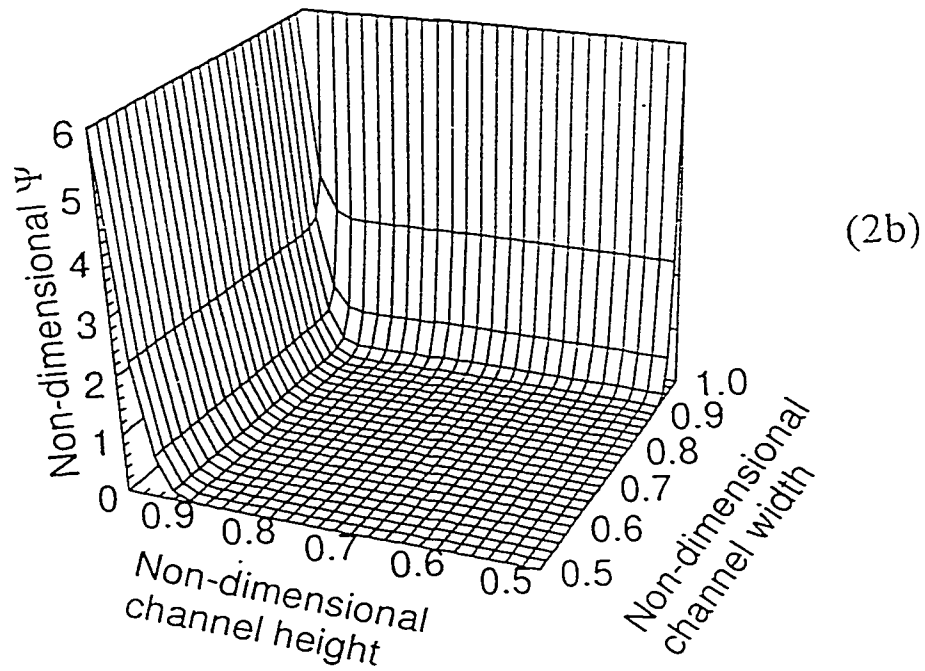
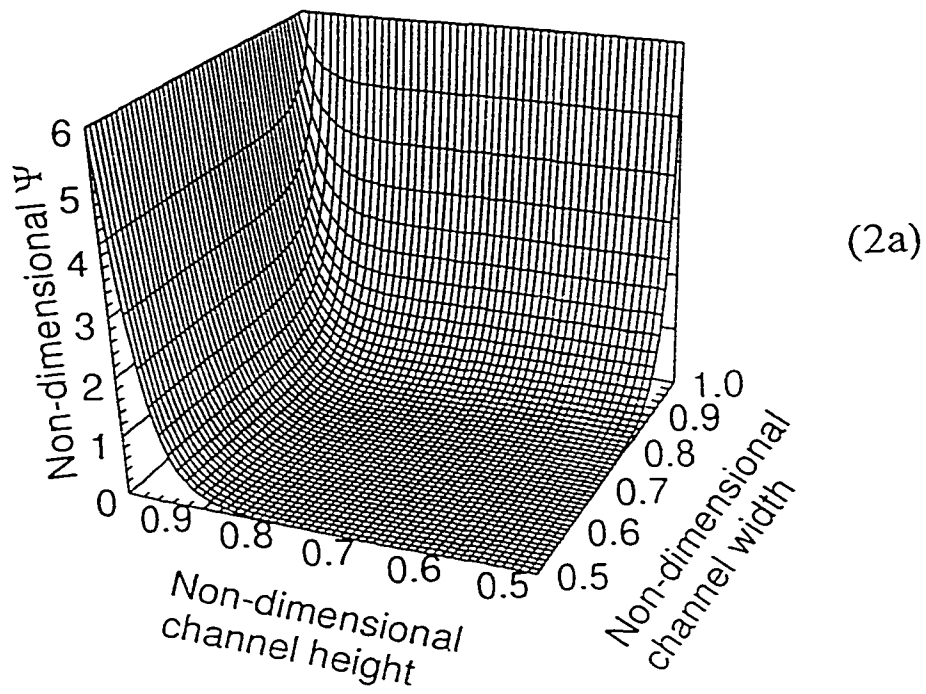


Figure 6.2: Nondimensional EDL potential distribution in one quarter of the microchannel, with $\xi=150\text{mV}$ a) linear solution, and b) complete numerical solution

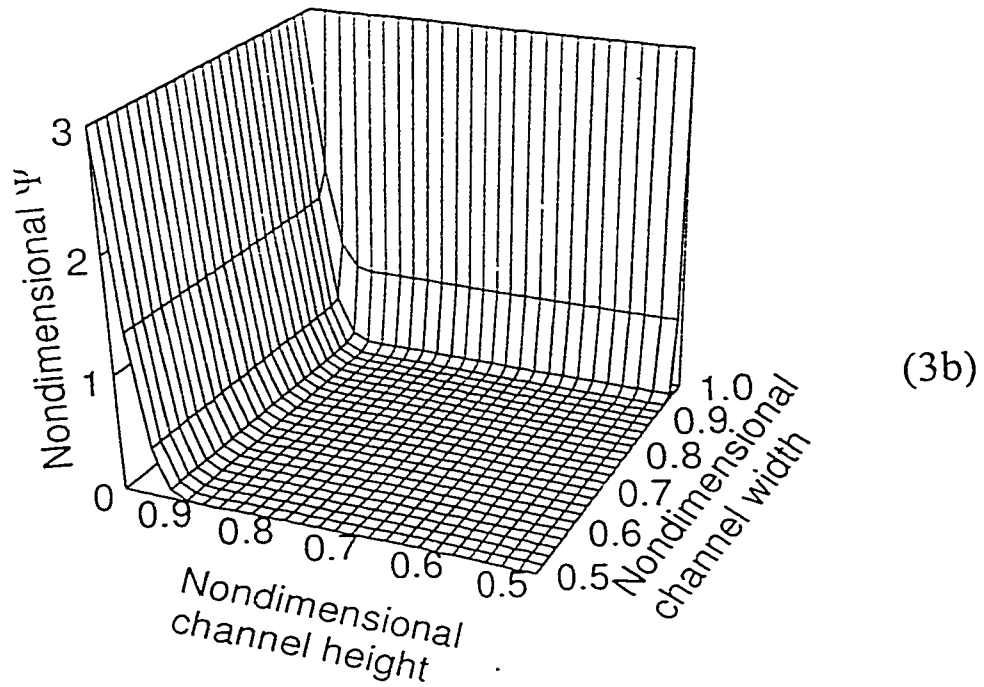
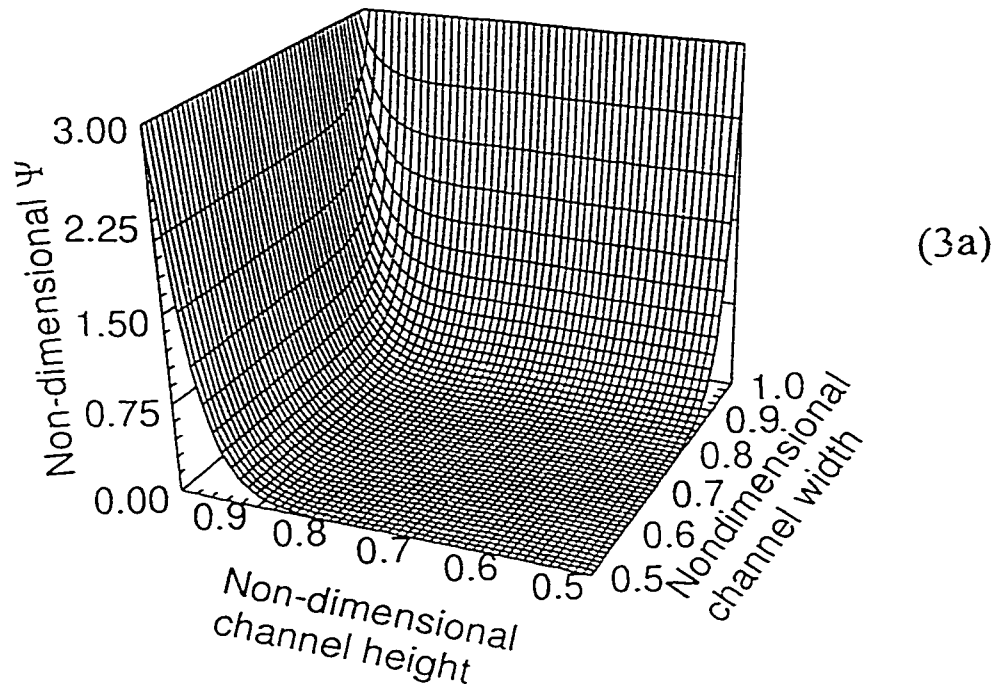


Figure 6.3: Nondimensional EDL potential distribution in one quarter of the microchannel, with $\xi=75$ mV a) linear solution, and b) complete numerical solution

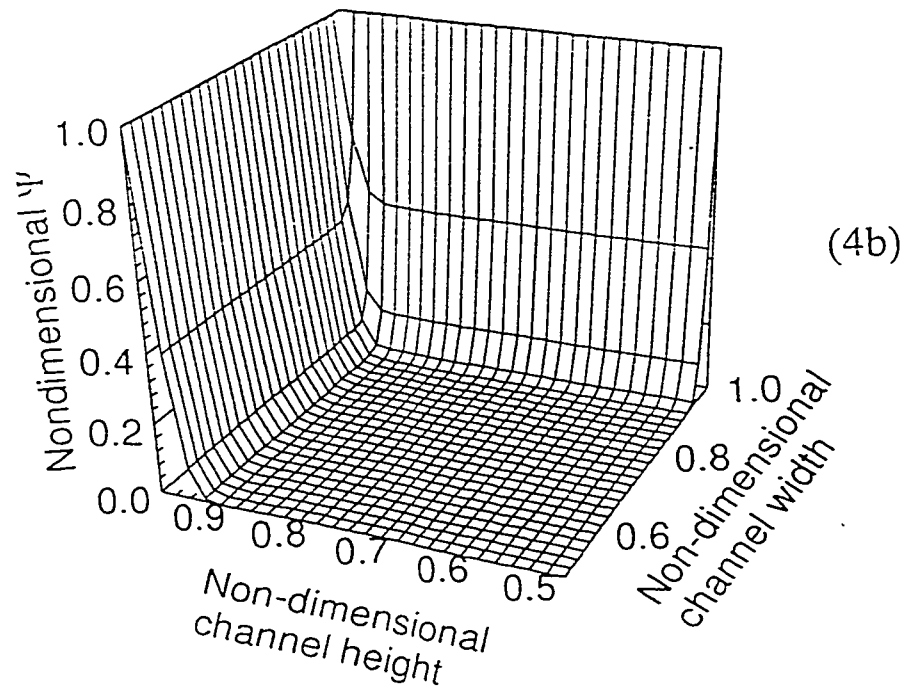
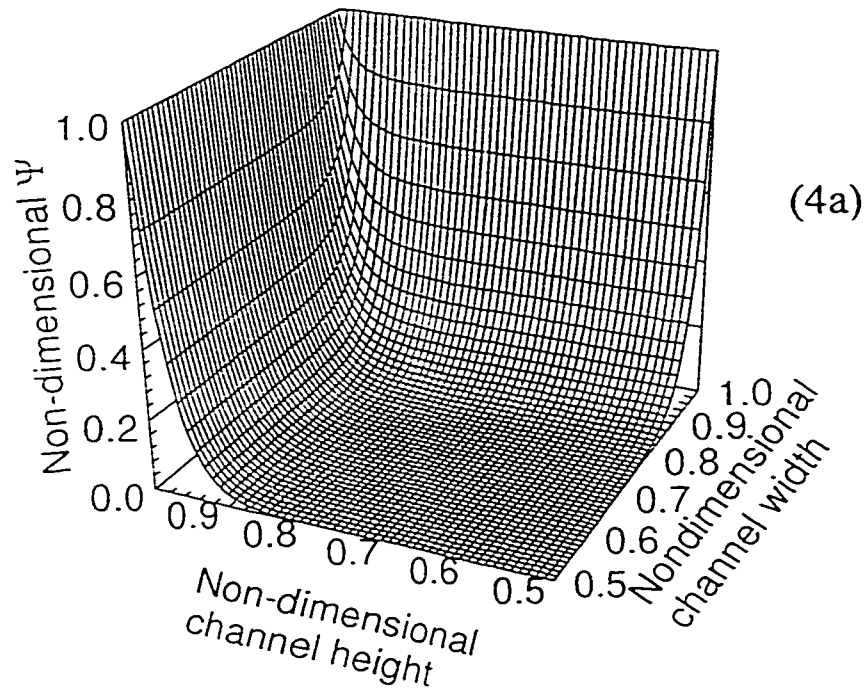


Figure 6.4: Nondimensional EDL potential distribution in one quarter of the microchannel, with $\xi_0=25$ mV a) linear solution, and b) complete numerical solution

In order to see more clearly the difference between the linear solution and the complete solution, the profiles (viewed from the channel height side) of the potential distributions given in Figures 6.2-6.4 are plotted in Figure 6.5. As can be seen from the Figure 6.5 for $\xi=150 \text{ mV}$ the linear solution (line 2) gives a higher estimation of the potential than the complete solution (line 1). For $\xi=75 \text{ mV}$, the pattern is similar although the difference between the line 3 and line 4 is smaller. For $\xi=25 \text{ mV}$, the difference between the linear and the complete solution is very small. Thus again, for small ξ potentials, linear approximation can be used without much error. But for the case of higher ξ potential, linear approximation results in very large errors in the region close to the channel wall.

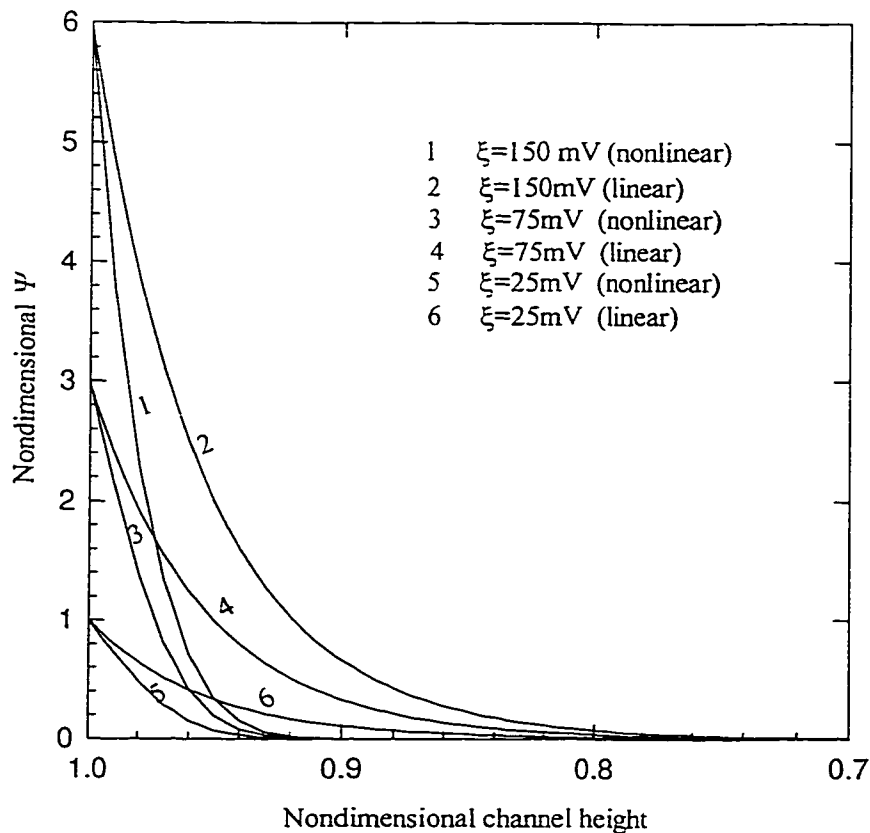


Figure 6.5: Comparison of the profiles of the linear and the nonlinear EDL potential distributions for three zeta potential values

It is well known from conventional fluid mechanics theory, that the flow rate from a square or rectangular duct is about 88.33% of the flow rate from a circular duct of the same cross-sectional area under the same conditions, Happel and Brenner (1965). This reduced flow rate is due to the sharp corners of the non-circular duct. From Figures 6.2-6.4, we can observe the effect of the corners of the rectangular channel on the electrical potential distribution. Therefore, for microchannel flows the *EDL* potential in the corner regions would be expected to cause a strong resistance to the flow. Such corner effects would be even higher if the linear solution is used. This may result in an error in modeling the electrokinetic flow behavior in microchannels if the linear approximation is used to solve the Poisson-Boltzmann equation.

Microchannels produced by microfabrication techniques, like chemical etching, often are made of more than one material. A slot is first chemically etched on a substrate plate and then a cover plate is bonded on the top to form a microchannel. The cover plate may or may not be the same material as the substrate. As the surface electrical potential depends on the solid materials, a microchannel formed in this way may have different surfaces electrical potentials at different surfaces. Using the numerical method described in this chapter, the *EDL* potential distribution in such a rectangular microchannel can be obtained. Figure 6.6 shows the potential distribution in a quarter of a rectangular microchannel formed by two surfaces with different zeta potentials of 200 mV and 75 mV , respectively.

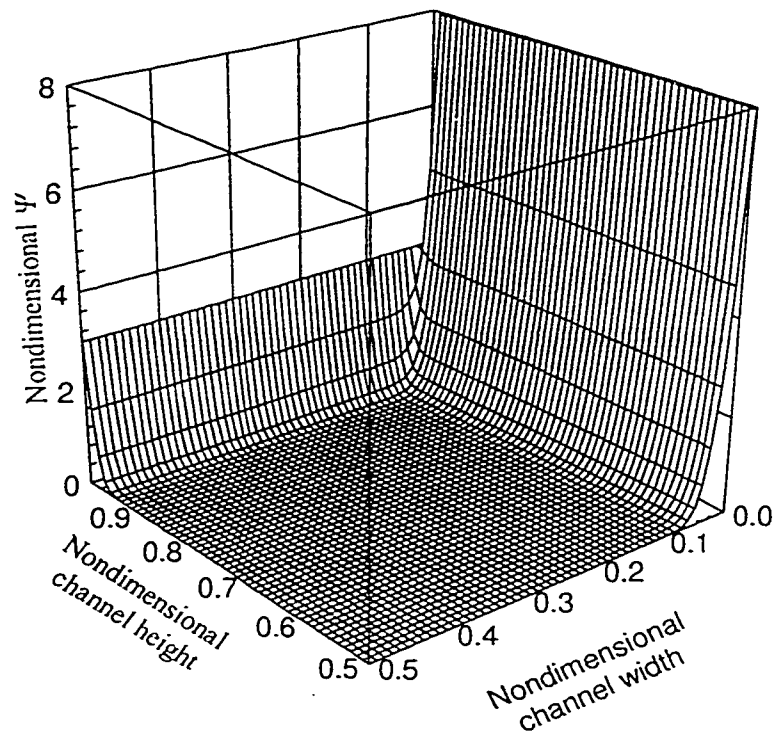


Figure 6.6: Nonlinear EDL potential distribution in a quarter of a microchannel with different ξ potentials at different surfaces

6.5 References

1. Ames F., 1977, '*Numerical methods for partial differential equations*', Academic Press, New York, pp. 130-135.
2. Ames F., 1965, '*Partial differential equations in engineering*', Academic Press, New York
3. Anderson A., Tannehill J. C. and Pletcher R. H., 1984, '*Computational fluid mechanics and heat transfer*', Hemisphere Pub. Corp., Washington
4. Bowen H.K. and Jenner F., 1995, *J. Colloid Interface Sci.*, Vol. 173, p. 388-395.
5. Bresler E., 1970, *J. Colloid Interface Sci.*, Vol. 33, p-278.

6. Dukhin S. S., 1974, '*Development of notion as to the mechanism of electrokinetic phenomena and the structure of the colloid micelle*' in *Surface and Colloid Sciences* Vol. 7, editor, E. Matijevic, John Wiley & Sons, New York, Chap 1, pp. 1-47.
7. Hunter R.J., 1981, '*Zeta potential in colloid science*', Academic Press, London
8. Happel J. and Brenner H., 1965, '*Low Reynolds number hydrodynamics*', Prentice-Hall Inc. SA, p-39.
9. Levine S. *et al.*, 1975, *J. Colloid Interface Sci.*, Vol. 52, No. 1, pp-136-149.
10. Levine S. and Bell G.M., 1966, *Discuss. Faraday Soc.* Vol. 42, p-69.
11. Levine P. L., 1975, *J. Colloid Interface Sci.*, Vol. 51, p-72.
12. Rice C. L. and Whitehead R., 1965, *Journal of Physical Chemistry*, Vol. 69, No. 11, pp. 4017-4023.
13. Strauss T. A. R. and Bowen H. K., 1987, *J. Colloid Interface Sci.*, Vol. 118, No. 2, p-326.

Chapter 7 Design of an Experimental Apparatus for Trapezoidal Silicon Microchannels

7.1. Design considerations

The goal of this study was to investigate and understand the fundamental aspects of flow and heat transfer of water in different types of microchannel (like rectangular, circular and trapezoidal) over a range of Reynold numbers. Because, only a complete understanding of the fundamental aspects can help in seeking answers to the questions being asked about microscale fluid flow. As discussed in literature review section of Chapter 2, there are number of studies that observed conflicting flow characteristics than that predicted by the conventional fluid mechanics theory. The three approaches to analyze any flow and heat transfer problem are theoretical prediction, numerical simulation and experimental investigation. However, in conventional theory, the governing equations of motion i.e. Navier-Stokes equations coupled with energy equation can not be solved analytically. Therefore, assumptions are made to reduce the system of equations to one or two-dimensional system to obtain an approximate analytical solution. In case of numerical simulation, the equations of motion can be solved numerically by a number of techniques developed over the years. With this approach, slightly more information can be derived than the theoretical approach. In fact, one can say that the numerical simulation is an extension of the theoretical approach with the advantage of solving the complete system of governing equations. Nevertheless, for fundamental investigation experimentation is very critical. The first two methods are used to analyze the experimental results. In fact, the theoretical and the numerical results should be

substantiated by the experimental results to incorporate any appropriate corrections to the governing system of equations.

To estimate the liquid flow and heat transfer characteristics of water in microchannels, in addition to the physical dimensions, the following parameters should be measured:

1. Pressure drop
2. Volume flow rate
3. Inlet temperature of water
4. Outlet temperature of water
5. Surface temperature or heat flux

By estimating the flow rate and the pressure drop, the friction characteristics, average velocity, Reynolds number etc. can be calculated. With the inlet and outlet temperature of the water, and the surface boundary temperature or heat flux, the heat transfer characteristics can be predicted. Nevertheless, as discussed in preceding chapters, interfacial effects play an important role in understanding the microscale flow behavior. Therefore, it became necessary to measure electrokinetic parameters, like:

1. Streaming potential
2. Streaming current
3. Electrical conductivity of water
4. Ionic concentration in water

By measuring these parameters the electrical potential at the solid-liquid interface, often referred to as the zeta potential can be estimated. Once the zeta potential is known, the distribution of the electrical double layer at the solid-liquid interface can be

determined. Therefore, the effects of the electrokinetic parameters on flow in microchannels can be estimated. All these measurements can help in predicting the flow and heat transfer characteristics in microchannels with a reasonable accuracy.

7.2. Pressure requirements and measurement

Measurement of the pressure drop is quite straightforward. A Valedyne pressure transducer with a piezoresistive-sensing element is used to measure the pressure differential across the microchannel. The piezoresistive effect is defined as the change in the resistivity ρ , of a material with applied mechanical strain e , and is represented by the term $(1/e)(\Delta\rho/\rho)$. Silicon doped with small amounts of N or P type material exhibits a large piezoresistive effect and is used to manufacture strain gauges with high gauge factors. In piezoresistive pressure sensors, the elastic element is a flat silicon diaphragm. The distortion of the diaphragm is sensed by the four-piezoresistive strain elements made by introducing doping material into the areas of the silicon, where the strain is greatest. Sensing elements with different pressure ranges are available. The sensing element of the transducer used for the pressure drop measurement has a range of ± 2500 psi. The transducer is calibrated with a dead weight tester calibrator. The calibration and the specifications can be found in appendix I.

However, as the characteristic dimension (hydraulic diameter) of the microchannels decreases, high-pressure gradients are required even for very small flow rates. Therefore, the nature of the system dictates the necessity of a high-pressure pump with small but constant flow rates. For this purpose, a high precision RUSKA[®] proportioning pump was used. This high precision pump has a constant flow rate range of 2 to 650 cc/hr with a pressure rating of up to 5000 psi. Depending on the selected feed

rate, the pump dispenses liquid at a constant flow rate while the pressure increases as required. For comparatively larger microchannels, where the pressure required is less than 100 psi, a low pressure (100-psi max) Masterflex[®] tubing pump is used. The pump can be operated either at a fixed or variable speed. The main features of this pump are high accuracy drives for precise flow control. The specifications of both pumps are given in appendix I.

7.3. Flow rate measurement

Three different methods were employed to measure the flow rates of water flowing through the microchannels. The high precision pump has a calibrated flow scale from which the flow rate can be directly read. For a constant speed, the feed rate is also constant therefore; by recording the displacement and time the flow rate can be easily calculated. For this pump, the flow rate is accurate to ± 0.02 cc/hr. A comparison was made with the average flow rate calculated by measuring the amount of water collected for a known time, and the difference between the two flow rates was less than 0.01%. In the case of the low-pressure pump, the pump is controlled by the computer and the volume flow rate to be dispensed per minute is specified. The pump auto adjusts the speed that ranges from 60 rpm to 600 rpm to attain the required pressure. The difference between the dispensed flow rate and the measured flow rate was less than 0.5%. However, the shortcomings of this pump were that the tubes developed cracks when operated at the highest speed and no microfilter could be used as the pressure drop across the microfilter is greater than 100 psi. In addition to these two, a magnetic flow sensor is used to measure the flow rate through the microchannels. As the flow is established through the sensor, a small piston is displaced proportional to the volumetric flow rate. A

transducer senses the displacement of the piston as flow increases or decreases. A conditioning circuit converts the transducer signal to either an analog or a digital output. In this case, the output is an analog signal. The calibration and the specifications of the flow sensor used are given in appendix I.

7.4. Temperature measurement:

Thermocouples are used to measure temperature. The temperature was measured at five different places. Two T-type miniature probe thermocouples (80 μm thick) were used to measure the inlet and the outlet temperature of water at microchannel inlet and outlet. Three T-type micro-size thermocouples (40 μm thick) were used to measure the surface temperature of the microchannel plate. Thermocouples were made by spot welding two different metal wires, copper vs. copper-nickel alloy (constantan). The thermocouples used have a very good linear response in the range of temperatures encountered, which are less than 200°C. The temperatures of the water flowing through the microchannel is not expected to go above the boiling point since the surface temperature is expected to be less than 200°C. From typical voltage temperature characteristics of thermocouples, for up to 200°C the emf output of T-type thermocouples is less than 10 mV. This results in a significant gain refinement (100 in this case) for the data acquisition system. Hence, more accurate voltage measurement can be acquired. The reference for the thermocouples is the 'Cold Junction Compensation Sensor' of the data acquisition board.

7.5. Measurement of electrokinetic parameters

The electrokinetic parameters that were measured include streaming potential across the ends of the microchannel, streaming current, electrical conductivity and the

ionic concentration of water. As the streaming potential is the induced potential due to the presence of the electrical double layer, therefore, the measurements are typical and very difficult. The magnitude of the potential is in few milli-volts to hundreds of milli-volts, and the current is very low from few pico-amps to few micro-amps. This inherently makes the measurements quite complicated. Due to the magnitude and the nature of measurement, the first and the foremost restriction it places is about the material of the flow cell. The material has to be non-conducting and at the same time withstand high pressures. A flow cell of pixie-glass with two symmetrical sides was fabricated. A small rectangular slot equal to the cross-sectional area of the microchannel plate was cut on both parts of the cell, and the microchannel was placed in between them. After placing the microchannel plate between the two cell parts, the channel plate was glued using a high temperature epoxy. Two AgCl electrodes with a tip of 0.45 mm were placed on the inlet and outlet of the microchannel. The electrodes were connected to a Keithley® 6517A electrometer by tri-axial cable. The specifications of the electrometer are given in appendix I. As the liquid is made to pass through the microchannel, the accumulation of the ions up-stream and down-stream setup an electrical field, with a potential equal to the streaming potential and that is the potential being measured with the electrodes. The streaming current being measured is the current setup due to this electrical field. The streaming current and voltage were being simultaneously measured by the electrometer that is remotely controlled, through a GPIB interface, as will be explained later in Data Acquisition and Control. However, it must be noted that the measurements were made only for a small fraction of time, as the electrodes can not be kept connected, which results in their polarization. To avoid possible polarization, a switch is used and it is

switched on only during the time the measurements were taken. Besides, the direction of the flow is also reversed, so that the streaming potential and current were measured in both directions. This reversal of the direction also helps in avoiding polarization.

7.6. Conductivity measurement:

The electrical conductivity is simple to measure nevertheless an important electrolyte property. A conductivity sensor, InPro[®] 7001/120 was connected to a CR 7300 Mettler-Toledo[®] conductivity / resistivity transmitter. The detailed specifications of the sensor and the transmitter are given in appendix I. A small conductivity cell was fabricated in which the conductivity sensor was placed. The cell was connected to the water outlet of the flow cell (in both the directions) so that the conductivity can be measured and monitored. The output of the transmitter was displayed on the LCD panel of the transmitter in addition to an analog signal being sent to the DAQ board.

7.7. Micro heater

A heater of equal dimensions to the size of the plate in which microchannel are etched is to be fabricated to supply the necessary heat flux to be removed by the liquid flowing in the microchannels. The effective size of the heater is (1cm x 2.8cm). The heater chosen for the application is a stainless steel sheet (25 microns thick) through which a large current (~20A) at a low voltage (5V) was passed to generate the required heat flux.

7.8. Microfilter

The microchannel hydraulic diameters used in this study range from 30 μm to 250 μm . Therefore any small impurity will very easily block the microchannel. To avoid any

possible impurity from going into the microchannel a 0.1 μm submicron filter was used at the microchannel inlet.

7.9. Microchannel manufacture by silicon micromachining

The microchannels used in the study were manufactured by silicon micromachining at Alberta Microelectronic Center, Edmonton Alberta. Micromachining is a process that enables precise three-dimensional shapes on different materials, e.g. silicon, oxides, nitrides, polysilicon and metals (often referred to as substrates). Presently the technology allows control of dimensions from few micrometers to a few millimeters with a tolerance of less 0.5 μm . These microfabrication techniques are also used to manufacture flow channels ranging in depth from a few thousand angstroms to hundreds of microns. Most of the devices and systems are fabricated using silicon, that is arguably the world's best-characterized semiconductor material due to its electrical and mechanical properties, shown and compared with other commonly used materials in Table 7.1. The micromachining processes are different and relatively difficult compared to the traditional machining processes. The characteristics of a typical micromachining process (etching) are compared to the conventional mechanical milling process in Table 7.2. Various microfabrication processes are being used to manufacture microchannels. However, the two processes that were used to fabricate microchannels used in this study are discussed.

7.9.1. Etching process:

Many crystalline materials have etching rates that vary with crystalline orientation for some etchants. Because of this, the material is removed (etched) faster from some orientations. If the crystals can be made large enough, then this orientation can be

Table 7.1: Comparison of the mechanical properties of silicon with other commonly used materials

Material	Yield Strength 10^9 N/m^2	Knoop Strength kg/mm^2	Young's Modulus 10^{11} N/m^2	Density g/cm^3	Thermal Conductivity $\text{W/cm } ^\circ\text{C}$	Thermal Expansion $10^{-5} / ^\circ\text{C}$
Diamond	53	700	10.35	3.5	20	1
Silicon Carbide	21	2480	7	3.2	3.5	3.3
Silicon Nitride	14	3486	3.85	3.1	0.19	0.8
Iron	12.6	400	1.96	7.8	0.803	12
Silicon	7	850	1.9	2.3	1.57	2.33
Tungsten	4	485	4.1	19.3	1.78	4.5
Stainless Steel	2.1	660	2	7.9	0.329	17.3
Molybdenum	2.1	275	3.43	10.3	1.38	5
Aluminum	0.17	130	0.7	2.7	2.36	25

Table 7.2: Comparison of etching to conventional milling process

Etching	Milling
Single Crystal Silicon	Polycrystalline Metals
Parallel Process	Serial Process
No Induced Stresses	Induced Stresses
Smooth Finish	Rough Finish
Lithography / etch	Cutting Tools
Bonding	Welding
Pre-determined shapes	Shape Flexibility
Sharp Corners	Rounded Corners

advantageously used to make microchannels. Several etchants and materials (primarily single crystalline semiconductor materials) are used, like silicon, gallium, Indium Phosphate etc. Prior to an actual etching, microstructures are outlined on wafers by means of photolithographic process, typically involving the transfer of a pattern from a

master plate (mask) to the wafer. The mask is designed on a computer based on the requirements with L-Edit (special package for designing the microfabrication layout).

The different steps in the photolithography technique are:

- The entire wafer is covered with a masking layer such as silicon dioxide or silicon nitride on top of which is added a photo resist coating.
- The wafer is exposed to the ultra-violet light through a mask which has been imprinted with the desired pattern
- After developing the photoresist layer that has been exposed, the unprotected parts of the masking layer are removed in order to expose the substrate for etching. This enables in selective removal of the material.

The etching process can be classified as isotropic etching, anisotropic or a combination of both, and can be accompanied by either wet chemical or dry etching techniques. The essential variables in selecting a particular etching process are controllability of lateral dimensions, convenient indication of the etched end-point, uniformity across the wafer and repeatability.

In isotropic chemical etching, the etching rate is identical in all directions and the lateral dimensions can not be easily controlled because of the undercutting under the masking layer as shown in Figure 7.1. Isotropic etching is very sensitive to etching conditions and is not widely used for precision micromachining but is used for bulk material removal, like thinning of wafers etc. in HF and CH_3COOH mixtures.

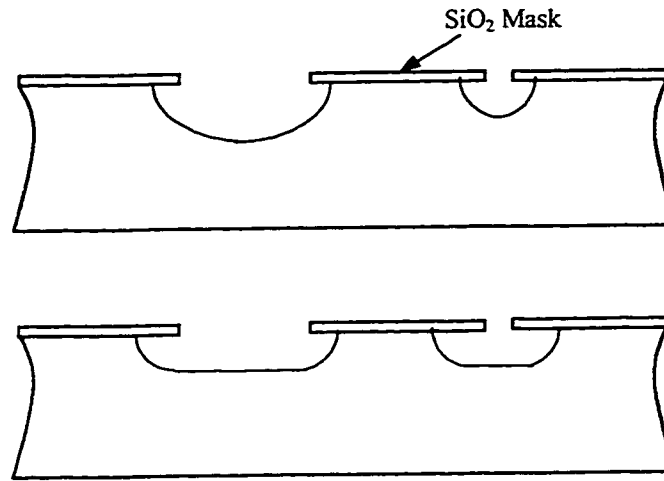


Figure 7.1: Isotropic chemical etching of silicon

In anisotropic chemical etching, as shown in Figure 7.2, the etch rate depends on the wafer's crystallographic orientation and impurity doping density. An anisotropy ratio of

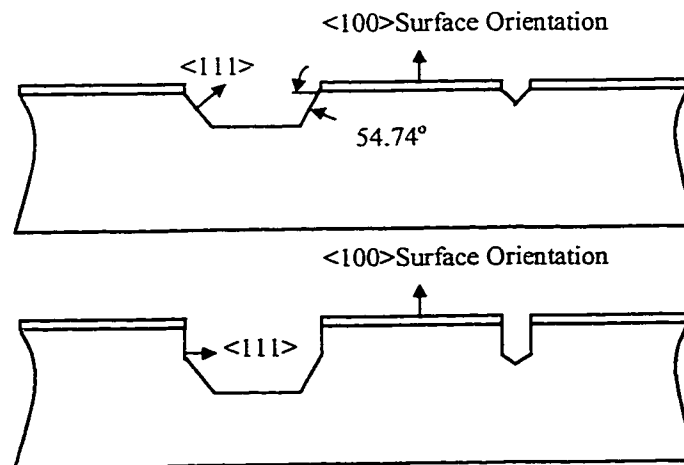


Figure 7.2: Anisotropic chemical etching of silicon

100: 1 is possible in $\langle 100 \rangle$ direction relative to the $\langle 111 \rangle$ direction. An etch process can be made selective by dopants (heavy doped regions etch more slowly), or may even be halted electrochemically (etching stops upon encountering a region of different polarity

in a biased p-n junction). Once the channels are etched in the wafer, stripping and cleaning is done and the wafer is anodically bonded to Pyrex and finally diced by a precision saw. It is the most common method used in silicon micromachining in KOH and EDP (ethylene diamine pyrocatechol). The drawback of this traditional bulk micromachining is that the geometry of the structures is restricted by the aspect ratios inherent in the fabrication methods, so the dimensions are slightly larger than initially designed in the mask layout. The microchannels used in this study were fabricated using anisotropic etching, and a schematic of the mask designed for microchannel etching is shown in Figure 7.3.

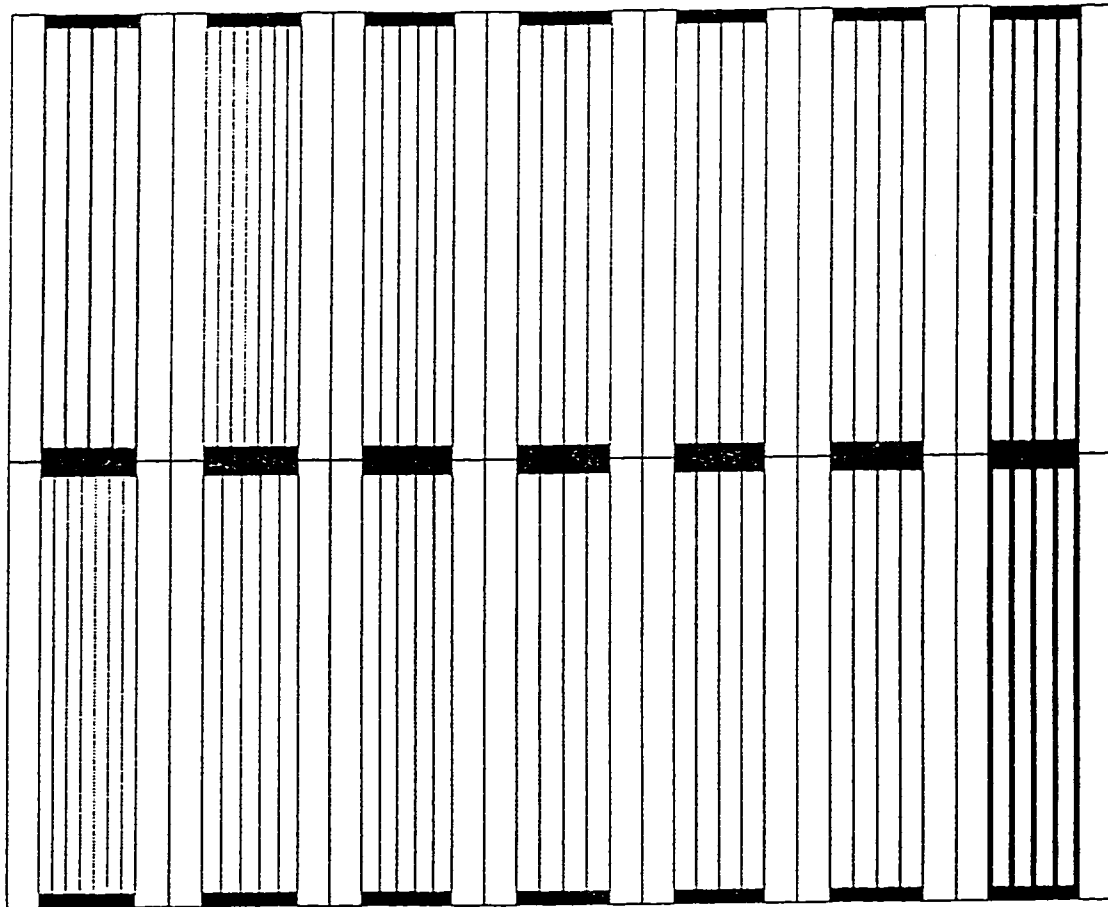


Figure 7.3: Layout of the microchannel mask as designed in L-edit for anisotropic chemical etching of trapezoidal silicon microchannels

It can be seen from Figure 7.3, that a common opening is provided to all the microchannels on one plate. This common opening results in negligible inlet and outlet losses besides acting as a sump for flow inlet and outlet, which is desired for electrokinetic measurements. In addition to this, the common opening has the advantage of minimizing the risk of microchannel blocking while dicing individual plate from the wafer.

Anisotropic etching produces smooth microchannels. The roughness varies from few Angstroms to about a micrometer. However, it has been found that the surface roughness is maximum for the <100> plane of the material being etched, (silicon). The roughness depends on the depth of etch, or in other words the time taken for etching.

7.9.2. Precision sawing:

The precision sawing of microchannels with conventional semiconductor dicing saws can often be used as an alternative to orientational etching. Precision sawing is generally insensitive to crystal orientation and is therefore a good alternative when the channels must be oriented along crystal orientation not suited for etching. Tuckerman (1984) fabricated microchannels using a 'Tempress 602' dicing saw with diamond impregnated metallic blades, at 2500 rpm or faster. Channel uniformity of 2% can generally be obtained. We tested some microchannels made with precision sawing. However, the microchannels were not used because the channels were irregular and very rough, average roughness being of the order of micrometers. Besides, due to the non-availability of small blades, only channel widths in excess of 150 μm could be made.

7.10. Bonding materials to silicon chips

In order to confine the liquid within the microchannels, some sort of cover plate must be bonded to the top of the silicon plate on which microchannels are etched. The bonding technique must provide a leak tight seal at normal operating pressures and temperatures. Pressures as high as 2500 psi and temperatures up to 100°C were encountered. Furthermore, the thermal expansion coefficient of the cover plate should be well matched to that of the silicon. Silicon would be the ideal choice for a cover plate. A technique for bonding silicon to silicon has been reported in literature but was not available at the AMC laboratory.

Another possible technique for bonding the silicon or glass plates on which channels were etched to the cover plate is to use epoxy resin. In order to achieve a sufficiently thin layer so as not to clog the microchannels, the plates needed to be spun in the same way as the photoresist is spun on the wafer. The technique has been described in detail by Tuckerman (1984). But as the microchannels used in this study were much smaller than used by Tuckerman, this method was not used because a small irregularity in the texture of the resin film could very easily clog the microchannel. Further more, epoxy resin bonding can not be used for very high pressure or heat transfer measurement as the epoxy would peel at temperatures above 90°C.

The bonding technique that is clean and gave very satisfactory results was "anodic bonding", which is a well-established technique for bonding glass to silicon or to certain other metals, Wallis and Pomerantz (1969), Wallis (1970) and Brownlow (1978). The thickness of the silicon wafers is less than 0.5 mm, whereas the Pyrex glass is thick, more than a 1 cm. Therefore, the Pyrex is machined first and then polished before being used

for bonding. After etching and sawing silicon and glass as required, they are washed in a high-pressure washer. The surfaces are then thoroughly cleaned and placed in contact and heated to about 400°C, at which temperature the glass is conductive and beginning to soften. A dc potential of several hundred volts is applied across the materials with the silicon as anode. The large electrostatic attraction estimated to be greater than 350 psi, possibly combined with the resistive heating associated with the ionic current in the glass, results in a gradual fusion of the surface. Anodic bonding does not employ any adhesive layer. Borosilicate glass such as Pyrex 7740 is used when anodically bonding to silicon, because the thermal expansion mismatch is very small.

7.11. Data acquisition and control

Data acquisition and control is an important part of any experiment. After installing all the components of the experiment, it was important to understand what is being recorded, and how accurately are the parameters measured. In order to understand what exactly is the state of the system, simultaneous measurements must be taken, and an average of the output over a period must be taken. This can be easily achieved using Data Acquisition Boards and GPIB interfaces.

7.11.1. Data acquisition card (DAQ)

For acquiring data with the help of a computer, a data acquisition card, PCI-MIO-16E-4, from National Instruments® is used. These DAQ boards are completely software configurable. Data acquisition related configuration settings like analog input polarity and range, analog input mode and others are performed. The analog input section of the board is also software configurable, and nonreferenced single-ended analog input

configuration is selected for different measurements. This provides 16 data acquiring channels.

The DAQ board can be operated with two input polarities-unipolar and bipolar. The unipolar and bipolar ranges are 0 to 10 V and ± 5 V respectively. The polarity ranges are set as per the incoming signal through LabView, thus allows configuring each channel uniquely. The software-programmable gain on the board increases its flexibility by matching the input signal ranges thus utilizing the variable gains for each channel as required. For example for measurement of the temperature, if the expected output voltage range is 0-100 mV, therefore a gain of 100 can be used for those channels. This enables to measure the signal with a precision of 24.41 μ V. For all the channels used in data acquisition the gain varies from 100 to 2.0, being highest for the temperature measurement and lowest for the pressure measurement. The precision with which the output signal is measured varies from 24.41 μ V to 2.44 mV.

7.11.2. GPIB interface

The Keithley 6517A electrometer is remotely controlled by a AT-GPIB/TNT (PnP) card from National Instruments®, which is a standard interface for communication between instruments and controllers. It contains information about electrical, mechanical, and functional specifications. The GPIB is a digital, 8-bit parallel communications interface with data transfer rate of 1 Mbytes/s and above. GPIB devices communicate with the controller (usually a computer) which maintains communication links and sending GPIB commands to devices. The data is transferred through digital input-output lines, which also carry the command messages. The GPIB used has a total of eight digital input-output data lines.

7.11.3. LabView

Labview software is used to control the DAQ and GPIB cards. LabView features interactive graphics, state of the art user interface, and a powerful graphics programming language. LabView includes libraries of functions and development tools designed specifically for instrument control and data acquisition. In fact, LabView adheres to the concept of modular programming where applications are divided into a series of tasks, which can be further subdivided to simplify the overall task. With this, a VI is built to accomplish each sub-task and then combine those VIs on another block diagram to accomplish a larger task. Finally, the top level VI contains a collection of subVIs that represent application functions. Each VI corresponds to programmatic operation such as configuring, reading from, writing to, or triggering the instrument. This makes acquisition and control easy and more efficient.

7.12. Procedure

During the experiment, utmost care was taken that the system was clean with no particles or dust to avoid any contamination that can possibly effect the measurement process. Depending on the expected pressure drops and flow rate ranges one of the two pumps was used. If the expected pressure drop was higher than 40 psi, the precision-pump was used. Depending on the direction of the flow i.e. from left to right or right to left, the appropriate valves were opened or closed. The zero reading of all the meters and sensors was noted to zero-check the readings later. After making all the necessary connections, the pump was switched on and the flow was monitored for some time. Care was taken to eliminate the neutralization of the electrodes by taking only few readings of streaming potential and current, only when the steady state was reached and then

disconnecting the triaxial cable connection to the electrometer. The process was repeated until the end of the experiment after every 5 to 10 minutes. The data acquisition VIs are stopped only after the experiment was complete. As a comparison for flow rates the final pump scale reading were noted and the flow rate was calculated. The experiments were repeated in the opposite direction. For every experiment, repeatability tests were performed.

7.10. References

1. Brownlow J. M., 1978, Glass related effects in field assisted glass metal bonding, Tech. Report RC 7101 (#30435), IBM.
2. Tuckerman, D.B., (1984), 'Heat transfer microstructures for integrated cooling,' Ph.D. Thesis, Stanford University, Stanford, CA.
3. Wallis G. and Pomerantz D.I., 1969, Field assisted glass-metal sealing, Journal of Applied Physics, Vol. 40. Pp. 3946-3849.
4. Wallis G., 1970, Direct current polarization during field assisted glass metal bonding, J. Amer. Ceram. Soc., Vol 53, pp. 563-567.

Chapter 8 Fluid Flow and Heat Transfer Characteristics of Water in Trapezoidal Silicon Microchannels

8.1. Introduction

As the hydraulic diameter of channels or tube decreases, the fluid flow behavior is influenced by the wall effects. These effects were demonstrated by Gee et al (1990), and Chan and Horn (1985) by studying liquid film flow; Anderson and Quinn (1972), Debye and Cleland (1959) for flow through porous media; Mala et al (1997, 1996), Peng et al (1994a, 1994b), Pfahler (1992), Tuckermann (1984), and Wu and Little (1983) for flow in microchannels; Mala and Li (1998), and Choi et. al (1991) for flow in microtubes. Due to the increasing applications of microscale fluid flow and heat transfer in number of MEMS devices and systems, research on fluid flow and heat transfer in these microchannels is important to understand the fundamental characteristics. Some of the practical applications are, thermal control and cooling of high density electronic chips and devices, mini-heat exchangers, bioengineering devices, micro-fluidic devices, and so on.

The concept of the microchannel heat sinks was introduced by Tuckermann (1984). A detailed review of several other research works on microchannel heat sinks can be found elsewhere, Philip (1990). However, for an effective design of these microscale devices, it is necessary to understand the flow characteristics. Because only after obtaining the velocity distribution can, the energy equation be solved to determine the heat transfer characteristics. However, conventional transport theories cannot explain many phenomena associated with the microscale flow. For example, Eringen (1964) proposed a theory, which states that fluid flow in microchannels will deviate from that

predicted by Navier-Stokes Equations. Pfahler (1992) measured the friction coefficient in microchannels, and found a significantly higher flow rate than expected for both isopropanol and silicon oil. His results indicate that polar nature of the fluid may play a role in the change in the observed viscosity. Choi et al (1991) measured friction factor in microtubes of inside diameters 3 to 81 μm using nitrogen gas. They found that for diameters smaller than 10 μm , the friction factor constant is $C_f = 53$, instead of 64. Harley and Bau (1989) measured the friction factor in channels of trapezoidal and square cross-sections. They found experimentally that C_f ranged from 49 for the square channels to 512 for the trapezoidal channels. Peng et al (1994a, 1994b), found experimentally that transition to turbulent flow began at $\text{Re} = 200$ to 700, and that fully turbulent convective heat transfer was reached at $\text{Re} = 400$ to 1500. They also observed that transitional Re diminished as the size of the microchannel decreased. Wang and Peng (1994) concluded that these effects in small channels were largely due to changes in thermophysical properties because of high heat fluxes. Mala et al (1996, 1997), Yang and Li (1997) found that electrokinetic effects partially explain these effects, as they are significant for small microchannels. But for microtubes, the experimentally measured pressure gradients are much higher than predicted by conventional theory. They explained that these effects are either due to change in the flow mode, from laminar to turbulent at lower Reynolds numbers or due to the effects of surface roughness. They developed a mathematical model that incorporates the effects of surface roughness in laminar flow. Therefore, it is safe to conclude that microscale flow needs further investigation to seek answers to these conflicting observations reported in pertinent literature.

8.2. Poisson-Boltzmann equation

In order to consider the electroviscous effects at the solid-liquid interface on fluid flow in microchannels, the distribution of electrical potential and the net charge density must be determined. Consider a liquid phase containing positive and negative ions in contact with a planar positively or negatively charged surface. The surface bears a uniform electrostatic potential, which decreases as one proceeds out into the fluid. Far away from the wall, the concentration of the positive and negative ions is equal. The electrostatic potential Ψ , at any point near the surface is related to the net number of electrical charges per unit volume ρ_e , in the neighborhood of the point, which measures the excess of the positive ions over negative ions or vice versa. According to the theory of electrostatics, the relation between Ψ and ρ_e is given by the Poisson's Equation. For a flat surface the Poisson equation is given below, Hunter (1981):

$$\nabla^2 \Psi = -\frac{\rho_e}{\epsilon \epsilon_0}$$

For a microchannel, as shown in Figure 8.1, the Poisson Equation in Cartesian coordinates can be written as:

$$\frac{\partial^2 \Psi}{\partial Y^2} + \frac{\partial^2 \Psi}{\partial Z^2} = -\frac{\rho_e}{\epsilon \epsilon_0} \quad (8.1)$$

The probability of finding an ion at a particular point is proportional to the Boltzmann factor $e^{\frac{z_e e \Psi}{k_b T}}$. For any fluid consisting of two kinds of ions of equal and opposite charge z_v^+ , z_v^- , the number of ions of each type are given by the Boltzmann Equation, Hunter (1981)

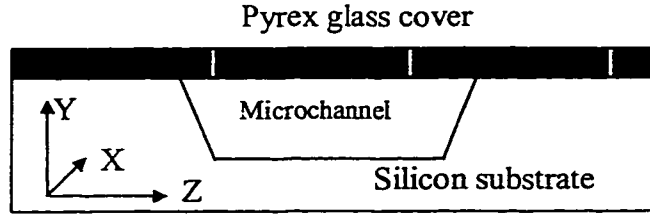


Figure 8.1: Schematic of a trapezoidal microchannel in silicon with a Pyrex glass cover plate.

$$n^- = n_o e^{\frac{z_v e \Psi}{k_b T}} \text{ and } n^+ = n_o e^{-\frac{z_v e \Psi}{k_b T}} \quad (8.2)$$

The net charge density in a unit volume of the fluid is given by

$$\rho_e(Y, Z) = (n^+ - n^-) z_v e = -2n_o z_v e \sinh(z_v e \Psi / k_b T) \quad (8.3)$$

Substituting Equation (8.3) in Equation (8.1), we obtain a nonlinear second-order two-dimensional Poisson-Boltzmann Equation.

$$\frac{\partial^2 \Psi}{\partial Y^2} + \frac{\partial^2 \Psi}{\partial Z^2} = \frac{2n_o z_v e}{\epsilon \epsilon_o} \sinh\left(\frac{z_v e \Psi}{k_b T}\right) \quad (8.4)$$

Nondimensionalizing Equation (8.4) via

$$y = \frac{Y}{d_h}, \quad z = \frac{Z}{d_h}, \quad \psi = \frac{z_v e \Psi}{k_b T} \quad (8.5)$$

a nondimensional form of the Poisson-Boltzmann Equation is obtained and is given as:

$$\frac{\partial^2 \psi}{\partial y^2} + \frac{\partial^2 \psi}{\partial z^2} = \kappa^2 \sinh \psi \quad (8.6)$$

Where

$$\kappa = d_h k_e,$$

$$k_e = \left(\frac{2n_o z_v^2 e^2}{\epsilon \epsilon_o k_b T} \right)^{1/2}$$

' k_e ' is called the Debye-Huckel parameter, and ' $1/k_e$ ' is usually referred to as the characteristic thickness of the EDL.

8.3. Equation of motion

Consider laminar fluid flow in a two-dimensional trapezoidal microchannel as shown in Figure 8.1. The equations of motion for incompressible liquid flow is given by:

$$\rho \frac{\partial \mathbf{u}}{\partial t} + \rho (\mathbf{u} \cdot \nabla) \mathbf{u} = -\nabla P + \mathbf{F} + \mu \nabla^2 \mathbf{u} \quad (8.7)$$

For a steady state, fully developed flow, the components of the velocity vector \mathbf{u} satisfy $u=u(Y,Z)$ and $v=w=0$ in terms of the Cartesian coordinates. For the case of steady state, both the convection terms vanish. The pressure gradient dP/dX is constant, as P is a function of flow direction only. Neglecting the effects of gravity, the body force \mathbf{F} is due to the electrical field E_x resulting from the presence of electrical double layer at the solid liquid interface. The strength of this induced electrical field is given as

$$\mathbf{F} = F_x = E_x \rho_e(Y,Z) = E_s \rho_e(Y,Z) / L \quad (8.8)$$

Therefore, with these considerations Equation (8.7) reduces to

$$\frac{\partial^2 u}{\partial Y^2} + \frac{\partial^2 u}{\partial Z^2} = \frac{1}{\mu} \frac{dP}{dX} - \frac{1}{\mu} \frac{E_s \rho_e(Y,Z)}{L} \quad (8.9)$$

Using the following non-dimensional parameters

$$\begin{aligned} x = \frac{X}{d_h}, \quad y = \frac{Y}{d_h}, \quad z = \frac{Z}{d_h}, \quad l = \frac{L}{d_h}, \quad p = \frac{P}{\rho U^2}, \quad \bar{u}(y,z) = \frac{u(Y,Z)}{U} \\ \bar{E}_s = \frac{E_s}{\xi}, \quad \bar{\rho}_e(y,z) = \frac{\rho_e(Y,Z)}{n_o z_v e}, \quad \text{Re}_{ref} = \frac{\rho U d_h}{\mu} \end{aligned} \quad \{8.10\}$$

the non-dimensional form of Equation (8.9) is obtained and is given as:

$$\frac{\partial^2 \bar{u}}{\partial y^2} + \frac{\partial^2 \bar{u}}{\partial z^2} = \text{Re} \frac{d\bar{p}}{dx} - F_1 \bar{E}_s \bar{\rho}_e(y, z) \quad (8.11)$$

Where

$$C = \text{Re}_{ref} \frac{dp}{dx} - F_1 \bar{E}_s \bar{\rho}_e(y, z) \quad (8.12)$$

$$F_1 = \frac{n_o z_v e \xi d_h^2}{\mu l U} \quad (8.13)$$

For fluid flow without considering the electrokinetic effects, the constant F_1 is zero. In the following discussion for non-dimensional quantities, the over-bar sign will be omitted.

8.4. Streaming potential

To determine the local and the mean velocity, the streaming potential should be known. This is the induced electrical potential per unit length, and is a steady state potential difference, which builds across the microchannel. When a liquid is forced under hydrostatic pressure through a microchannel, the ions in the mobile part of the double layer are carried downstream. This causes an electrical current called the streaming current to flow in the direction of the flow. This accumulation of ions sets up an electrical field with an electrokinetic potential called the streaming potential. This field generates a current, called the conduction current, to flow back in the opposite direction. When the two currents are equal, a steady state is reached. The net current flowing in the flow direction of the microchannel is the sum of convection current i.e. streaming current and the electrical conduction current i.e. conduction current. At a steady state, the net current should be zero.

$$I = I_s + I_c = 0 \quad (8.14)$$

The streaming current is given as

$$I_s = \int_{A_c} u(Y, Z) \rho_e(Y, Z) dA_c \quad (8.15)$$

The conduction current is given as

$$I_c = \frac{E_s \lambda_T A_c}{L} \quad (8.16)$$

Where,

$$\lambda_T = \lambda_b + \frac{\lambda_s P_s}{A_c} \quad (8.17)$$

Non-dimensionalizing the conduction and streaming currents, substituting in Equation (8.14), the nondimensional form of the streaming potential is obtained which can be written after some simplification as:

$$\bar{E}_s = \frac{2n_o l_z v_e U}{\xi \lambda_T A_c} \int_{\bar{A}_c} \bar{u}(y, z) \psi(y, z) d\bar{A}_c \quad (8.18)$$

$$\text{where, } \bar{A}_c = \frac{A_c}{d_h^2}.$$

8.5. Solution of governing equations

The governing equations that determine the fluid flow characteristics of water through a microchannel with and without electrokinetic effects are given by Equations (8.6, 8.11 and 8.18). The Poisson-Boltzmann Equation is a two-dimensional, second-order, nonlinear partial differential equation. Therefore, an analytical solution is not possible. However, this equation can be solved either by making use of Debye-Huckel approximation or numerically. Both types of solutions are discussed in Mala et al (1998). The equation of motion with electrical body force source term, is also a non-linear two-

dimensional, second-order partial differential equation. Therefore, an analytical solution is not possible. Besides, to solve the equation of motion the streaming potential should be known first. Nevertheless, the streaming potential is a function of the velocity $u(y,z)$ in the flow direction. The equations are solved numerically by finite difference with the wall boundary conditions, given as, $u(y,z)=0$ and the surface potential, $\Psi(Y,Z)$ is equal to the zeta potential, ξ at the walls of the microchannel. Successive overrelaxation is employed to solve these equations, and the values are updated after every iteration until convergence is achieved. The solution of the Poisson-Boltzmann Equation is used to calculate the charge density given by Equation (8.3). The previous value of the velocity is used to calculate the streaming potential and then the values of the velocity distribution are updated along with the streaming potential.

However, it must be remembered that the actual cross-section of the microchannel is trapezoidal, and therefore to solve the PBE and equation of motion for the microchannel with a constant step size a transformation should be made that converts the trapezoidal cross-section into a square or rectangular cross-section. The governing equations should also be re-written in the transformed computational coordinates before employing the finite difference formulation.

8.6. Transformation of actual non-uniform (y, z) to uniform (η, ζ) coordinates

The microchannels used in this study are of trapezoidal cross-section and therefore, a constant step size can not be used. This results in an unstructured non-uniform numerical grid. The unstructured grids are difficult and inefficient to work with.

However, a transformation can be made here to change the unstructured grid to a square one. The transformation is given by:

$$\eta = \frac{2hy - (a-b)z}{2ha - 2(a-b)z}, \text{ and } \zeta = \frac{z}{h} \quad (8.19)$$

which transforms the trapezoidal cross-section of the microchannel to a square of unit sides as shown in Figure 8.2. From Equation (8.19), (y, z) can be expressed as functions of the transformed axes (η, ζ) as the reverse transformation is given by:

$$y = \eta(a - (a-b)\zeta) + \frac{a-b}{2}\zeta, \text{ and } z = h\zeta \quad (8.20)$$

The step sizes used in (η, ζ) coordinates are:

$$\Delta\zeta = \frac{1}{m-1}, \quad \Delta\eta = \frac{1}{n-1} \quad (8.21)$$

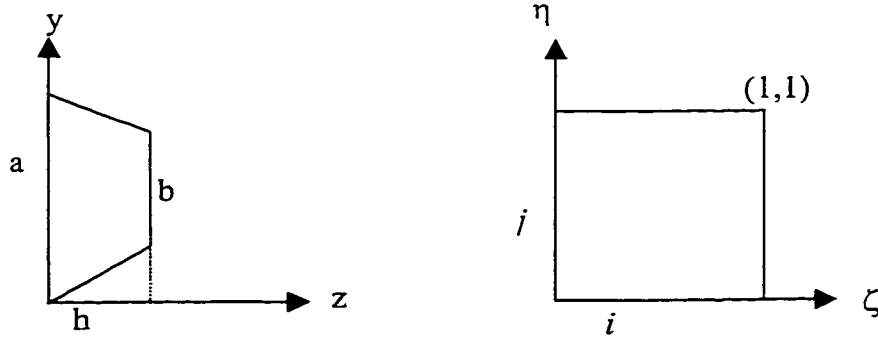


Figure 8.2: Transformation of the coordinates from (y, z) to (η, ζ) .

and the corresponding step sizes in the actual non-dimensional axes (y, z) can be written as:

$$\Delta y = \frac{a(m-1) - (a-b)(i-1)}{(m-1)(n-1)}, \quad \Delta z = \frac{h}{m-1}, \quad (8.22)$$

The equation of motion and the Poisson-Boltzmann Equation should be transformed from the (y, z) coordinate system to (η, ζ) coordinate system. In order to do that, the following partial differential relations for the multivariable functions are employed.

$$\frac{\partial \zeta}{\partial z} = \frac{1}{J} y_\eta, \quad \frac{\partial \eta}{\partial z} = -\frac{1}{J} y_\zeta, \quad \frac{\partial \zeta}{\partial y} = -\frac{1}{J} z_\eta, \quad \frac{\partial \eta}{\partial y} = \frac{1}{J} z_\zeta \quad (8.23)$$

where,

$$J = \begin{vmatrix} \frac{\partial z}{\partial \zeta} & \frac{\partial z}{\partial \eta} \\ \frac{\partial y}{\partial \zeta} & \frac{\partial y}{\partial \eta} \end{vmatrix} = \frac{\partial z}{\partial \zeta} \frac{\partial y}{\partial \eta} - \frac{\partial z}{\partial \eta} \frac{\partial y}{\partial \zeta} = ah - (a-b)h\zeta \quad (8.24a)$$

$$z_\zeta = \frac{\partial z}{\partial \zeta} = h, \quad z_\eta = \frac{\partial z}{\partial \eta} = 0, \quad (8.24b)$$

$$y_\zeta = \frac{\partial y}{\partial \zeta} = \left(\frac{1}{2} - \eta \right) (a-b), \quad y_\eta = \frac{\partial y}{\partial \eta} = a - (a-b)\zeta \quad (8.24c)$$

where J , is the Jacobi determinant.

8.7. Equation of motion in η and ζ Coordinates

By making use of relations given in Equation (8.23), the first and the second partial derivatives of the velocity with respect to z in terms of the new computational coordinates η and ζ can be expressed as:

$$\frac{\partial u}{\partial z} = \frac{\partial u}{\partial \zeta} \frac{\partial \zeta}{\partial z} + \frac{\partial u}{\partial \eta} \frac{\partial \eta}{\partial z} = \frac{1}{J} \left[\frac{\partial(u y_\eta)}{\partial \zeta} - \frac{\partial(u y_\zeta)}{\partial \eta} \right] \quad (8.25a)$$

$$\frac{\partial^2 u}{\partial z^2} = \frac{1}{J} \left[\frac{\partial}{\partial \zeta} \left\{ \frac{1}{J} \left(\frac{\partial u}{\partial \zeta} y_\eta^2 - \frac{\partial u}{\partial \eta} y_\eta y_\zeta \right) \right\} - \frac{\partial}{\partial \eta} \left\{ \frac{1}{J} \left(\frac{\partial u}{\partial \zeta} y_\eta y_\zeta - \frac{\partial u}{\partial \eta} y_\zeta^2 \right) \right\} \right] \quad (8.25b)$$

Similarly, the derivatives with respect to y can be written as:

$$\frac{\partial u}{\partial y} = \frac{1}{J} \left[\frac{\partial(u z_\zeta)}{\partial \eta} - \frac{\partial(u z_\eta)}{\partial \zeta} \right] \quad (8.26a)$$

$$\frac{\partial^2 u}{\partial y^2} = \frac{1}{J} \left[\frac{\partial}{\partial \eta} \left\{ \frac{1}{J} \left(\frac{\partial u}{\partial \eta} z_\zeta^2 - \frac{\partial u}{\partial \zeta} z_\eta z_\zeta \right) \right\} - \frac{\partial}{\partial \zeta} \left\{ \frac{1}{J} \left(\frac{\partial u}{\partial \eta} z_\eta z_\zeta - \frac{\partial u}{\partial \zeta} z_\eta^2 \right) \right\} \right] \quad (8.26b)$$

Adding Equations (8.25b) and (8.26b) together, yields

$$\frac{\partial^2 u}{\partial y^2} + \frac{\partial^2 u}{\partial z^2} = \frac{1}{J} \left[\alpha \frac{\partial^2 u}{\partial \zeta^2} + \beta \frac{\partial^2 u}{\partial \eta^2} + \frac{\partial \alpha}{\partial \zeta} \frac{\partial u}{\partial \zeta} + \frac{\partial \beta}{\partial \eta} \frac{\partial u}{\partial \eta} \right. \\ \left. - \frac{\partial \chi}{\partial \zeta} \frac{\partial u}{\partial \eta} - \frac{\partial \chi}{\partial \eta} \frac{\partial u}{\partial \zeta} - 2\chi \frac{\partial^2 u}{\partial \zeta \partial \eta} \right] \quad (8.27)$$

Where

$$\alpha = \frac{z_\eta^2 + y_\eta^2}{J} = \frac{a}{h} - \frac{a-b}{h} \zeta \quad (8.28a)$$

$$\beta = \frac{z_\zeta^2 + y_\zeta^2}{J} = \frac{h^2 + (a-b)^2 (\eta^2 - \eta + \frac{1}{4})}{ah - (a-b)h\zeta} \quad (8.28b)$$

$$\chi = \frac{z_\zeta z_\eta + y_\zeta y_\eta}{J} = \frac{a-b}{h} \left(\frac{1}{2} - \eta \right) \quad (8.28c)$$

$$\frac{\partial \alpha}{\partial \zeta} = -\frac{a-b}{h} \quad (8.28d)$$

$$\frac{\partial \beta}{\partial \eta} = \frac{(a-b)^2 (2\eta - 1)}{ah - (a-b)h\zeta} \quad (8.28e)$$

$$\frac{\partial \chi}{\partial \zeta} = 0 \quad (8.28f)$$

$$\frac{\partial \chi}{\partial \eta} = -\frac{a-b}{h} \quad (8.28g)$$

Making use of Equation (8.28), Equation (8.27) can be expressed as:

$$\frac{\partial^2 u}{\partial y^2} + \frac{\partial^2 u}{\partial z^2} = \frac{1}{J} \left[C_1 \frac{\partial^2 u}{\partial \zeta^2} + C_2 \frac{\partial^2 u}{\partial \eta^2} + C_3 \frac{\partial^2 u}{\partial \zeta \partial \eta} + C_4 \frac{\partial u}{\partial \eta} \right] \quad (8.29)$$

Where

$$C_1 = \alpha = C_1(\zeta), C_2 = \beta = C_2(\eta, \zeta), C_3 = -2\chi = C_3(\eta), C_4 = \frac{\partial \beta}{\partial \eta} = C_4(\eta, \zeta)$$

By substituting Equation (8.29) in the equation of motion, Equation (8.11) transforms to

$$C_1 \frac{\partial^2 u}{\partial \zeta^2} + C_2 \frac{\partial^2 u}{\partial \eta^2} + C_3 \frac{\partial^2 u}{\partial \zeta \partial \eta} + C_4 \frac{\partial u}{\partial \eta} - C J = 0 \quad (8.30)$$

This is the modified momentum equation in (η, ζ) coordinate system.

8.8. Poisson-Boltzmann equation in η and ζ Coordinates

The left hand side of Equation (8.6) is to be transformed from the non-uniform (y, z) coordinates to uniform (η, ζ) coordinates so that the step size is constant for numerical computation. Making use of the Equation (8.29) by replacing the u with ψ the left hand side of the Poisson-Boltzmann Equation, Equation (8.6) can be written in the (η, ζ) coordinates as:

$$\frac{\partial^2 \psi}{\partial y^2} + \frac{\partial^2 \psi}{\partial z^2} = \frac{1}{J} \left[C_1 \frac{\partial^2 \psi}{\partial \zeta^2} + C_2 \frac{\partial^2 \psi}{\partial \eta^2} + C_3 \frac{\partial^2 \psi}{\partial \zeta \partial \eta} + C_4 \frac{\partial \psi}{\partial \eta} \right] \quad (8.31)$$

Therefore, Equation (8.6) can be re-written as

$$C_1 \frac{\partial^2 \psi}{\partial \zeta^2} + C_2 \frac{\partial^2 \psi}{\partial \eta^2} + C_3 \frac{\partial^2 \psi}{\partial \zeta \partial \eta} + C_4 \frac{\partial \psi}{\partial \eta} = J \kappa^2 \sinh \psi \quad (8.32)$$

The hyperbolic function on the right hand side of Equation (8.32) can be written as:

$$\sinh \psi^{k,i,j} = \frac{1}{2} \{ e^{\psi^{k,i,j}} - e^{-\psi^{k,i,j}} \} \quad (8.33)$$

The right hand side of the above equation can be expanded described in Mala, et al (1998) that is:

$$e^{\psi^{k,i,j}} = e^{\psi^{k,i,j}} + [\psi^{k+1,i,j} - \psi^{k,i,j}] e^{\psi^{k,i,j}} \quad (8.34a)$$

$$e^{-\psi^{k,i,j}} = e^{-\psi^{k,i,j}} - [\psi^{k+1,i,j} - \psi^{k,i,j}] e^{-\psi^{k,i,j}} \quad (8.34b)$$

Using Equations (8.33) and (8.34), the right hand side of Equation (8.32) can be written as:

$$J\kappa^2 \sinh \psi_{i,j}^{k+1} = J\kappa^2 (\sinh \psi_{i,j}^k + \psi_{i,j}^{k+1} \cosh \psi_{i,j}^{k+1} - \psi_{i,j}^k \cosh \psi_{i,j}^k) \quad (8.35)$$

Therefore, the modified Poisson-Boltzmann Equation in (η, ζ) coordinate system can be written as

$$C_1 \frac{\partial^2 \psi}{\partial \zeta^2} + C_2 \frac{\partial^2 \psi}{\partial \eta^2} + C_3 \frac{\partial^2 \psi}{\partial \zeta \partial \eta} + C_4 \frac{\partial \psi}{\partial \eta} = J\kappa^2 (\sinh \psi_{i,j}^k + \psi_{i,j}^{k+1} \cosh \psi_{i,j}^{k+1} - \psi_{i,j}^k \cosh \psi_{i,j}^k) \quad (8.36)$$

8.9. Finite difference form of the governing equations

The first and second order derivatives are written in three and five point central difference scheme as:

$$\frac{\partial^2 u}{\partial \zeta^2} = \frac{u_{i+1,j}^{k+1} - 2u_{i,j}^{k+1} + u_{i-1,j}^{k+1}}{\Delta \zeta^2} \quad (8.37a)$$

$$\frac{\partial^2 u}{\partial \eta^2} = \frac{u_{i,j+1}^{k+1} - 2u_{i,j}^{k+1} + u_{i,j-1}^{k+1}}{\Delta \eta^2} \quad (8.37b)$$

$$\frac{\partial^2 u}{\partial \zeta \partial \eta} = \frac{u_{i+1,j+1}^{k+1} - u_{i-1,j+1}^{k+1} - u_{i+1,j-1}^{k+1} + u_{i-1,j-1}^{k+1}}{4\Delta \zeta \Delta \eta} \quad (8.37c)$$

$$\frac{\partial u}{\partial \eta} = \frac{u_{i,j+1}^{k+1} - u_{i,j-1}^{k+1}}{2\Delta \eta} \quad (8.37d)$$

$$\frac{\partial^2 \psi}{\partial \zeta^2} = \frac{\psi_{i+1,j}^{k+1} - 2\psi_{i,j}^{k+1} + \psi_{i-1,j}^{k+1}}{\Delta \zeta^2} \quad (8.37e)$$

$$\frac{\partial^2 \psi}{\partial \eta^2} = \frac{\psi_{i,j+1}^{k+1} - 2\psi_{i,j}^{k+1} + \psi_{i,j-1}^{k+1}}{\Delta \eta^2} \quad (8.37f)$$

$$\frac{\partial^2 \psi}{\partial \zeta \partial \eta} = \frac{\psi_{i+1,j+1}^{k+1} - \psi_{i-1,j+1}^{k+1} - \psi_{i+1,j-1}^{k+1} + \psi_{i-1,j-1}^{k+1}}{4\Delta \zeta \Delta \eta} \quad (8.37g)$$

$$\frac{\partial \psi}{\partial \eta} = \frac{\psi_{i,j+1}^{k+1} - \psi_{i,j-1}^{k+1}}{2\Delta\eta} \quad (8.37h)$$

For $i = 1, 2, \dots, m$, and $j = 1, 2, \dots, n$.

Substituting these derivatives in Equation (8.30) and (8.36), the modified equation of motion and Poisson-Boltzmann Equation, we obtain $(m \times n)$ algebraic equations for velocity u_{ij} and $(m \times n)$ algebraic equations for potential ψ_{ij} , given respectively as

$$u_{i,j}^{k+1} = \frac{\left[\frac{C_1}{\Delta\zeta^2} (u_{i+1,j} + u_{i-1,j}) + \frac{C_2}{\Delta\eta^2} (u_{i,j+1} + u_{i,j-1}) + \frac{C_4}{2\Delta\eta} (u_{i,j+1} + u_{i,j-1}) \right. \\ \left. + \frac{C_3}{\Delta\zeta\Delta\eta} (u_{i+1,j+1} + u_{i-1,j-1} - u_{i-1,j+1} + u_{i+1,j-1}) - C_{i,j} J_{i,j} \right]}{\left[\frac{2C_1}{\Delta\zeta^2} + \frac{2C_2}{\Delta\eta^2} \right]} \quad (8.38a)$$

and

$$\psi_{i,j}^{k+1} = \frac{\left[\frac{C_1}{\Delta\zeta^2} (\psi_{i+1,j} + \psi_{i-1,j}) + \frac{C_2}{\Delta\eta^2} (\psi_{i,j+1} + \psi_{i,j-1}) + \frac{C_4}{2\Delta\eta} (\psi_{i,j+1} + \psi_{i,j-1}) \right. \\ \left. + \frac{C_3}{4\Delta\zeta\Delta\eta} (\psi_{i+1,j+1} + \psi_{i-1,j-1} - \psi_{i-1,j+1} + \psi_{i+1,j-1}) - \kappa^2 J_{i,j} (\sinh\psi_{i,j}^k - \psi_{i,j}^k \cosh\psi_{i,j}^k) \right]}{\left[\frac{2C_1}{\Delta\zeta^2} + \frac{2C_2}{\Delta\eta^2} + J_{i,j} \kappa^2 \cosh\psi_{i,j}^k \right]} \quad (8.38b)$$

The resulting systems of equations are solved for $u_{i,j}^{k+1}$ and $\psi_{i,j}^{k+1}$ by successive overrelaxation, *i.e.*, using the value obtained in the k^{th} iteration, where k is the outer iteration index, represented by superscript k and update its value in next, *i.e.*, $(k+1)^{th}$ iteration, represented superscript $k+1$. A complete numerical solution of the Poisson-Boltzmann Equation and equation of motion can be obtained in this way. The numerical solution was compared with other analytical solutions and for various values of the apex angle ϕ of the trapezoidal silicon microchannel. The numerical results are in a very good

agreement with the analytical results as can be seen from Table 8.1. The numerical results are compared with the results given in Shah and London (1978).

Table 8.1. Comparison of numerical results with analytical results

S. No.	ϕ	a/b	f^*Re (Shah and London)	f^*Re (Numerical Solution)
1	60°	2.0	13.804	13.809
2	45°	2.0	13.364	13.372
3	45°	0.5	15.206	15.212
4	30°	4	12.782	12.789

8.10. Heat transfer coefficient

Consider n number of identical microchannels each of length L (in the flow direction) etched in a silicon substrate of same length and width of 1 cm . The coolant (DIUF) flows in each microchannel, from the common opening at the channel inlet. The coolant absorbs a constant heat flow per unit length \dot{q}/nL from its walls. The coolant is assumed to be incompressible Newtonian fluid, i.e. ρ and C_p are constant. The use of many microchannels increases the surface area which is given by $A_s = npL$. If we assume that at any location along the length of the duct, the walls are at a uniform temperature $T_w(x)$ around the cross-section, then the local convective heat transfer coefficient h_x is defined as

$$h_x = \frac{\dot{q}}{nLp(T_w(x) - T_f(x))} = \frac{Nu_x k}{d_h} \quad (8.39)$$

Assuming a uniform heat capacity (ρC_p) for the coolant, we find from energy conservation that

$$\dot{q} = mC_p(T_{out} - T_{in}) \quad (8.40)$$

Usually the term d_h/Nu_x can be interpreted as the thermal boundary layer thickness, which increases monotonically with increasing x . Therefore, the maximum wall temperature $T_{w,max}$ will occur at the output end of the microchannel plate, i.e. $T_{w,max} = T_w(L)$.

However, due to a significant increase in the temperature of the coolant from microchannel inlet to outlet, the thermophysical properties of the coolant change appreciably. In order to account for the changes in coolant density, specific heat, viscosity, thermal conductivity and Prandtl number the variable property data was taken from Kays and Crawford (1980). To find the value at any intermediate point, the following function was used:

$$f(x) = \sum_{k=1}^n \prod_{\substack{i=1 \\ i \neq k}}^n \left(\frac{x - x_i}{x_k - x_i} \right) y_k \quad (8.41)$$

8.11. Experimental apparatus and procedure

A schematic of the experimental apparatus used to investigate fluid flow and heat transfer in trapezoidal silicon microchannels is shown in Figure 8.3. It consists of a high precision proportioning pump, a microfilter, flow sensor, pressure transducer, flow cell, conductivity meter, two reference electrodes, electrometer, data acquisition system, a micro-heater, thermocouples and adjusting valves. Water was pumped by the high precision pump that has a flow rate range of 2.5-650 cc/hr with a pressure rating of up to 5000 psi. The liquid was made to flow through the microfilter to avoid any impurities from flowing through and blocking the microchannels. The flow rate was measured in

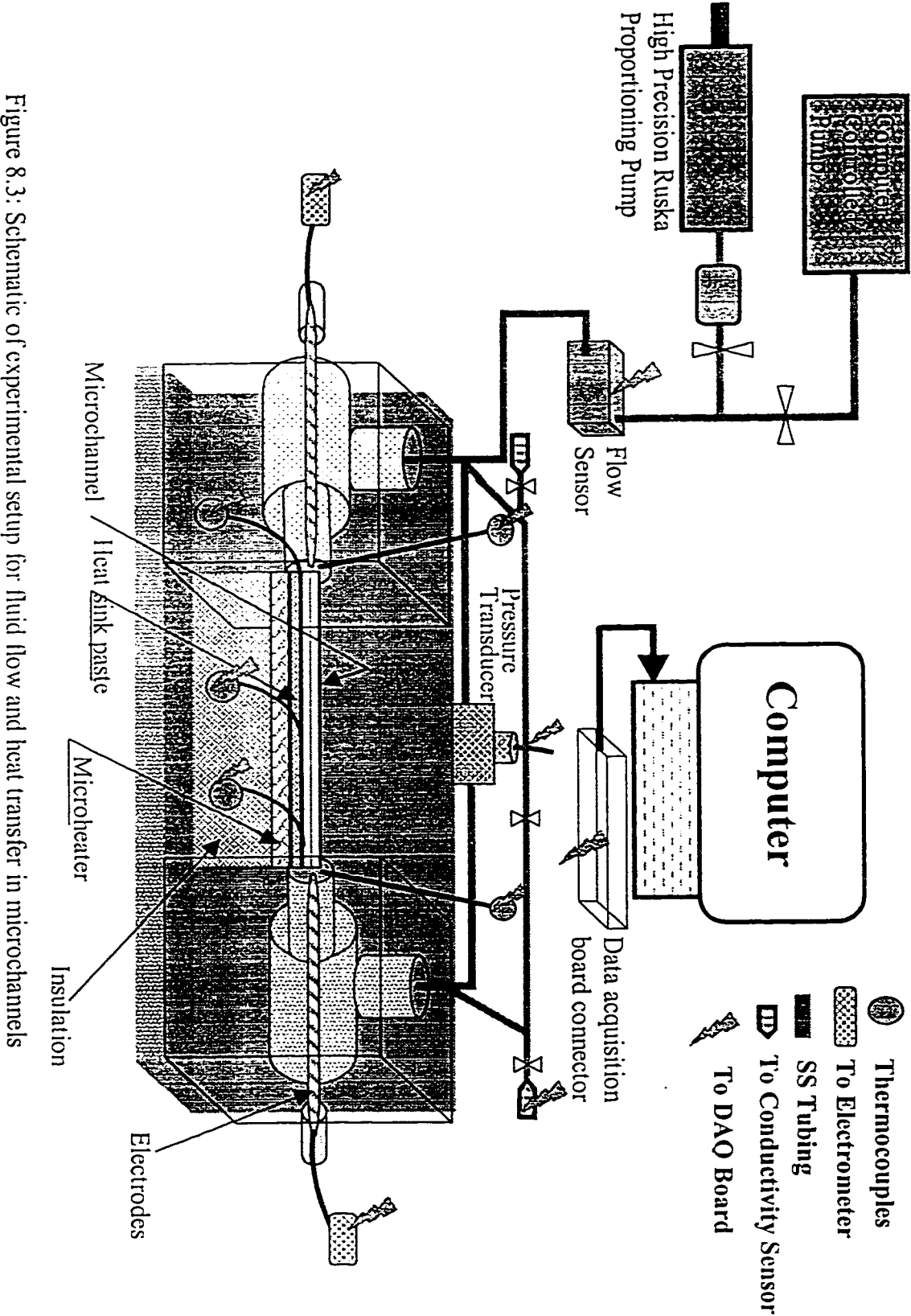


Figure 8.3: Schematic of experimental setup for fluid flow and heat transfer in microchannels

two ways: by the flow sensor and directly reading the displacement of the pump in a particular time. The microchannels are placed in a two-part symmetrical Plexiglas flow cell. The electrodes are placed on the up and downstream of the microchannel. The electrodes are connected to a Keithley 6517A electrometer used to measure the streaming potential and streaming current. The pressure transducer was connected across the microchannel ends to measure the pressure drop across the microchannel. The liquid coming out of the microchannel was made to flow through an InPro conductivity sensor that measures the electrical bulk conductivity of the water. The heater was placed under the microchannel plate. Three thermocouples are attached to the microchannel plate at near inlet, in the middle, and at near outlet of the microchannels. Two 80 μm probe thermocouples are placed on the two ends of the microchannel, one at liquid inlet and the other at the liquid outlet to measure the inlet and outlet temperature of the liquid. All the measurement devices are connected to a data acquisition card. The electrometer was also remotely controlled through a GPIB. Labview was used to control the GPIB and Data Acquisition card and for acquiring data. Throughout the course of the experiment great care was taken to ensure the accuracy and the repeatability of the measured data.

The microchannels used in the investigation were fabricated locally by anisotropic etching. First the microchannels were etched in silicon and then a Pyrex glass cover was anodically bonded to the microchannel plates. The microchannels are smooth with a maximum surface roughness of few micrometers. For every microchannel, the tests were conducted up to a pressure of 250-300 psi, as microchannel failure occurred at pressures greater than 250 psi. Therefore, this limited the Reynolds number range to only few hundreds for very small microchannels.

The uncertainties of measurements were analyzed and evaluated. The uncertainty of the differential pressure measurement was estimated to be less than $\pm 1\%$ for all the conditions tested. For the flow rate measurement, the error was less than $\pm 1.5\%$. The errors in the measurement of streaming potential was less than $\pm 15\%$ and in electrical conductivity was less than $\pm 2\%$. The resulting deviations of flow friction calculation was evaluated to be less than $\pm 9.5\%$, the Reynolds number was less than $\pm 6.5\%$ and the heat transfer coefficient was less than $\pm 10\%$.

8.12. Results and discussion

Experimental and theoretical investigation on fluid flow and heat transfer in microchannels of trapezoidal cross-section etched in silicon and bonded anodically to a Pyrex glass cover plate was carried out. The hydraulic diameters of the microchannels studied ranged from $51\ \mu\text{m}$ to $169\ \mu\text{m}$ and other characteristics dimensions are shown in Table 8.2. The pressure drop (ΔP) across the microchannel, flow rate (Q_{exp}), various electrokinetic parameters and temperatures were measured. Based on these measurements the flow characterizing parameters such as the experimental Reynolds number, Re_{exp} , experimental friction factor, f_{exp} , and friction constant, C_{exp} are calculated using the following relations:

$$\text{Re}_{\text{exp}} = \frac{\rho Q_{\text{exp}} d_h}{A_c \mu} \quad (8.42)$$

$$f_{\text{exp}} = \frac{2 A_c^2 \Delta P d_h}{Q_{\text{exp}}^2 \rho \mu} \quad (8.43)$$

$$C_{\text{exp}} = f_{\text{exp}} \text{Re}_{\text{exp}} \quad (8.44)$$

Table 8.2: Characteristics dimensions of the trapezoidal silicon microchannels

S. No.	Top Width μm	Bottom Width μm	Height μm	Hydraulic Diameter μm	H/W
1	403.20	364.80	25.60	47.30	0.066667
2	302.00	266.00	25.30	45.60	0.089085
3	307.20	259.20	40.00	69.01	0.141243
4	396.00	273.00	115.50	165.40	0.345291
5	127.20	79.20	40.00	55.10	0.387597
6	120.00	74.40	42.00	56.30	0.432099
7	242.40	120.00	115.50	134.20	0.637417
8	180.00	55.20	115.50	104.80	0.982143
Length of the microchannels = 2.8 cm and number of microchannels per plate = 4 ~ 5					

The heat transfer characteristics are mainly defined by heat transfer coefficient and Nusselt number, which are calculated using Equations (8.39) to (8.41). The experimental results are compared with the theoretical predictions. The theoretical values are calculated by solving the appropriate equations with the numerical scheme developed. The experimentally measured pressure drop, flow rate, liquid properties, temperatures and physical dimensions of the microchannels are used as the input parameters to solve these equations. Some other parameters such as theoretical Reynolds number, average velocity, friction factor and friction constant are calculated using the following relations:

$$U = \frac{1}{A_c} \int_{A_c} u(y, z) dA_c \quad (8.45)$$

$$Q_{thy} = UA_c \quad (8.46)$$

$$Re_{thy} = \frac{\rho U d_h}{\mu} \quad (8.47)$$

$$f_{thy} = \frac{2\Delta P d_h}{L \rho U^2} \quad (8.48)$$

$$C_{thy} = f_{thy} \text{Re}_{thy} \quad (8.49)$$

8.12.1. Flow rate pressure drop characteristics

(i): Experimental Data: For all trapezoidal silicon microchannels used in this study, Figure 8.4 show the experimentally measured pressure drop flow rate (Reynolds number) characteristics. The working fluid used was water with three different electrolyte concentration; De-ionized ultra filtered water (*DIUF*), $\text{Conc1} = 10^{-5} \text{M KCl}$ and $\text{Conc2} = 10^{-4} \text{M KCl}$. KCl ions were dissolved in water in appropriate proportions to make the different electrolyte concentrations. Figures 8.4a, 8.4b 8.4c and 8.4d, show the pressure drop flow rate characteristics for microchannels of $51.07\mu\text{m}$, $51.3\mu\text{m}$, $79.93\mu\text{m}$ and $114.5\mu\text{m}$ hydraulic diameters with different electrolyte concentrations. As can be seen from these figures, as the flow rate increases, the pressure drop also increases linearly, as required by laminar flow theory. The pressure drop is maximum for DIUF water, which has negligible ions present in it. As the concentration is increased to 10^{-5}M the pressure drop is slightly lower compared to DIUF water. The pressure drop reduces further when the concentration is increased to 10^{-4}M . This is due to the fact that when the concentration increases, the electrical double layer thickness decreases, or in other words, the double layer is squeezed. This results in reduced resistance to flow, which results in lower pressure requirement for high concentration solutions. As can be seen from the Figures 8.4a-4d, the difference in the pressure drop between DIUF, 10^{-5}M and 10^{-4}M solutions is very small. The characteristic curves fall just next to each other and the

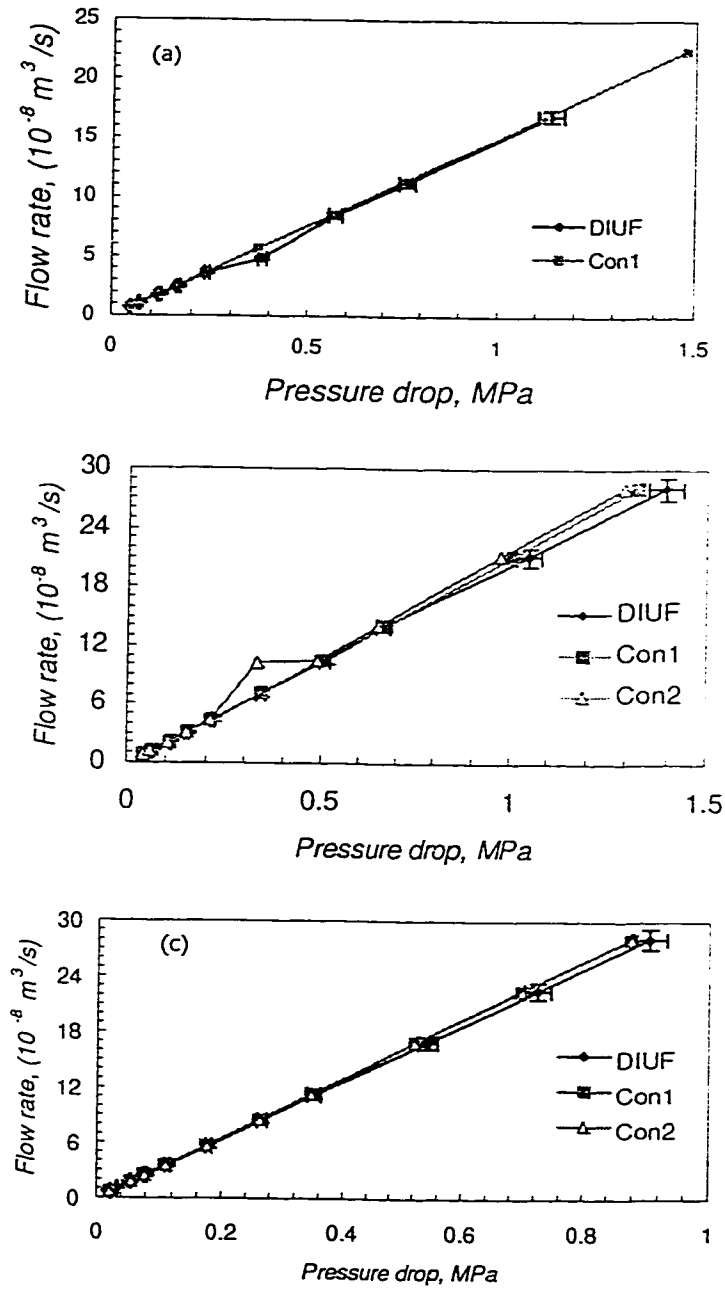


Figure 8.4abc: Pressure drop Vs flow rate characteristics for (a) 51.07 μm , (b) 51.3 μm , and (c) 79.93 μm trapezoidal silicon microchannels for DIUF water, 10^{-5} M and 10^{-4} M KCl electrolyte concentrations

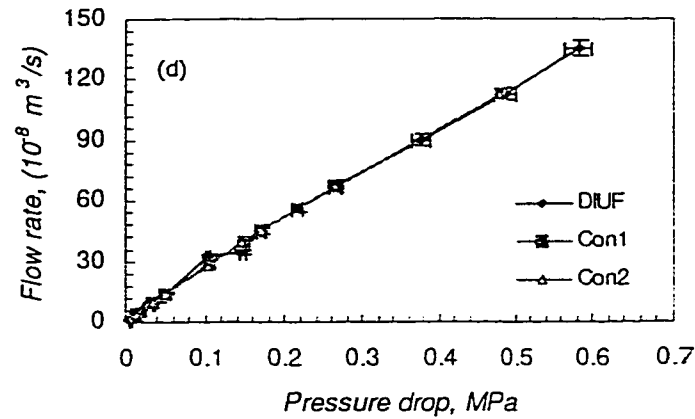


Figure 8.4d: Experimentally measured pressure drop Vs flow rate characteristics for 114.5 μm hydraulic diameter trapezoidal silicon microchannels for *DIUF* water, 10^{-5} M and 10^{-4} M KCl electrolyte concentrations

difference is less than 2-5%

.(ii): Comparison with conventional theory with electrokinetic effects: A comparison of the experimental data with theoretical predictions for flow of water with different electrolyte concentrations for a 51.3 μm d_h trapezoidal silicon microchannel is shown in Figures 8.4e-8.4g, for *DIUF*, Concl and Conc2, respectively. The theoretical predictions are calculated by solving the previously derived equations with a known value of zeta potential using finite difference. The zeta potential was calculated by using the measured value of the streaming potential and physical dimensions of the microchannel. Zeta potential values of 200 mV to 50 mV were obtained for various values of electrolyte concentrations with silicon and Pyrex glass materials. The measured zeta potential values were verified by conducting a series of experiments with 30 to 400 μm deep parallel plate microchannels made of silicon and Pyrex glass. The surface conductivity effects were

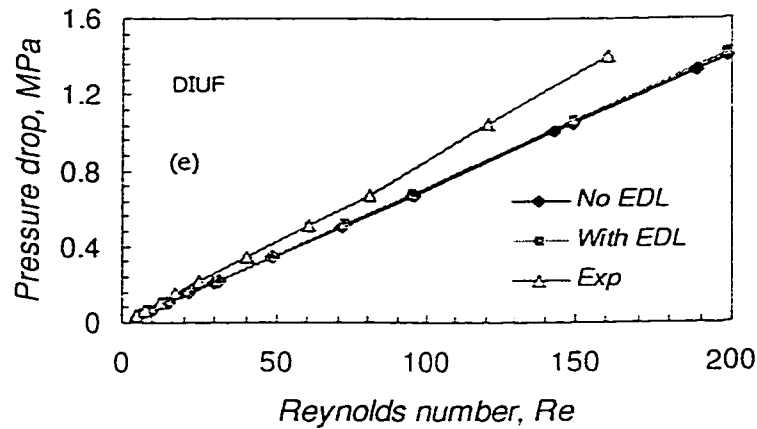


Figure 8.4e: Comparison of the theoretically predicted pressure drop with experimentally measured pressure drop for 51.3 μm hydraulic diameter trapezoidal silicon microchannel for *DIUF* water.

considered in the zeta potential calculations. The values of zeta potential used for different concentrations for silicon and Pyrex glass are *DIUF*; 200 mV and 100 mV, *Conc1*; 150 mV and 75 mV and *Conc2*; 100 mV and 50 mV, respectively. As can be seen from the Figures 8.4e-8.4g, the electrokinetic effect is negligible and does not account for the higher experimental pressure drop. Besides as can be observed from the Figures 8.4e-8.4g, the difference in the pressure drop for these solutions falls within the repeatability range of the experimental data. Therefore, from these observations it can be concluded that the electrokinetic effects at the solid liquid interface are present, but the magnitude of the effects is very small. Therefore, for microchannels with hydraulic diameters greater than 50 μm , the electrical double layer effect can safely be neglected. This implies that the electrokinetic effects are significant for small microchannels and negligible for larger

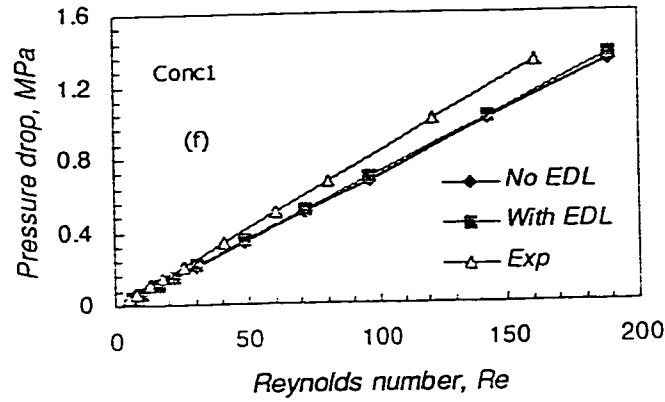


Figure 8.4f: Comparison of the theoretically predicted pressure drop with experimentally measured pressure drop for 51.3 μm hydraulic diameter trapezoidal silicon microchannel for $10^{-5} M$ KCl water.

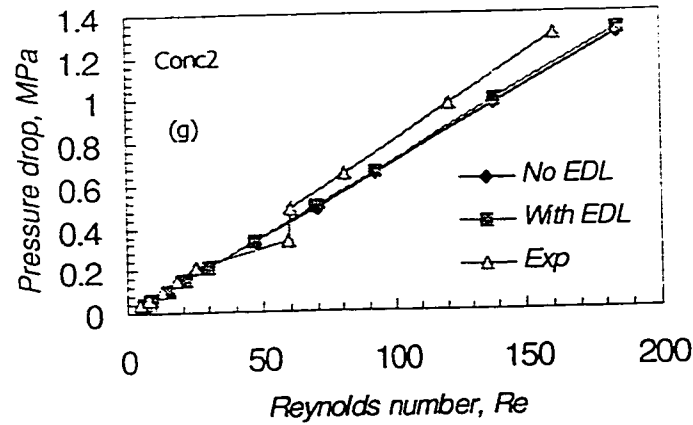


Figure 8.4g: Comparison of the theoretically predicted pressure drop with experimentally measured pressure drop for 51.3 μm hydraulic diameter trapezoidal silicon microchannel for $10^{-4} M$ KCl water

microchannels. This conclusion is in accordance with Hunter (1981), Mala, et al (1997, 1996), and Yang and Li (1998).

(iii) Comparison with conventional theory with no electrokinetic effects: For all the microchannels used in this study the pressure gradient ($\Delta P/L$) across the microchannels of various hydraulic diameters (calculated based on pressure drop through 28 mm long microchannels) is shown in Figures 8.4h-8.4i as a function of Reynolds number. The theoretical pressure drop is calculated from the conventional theory with no electrokinetic effects i.e. $\xi=0$, and compared with the experimentally measured pressure gradient. It can be seen that pressure gradient increases linearly as the Reynolds number increases, as suggested by the laminar flow theory. For small Reynolds numbers, there is a reasonable agreement between the experimental results and theoretical predictions, while for higher Reynolds numbers, the difference in the measured pressure gradient and the theoretical prediction is significant. The difference increases with an increase in the Reynolds number. For microchannels with small d_h , the relationship for the higher Reynolds numbers could not be obtained as the pressure inside the microchannels was greater than the strength of the anodic bond between the Pyrex and silicon. It was observed that at pressures greater than 250 psi, the microchannel plates developed small cracks which resulted in breakage of the plates. However, even for small Reynolds numbers the slope of the measured curves is higher than the theoretical curves; it would be reasonable to expect the slope will increase further for higher Reynolds numbers. For higher d_h microchannels, Reynolds numbers above 2000 could be reached easily. For such microchannels, the slope of the measured curves is still higher than the theoretical

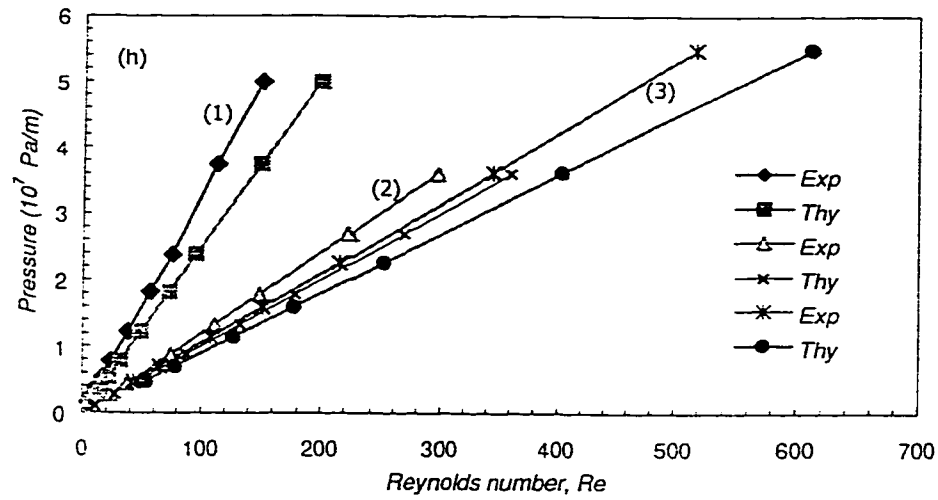


Figure 8.4h: Comparison of the experimentally measured pressure gradient with theoretical prediction for (1) 51.3 μm , (2) 62.3 μm , and (3) 64.9 μm hydraulic diameter trapezoidal silicon microchannels for DIUF water.

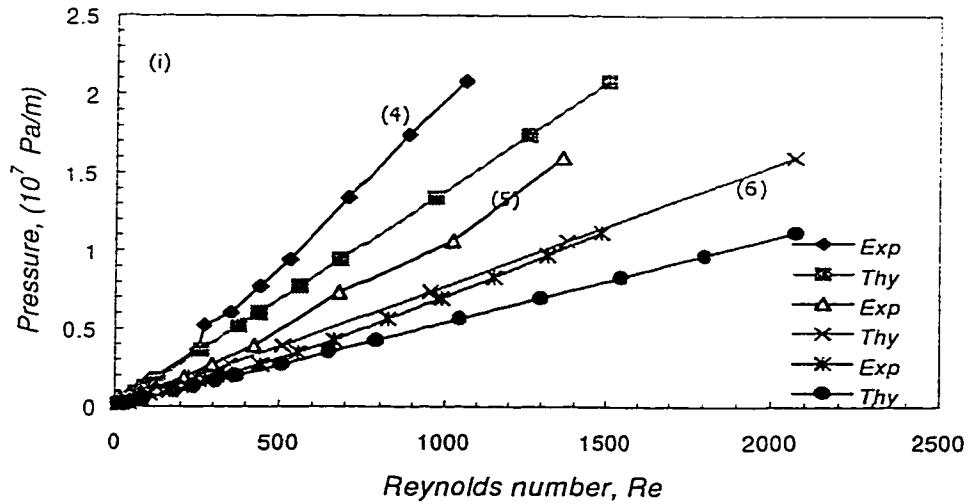


Figure 8.4i: Comparison of the experimentally measured pressure gradient with theoretical prediction for (4) 114.5 μm , (5) 142 μm , and (6) 168.9 μm hydraulic diameter trapezoidal silicon microchannels for DIUF water.

curves, but the difference is small compared to small d_h microchannels. The results are in accordance with the results reported in literature.

8.12.2. Friction characteristics

The flow behavior of water through microchannels can also be interpreted in terms of the flow friction. The experimental friction factor, f_{exp} can be determined by Eq.(8.43). In Figure 8.5a, the friction factor is plotted as a function of the experimentally determined Reynolds number. For comparison, the relationships between the friction factor and Reynolds number as predicted by the conventional theory is also plotted. From the figure, it is observed that in the high Reynolds number range, the experimental values are higher than the theoretical predictions. This implies that at a given Reynolds number or flow rate, the friction in microchannels is higher than calculated from conventional theory predictions.

In addition to the friction factor, another important parameter used in flow characterization is friction constant, Equation (8.44). The value of the friction constant remains constant for a flow regime, as predicted by the conventional theory. For trapezoidal microchannels, the friction constant is dependent only on the geometry of the microchannel cross-section, Shah and London (1978). Thus, a constant value of the friction constant should be expected as per the theory. However, according to the experimental data acquired during this study, C_{exp} is not a constant but varies as a function of the Reynolds number. To better illustrate the difference between the theoretical and the experimental value, the friction constant ratio is introduced. The friction constant ratio is defined as

$$C^* = \frac{C_{exp}}{C_{thy}} = \frac{f_{exp} Re_{exp}}{f_{thy} Re_{thy}} \quad (8.50)$$

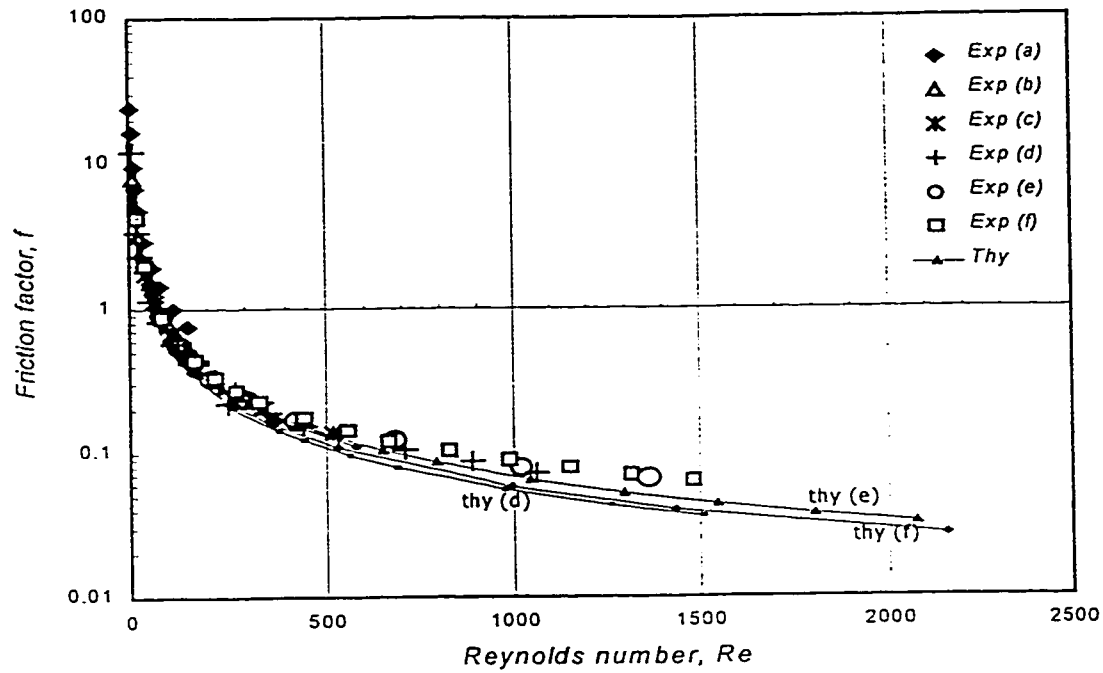


Figure 8.5a: A comparison of the experimental and theoretical predictions of friction factor for (a) 51.3 μm , (b) 62.3 μm , (c) 64.9 μm , (d) 114.5 μm , (e) 142 μm , and (f) 168.9 μm , hydraulic diameter trapezoidal silicon microchannels for DIUF water.

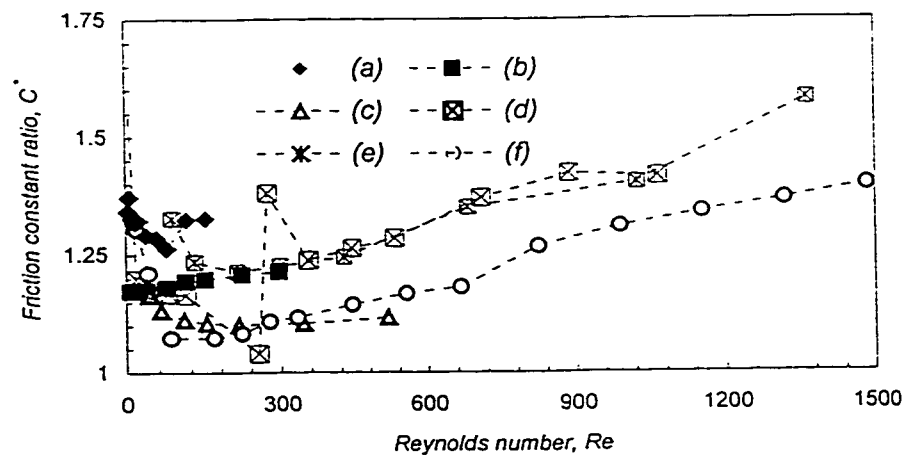


Figure 8.5b: Friction constant ratio Vs Reynolds number for (a) 51.3 μm , (b) 62.3 μm , (c) 64.9 μm , (d) 114.5 μm , (e) 142 μm , and (f) 168.9 μm , hydraulic diameter trapezoidal silicon microchannels for DIUF water.

For the case of $Re_{exp} = Re_{thy}$, the friction constant ratio reduces to the ratio of friction factors at that Reynolds number. The behavior of C^* as a function of the Reynolds number is shown in Figure 8.5b. As the experimental friction factor is greater than one, the value of C^* is always greater than one. As can be seen from the figure, the value of C^* is higher for very small Reynolds numbers. But as the Reynolds number increases, the C^* ratio decreases. With a further increase in the Reynolds number, the ratio increases and becomes approximately 1.5, which implies a 50% increase in the friction factor compared to conventional theoretical prediction. Therefore, it can be concluded that the experimental friction factor is higher than the theoretical friction factors for trapezoidal silicon microchannels.

8.12.3. *Roughness viscosity model*

The above-discussed characteristics of higher flow friction have to do with the scale of microchannels. We measured the surface roughness of the microchannels. The surface roughness of the Pyrex glass was measured by Profilometer and was found to be of the order of 10nm. The surface roughness of silicon microchannels was measured by using a high resolution inverted research metallurgical microscope (Olympus, Model PMG3). It was found that the average roughness height k varies from 0.8 μm for smaller microchannels to 2.0 μm for larger microchannels as shown in Table 8.2. The roughness with such an order of magnitude can safely be neglected for microchannels with diameters of the order of millimeters. However, for microchannels used in this study, the ratio of $2k/d_h$ ranges from 2.4 to 3.5%. The channel height is the smallest dimension for these trapezoidal microchannels. Therefore, the effects of surface roughness on flow velocity and friction should be investigated.

Generally the presence of the surface roughness affects the laminar velocity profile and decreases the transitional Reynolds number. This has been shown by a number of experiments and discussed in detail in Chapter 5. The roughness viscosity model has been developed in Chapter 5 for laminar flow in microtubes. As discussed previously, the surface roughness increases the momentum transfer in the boundary layer near the wall. This additional momentum transfer can be accounted for by introducing the roughness viscosity μ_R in a manner similar to the eddy viscosity concept in the turbulent flow model. The mathematical treatment developed in Chapter 5 was developed for cylindrical geometry, whereas the cross-section of the microchannels discussed here is trapezoidal. Therefore, the model is further developed for flow in trapezoidal microchannels.

According to the concept of roughness viscosity, μ_R should have a higher value near the wall and gradually diminish as the distance from the wall increases. Besides, μ_R should also increase as Re increases. The ratio of the roughness-viscosity to the fluid viscosity in trapezoidal microchannels is proposed to take the form:

$$\frac{\mu_R}{\mu} = A Re_k \frac{(R_h - l_{\min})}{k} \left(1 - \exp \left(- \frac{Re_k (R_h - l_{\min})}{Re k} \right) \right)^2 \quad (8.51)$$

Where, A is the coefficient that is to be determined by the experimental data; R_h is defined as the hydraulic radius of the microchannel; l_{\min} is the shortest distance from the point to the microchannel wall; Re_k denotes the local roughness Reynolds number, and is defines as

$$Re_k = \frac{U_k \rho_f k}{\mu} \quad (8.52)$$

Where U_k denotes the velocity at the top of the roughness element and is given by

$$U_k = \left(\frac{\partial u}{\partial n} \right)_\tau k \quad (8.53)$$

By introducing the roughness-viscosity in the equation of motion in a manner similar to the eddy viscosity in the turbulent flow, the equation of motion in the laminar flow through a trapezoidal microchannel becomes;

$$\frac{\partial^2 u}{\partial y^2} + \frac{\partial^2 u}{\partial z^2} = \frac{1}{(\mu + \mu_R)} \frac{dP}{dx} \quad (8.54)$$

with no slip boundary conditions on the wall of the microchannel.

$$U(y,z)=0 \text{ on } \tau \quad (8.55)$$

Equation 8.54 is the modified equation of motion that accounts for the effects of surface roughness on a laminar flow. Comparing Equation (8.54) with the Equation (8.11) for $F_I=0$, it is apparent that once the roughness viscosity is know, the modified equation of motion can be solved similarly by the method as developed in the previous sections.

As seen from the roughness-viscosity function, Equation (8.51), all parameters except the coefficient A can be determined from the flow field, the dimensions and the average surface roughness of the microchannel. Basically, the coefficient A not only depends on the factors mentioned above, but also depends on the shape and the distribution of the roughness elements. In principle the value of A should vary from channel to channel. However, based on the experimental data, an empirical relation is used to calculate A, which is discussed in detail in Chapter 5. For the trapezoidal microchannels, the coefficient A can be evaluated by

$$A = 5.8 \left(\frac{R_h}{k} \right)^{0.35} \exp \left(\text{Re}^{0.94} \left(5 \times 10^{-5} \frac{R_h}{k} - 0.0031 \right) \right) \quad (8.56)$$

Figures 8.6a and 8.6b show the comparison of the measured $P_x \sim Re$ relationships with the predictions of the roughness viscosity model. As can be seen from the Figures 8.6a and 8.6b, the curves predicted by the surface roughness viscosity model and the experimental curves are in an excellent agreement with each other. This implies that the roughness viscosity model proposed in the present section may be used to interpret the flow characteristics in these microchannels.

8.12.4. Heat transfer characteristics

The heat transfer characteristics in trapezoidal silicon microchannels with de-ionized ultra filtered water (*DIUF*) as the working fluid were investigated. The microchannel plate was heated by a micro-heater placed underneath. A heatsink paste thin film was placed between the heater and the microchannel plate to obtain proper contacts between the heater and the microchannel plate. Two thermocouples were placed at inlet and outlet of the microchannel to measure the inlet and outlet liquid temperatures. Three thermocouples were placed on the microchannel plate surface (in contact with the micro-heater) to measure the microchannel plate wall temperatures at inlet, middle and outlet positions. The wall temperature is assumed to be equal to the surface temperature at the channel walls, as the thermal resistance offered by the silicon plate is negligible. For example, after etching 100 μm deep microchannels on a 0.5 mm thick, 2.8 cm² cross-sectional area silicon plate, the thermal resistance offered varies from 0.0004 to 0.001 °C/W. The change in the thermal resistance is due to change in the thermal conductivity of intrinsic silicon with temperature. As is shown in Chapter 7, the thermal conductivity of silicon is maximum at room temperature and decreases with increase in temperature thereby increasing the thermal resistance offered by the silicon microchannel plate. Even

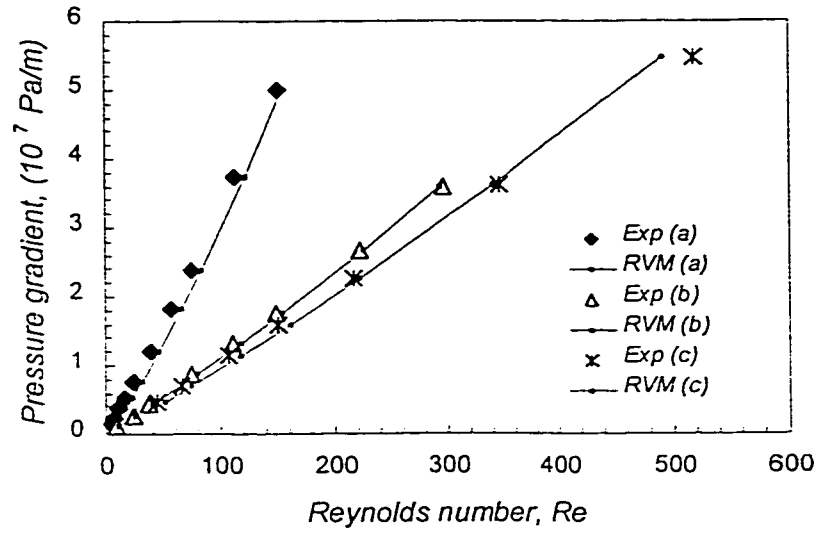


Figure 8.6a: A comparison of the experimental pressure gradient Vs Reynolds number with the theoretical predictions of roughness viscosity model for (a) 51.3 μm , (b) 62.3 μm , (c) 64.9 μm hydraulic diameter trapezoidal silicon microchannels for DIUF water.

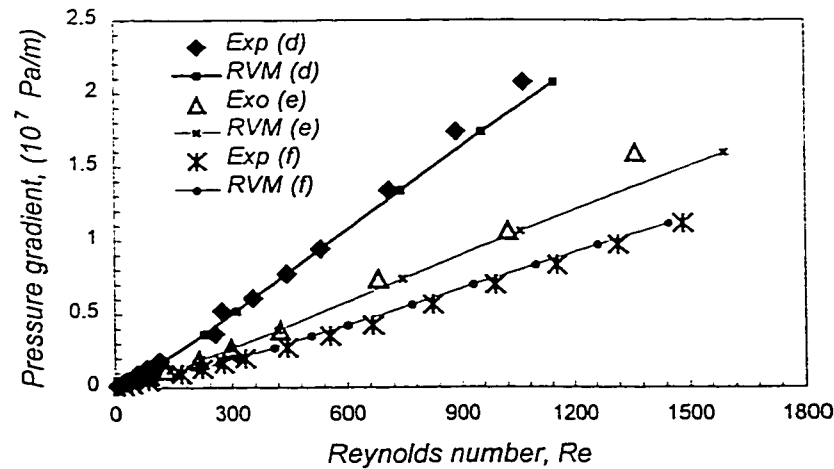


Figure 8.6b: A comparison of the experimental pressure gradient Vs Reynolds number with the theoretical predictions of roughness viscosity model for (d) 114.5 μm , (e) 142 μm , and (f) 168.9 μm hydraulic diameter trapezoidal silicon microchannels for DIUF water.

at higher wall temperatures the thermal resistance is still negligible. The experiments were conducted for various flow rates at different surface temperatures of up to 75 °C.

The heat transfer characteristics for liquid flow in trapezoidal silicon microchannels are shown in Figure 8.7. Figures 8.7a to 8.7d show the Nusselt number Vs Reynolds number for microchannels of 62.3 µm, 63.1 µm, 114.5 µm and 168.9 µm hydraulic diameters, respectively. The experimental results are compared with the conventional theoretical predictions, roughness-viscosity-model and results of Peng et al (1994b). For fluid flow in conventionally sized channels, the forced convective heat transfer in laminar flow regime can usually be predicted by the relationship, Shah and London (1978):

$$Nu = 1.86 \left(\frac{d_h}{L} \right)^{1/3} (Re Pr)^{1/3} \left(\frac{\mu}{\mu_w} \right)^{0.14} \quad (8.57)$$

This conventional empirical relation is valid for constant surface temperature which is the case prevailing in our experiment also. As discussed earlier, the source of heat supply is a micro-heater with one side insulated and other in contact with the microchannel plate through a heat sink compound thin film. A constant power (low voltage high current) is supplied to the heater. Some of the heat generated by the heater is lost through the insulation and the remainder is conducted to the microchannel plate through the thermal conducting and electrically non-conducting heat sink compound thin film. Assuming, that the heat is conducted uniformly, a constant surface temperature (wall temperature) at the interface can be measured. The wall temperatures of up to 75 °C were measured by the three thermocouples.

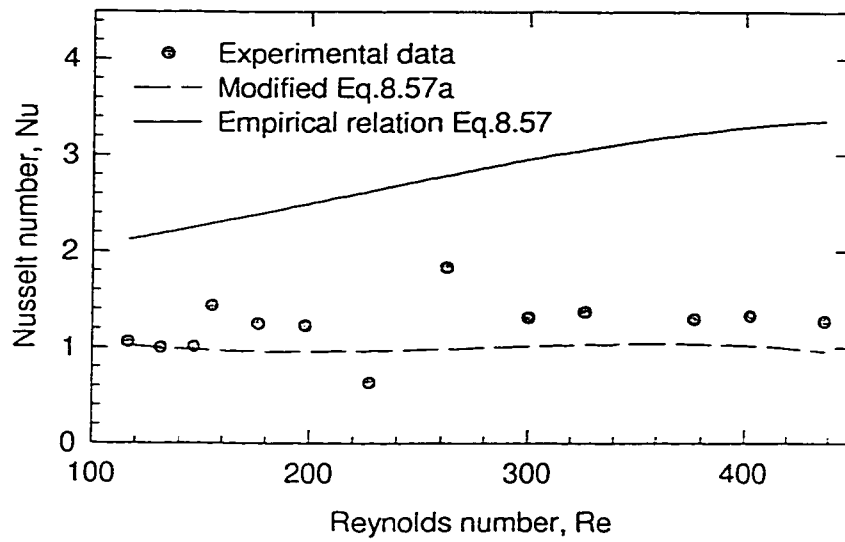


Figure 8.7a: Nusselt number vs Re for a 62.3 μm trapezoidal silicon microchannel and comparison of the experimental results with conventional theory and RVM

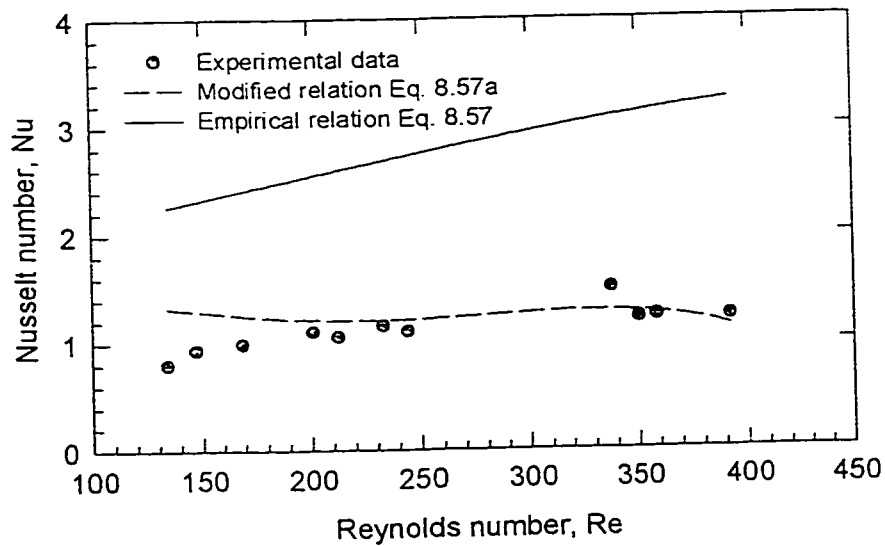


Figure 8.7b: Nusselt number vs Re for a 63.1 mm trapezoidal silicon microchannel and comparison of the experimental results with conventional theory and RVM

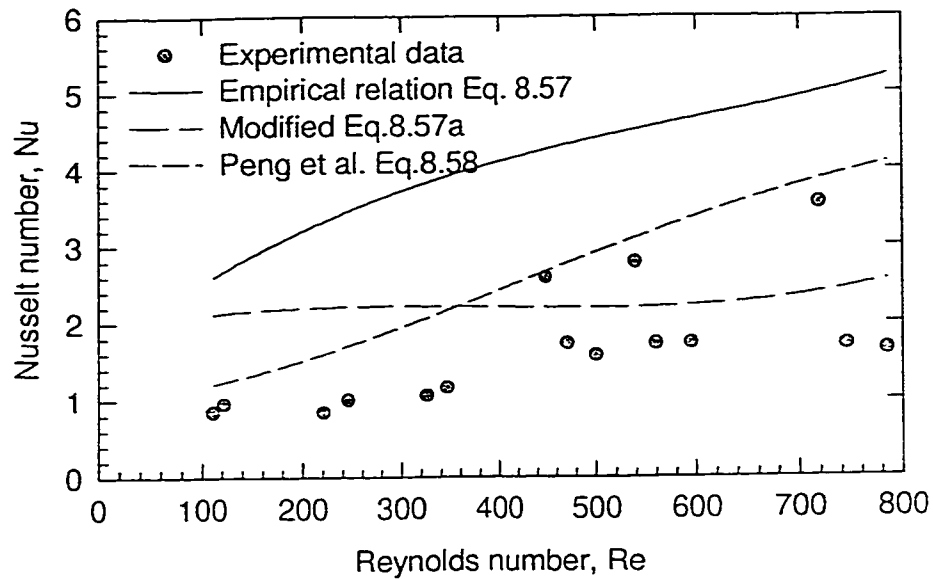


Figure 8.7c: Nusselt number vs Re for a 114.5 μm trapezoidal silicon microchannel and comparison of the experimental results with conventional theory, Peng et al. and RVM

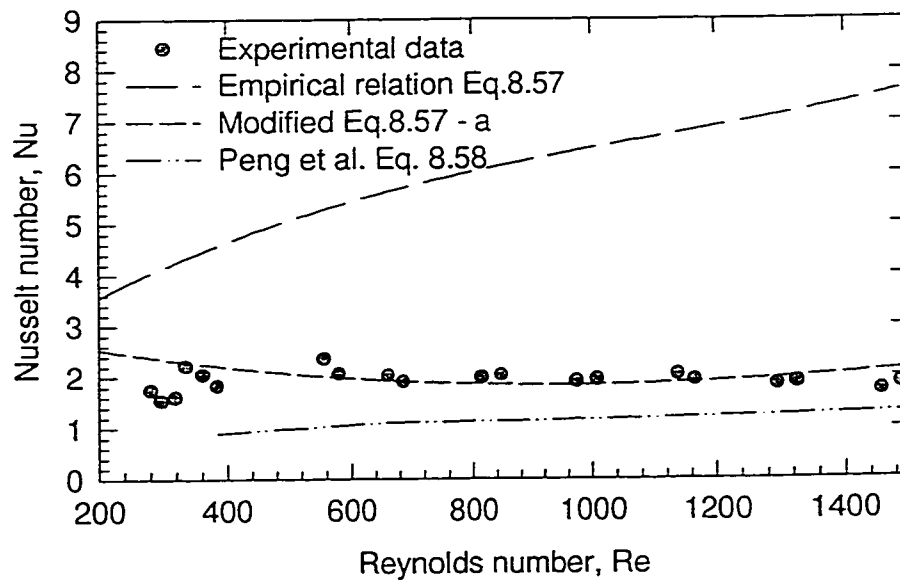


Figure 8.7d: Nusselt number vs Re for a 168.9 μm trapezoidal silicon microchannel and comparison of the experimental results with conventional theory, Peng et al. and RVM

As can be seen from the Figures 8.7a to 8.7d, the measured results are lower than the theoretical predictions of Equation (8.57). For small Reynolds numbers the difference between the measured results and the theoretical predictions is small compared to higher Reynolds numbers. This is in part due to the surface roughness effects as the microchannels used in this investigation have a high distributed-surface roughness to diameter ratio compared to conventional sized channels. The effect of this surface roughness in laminar flow regime is considered by the roughness viscosity model as developed previously, section 8.12.3. The surface roughness viscosity has a maximum value at the wall and approaches to zero far away from the wall. Once the microchannel size and the pressure drop are known, the roughness viscosity in the flow field can be easily calculated as a function of the Reynolds number. Equations (8.51) to (8.56). The effect of the surface roughness viscosity in laminar flow on heat transfer characteristics in microchannels can be determined by appropriate modifications to the conventional theory relationship, Equation (8.57). Once the average value of the roughness viscosity is calculated, the total wall effects can be accounted for by the addition of average roughness viscosity to the dynamic viscosity at wall temperature, μ_w . The overall result from such a modification would be a reduced Nusselt number as compared to the theoretical prediction. The modified empirical relationship that fits the experimental data appropriately is given as:

$$Nu = 1.86 \left(\frac{d_h}{L} \right)^{1/3} (Re Pr)^{1/3} \left(\frac{\mu}{\mu_w + \mu_{Rwm}} \right)^n \quad (8.57a)$$

where $n = 10^4 d_h$. As can be seen from Figures 8.7a to 8.7d, the predictions of this modified empirical relation agree very well with the experimental data.

Peng et al. (1994b) also investigated characteristics of water flowing through rectangular microchannels experimentally. Based on their results, they proposed a relation to correlate the data for laminar flow in microchannels, given as:

$$Nu = C_{H,l} Re^{0.62} Pr^{1/3} \quad (8.58)$$

Where $C_{H,l}$ is an empirical coefficient which strongly depends the aspect ratio, H/W , of the microchannels. The aspect ratios, H/W , of microchannels with hydraulic diameters of 114.5 μm and 168.9 μm are close to those of the microchannels used by Peng et al (1994b). Therefore, for the purpose of comparison the experimental results are compared with the predictions of Equations (8.58) as shown in Figures 8.7c and 8.7d. It is observed that the current experimental results are relatively close to Peng et al. ((1994b) results and follow a similar trend. Besides it should be noted that the microchannels used by Peng et al are machined on a stainless steel plate that also is used as the supply heat source. As is well known from conventional theory, the Nusselt number is higher for the constant heat flux at the surface of the channel than the constant surface temperature case. The experimental results of Peng et al. (1994b) are also much smaller than the conventional theory predictions.

8.13. Summary

Fluid flow and heat transfer in trapezoidal silicon microchannels were investigated both theoretically and experimentally. The interfacial effects such as the effects of electrical double layer at the solid liquid interface were also considered. The results were compared with conventional theory. It was found that for microchannels the experimentally measured pressure drop was higher than the theoretical prediction. Nevertheless, for microchannels greater than 100 μm hydraulic diameter, the difference

becomes small and for small Reynolds numbers the experimental data agrees well with the theoretical predictions. The experimentally measured friction factors and friction constants were also higher than the theoretical value. For small silicon microchannels, the roughness surface roughness is small and for higher / deep microchannels the surface roughness is of the order of few micrometers. This distributed surface roughness has a significant effect on the flow characteristics. The effects of this surface roughness are predicted by the roughness viscosity model. A good agreement between the experimental and theoretical predictions can be found. For the case of heat transfer, heat transfer coefficients up to 20,000 W/m²K were obtained. For 2.8 cm long microchannels, a temperature difference of up to 35 °C between the microchannel coolant outlet and inlet was measured. This large increase in the coolant temperature significantly changes the thermophysical properties of the coolant. Variable properties were used to calculate all the heat transfer characteristics. A comparison of the results indicates that although very high heat transfer coefficients were measured, the results are slightly lower than the theoretical prediction but match reasonably well with the results reported in the literature.

8.14. References

1. Anderson, J.L. and Quinn, J.A., 1972, ' Ionic mobility in microcapillaries', *Faraday Transactions, I*, vol. 68, pp.744-748.
2. Chan, D.Y.C. and Horn R.G., 1985, 'Drainage of thin liquid film', *J. Chem. Phys.*, Vol. 83, no. 3, pp. 5311-5324.
3. Choi S.B., Barren R.R., and Warrington R.O., (1991), 'Fluid Flow and Heat Transfer in Micro Tubes', *ASME DSC* vol. 40, pp. 89-93.
4. Debye, P. and Cleland, R.L., 1959, 'Flow of liquid hydrocarbons in porous vycor', *J. Appl. Phys.*, vol. 30, no. 6, pp. 843-849.
5. Eringen, A., 1964, 'Simple microfluids', *Int. J. Eng. Sci.*, vol. 2, pp.205-217.

6. Gee, M.L., Mcguiggan, P.M., Israelachvili, J.N. and Homola, A.M., 1990, 'Liquid to solidlike of molecularly thin films under shear', *J. Chem. Phys.*, Vol. 93, no. 3, pp. 1895-1906
7. Harley, J., and Bau, H., 1989, 'Fluid flow in micron and submicron size channels', *IEEE Trans.*, vol. THO249-3, pp. 25-28.
8. Hunter, R. J., 1981, *Zeta potential in colloid science, principles and applications*, Academic Press, New York.
9. Kays, W.M. and Crawford, M.E., 1980, 'Convective heat and mass transfer' Second Edition, McGraw-Hill, N.Y. p-393.
10. Mala, G. M., Li, D., 1998, 'Flow characteristics of water in microtubes', *International Journal of Heat and Fluid Flow*, (Accepted for publication).
11. Mala G. M., Yang, C., and Li, D., 1998, 'Electrical double layer potential distribution in a rectangular microchannel', *Colloids and Surfaces: A*, vol. 135 Nos. 1-3, pp.109-116.
12. Mala, G. M., Li, D., Werner, C., Jacobasch, H.J., and Ning Y., 1997, 'Flow characteristics of water through a microchannel between two parallel plates with electrokinetic effects', *Int. J. Heat and Fluid Flow*, vol. 18, pp. 489-496.
13. Mala, G. M., Li, D. and Dale J. D., 1996, 'Heat transfer and fluid flow in microchannels', *Int. J. Heat Mass Transfer*, vol. 40, No. 13, pp. 3079-3088.
14. Peng, X.F., Peterson, G.P., Wang, B.X., 1994a, 'Frictional flow characteristics of water flowing through rectangular microchannels', *Experimental heat transfer*, vol. 7, pp. 249-264.
15. Peng, X.F., Peterson, G.P., Wang, B.X., 1994b, 'Heat transfer characteristics of water flowing through microchannels', *Experimental heat transfer*, vol. 7, 265-283.
16. Pfahler, J.N., 1992, 'Liquid transport in micron and submicron size channels', *Ph.D. Thesis*, Department of Mechanical Engineering and Applied Mechanics, University of Pennsylvania, USA.
17. Philips, R.J., 1990, 'Microchannel Heat Sinks', In *Advances in Thermal Modeling of Electronic Components and Systems* (Edited by A. Bar-Cohen and A.D. Kraus), Vol. II Chap. 3. ASME Press New York.
18. Shah, R. K., and London, A. L., 1978, 'Laminar flow forced convection in ducts: A source book for compact heat exchanger analytical data, Supl. 1', Academic Press, N.Y., p.-259

19. Tuckerman, D.B., 1984 'Heat transfer microstructures for integrated cooling', *Ph.D. Thesis*, Stanford University, Stanford, CA.
20. Wang, B.X. and Peng, X.F., 1994, 'Experimental Investigation on Liquid Forced Convection Heat Transfer Through Microchannels', *Int. J. Heat Mass Transfer*, vol. 37 (Suppl.1), pp. 73-82.
21. Wu, P. Y., and Little, W. A., 1983, 'Measurement of friction factor for flow of gases in very fine channels used for microminiature Joule-Thompson refrigerators', *Cryogenics*, vol. 24, No. 8, pp.273-277.
22. Yang, C., and Li, D., 1997, 'Electrokinetic effects on pressure-driven liquid flows in rectangular microchannels', *J. of Colloid and Interface Sciences*, vol. 194, pp. 95-107.

Chapter 9 Concluding Remarks

9.1. Contributions of this work

The main aim of this work was to investigate fluid flow and heat transfer in microchannels, and develop fundamental understanding of flow and heat transfer characteristics. Because of the published results about microscale fluid flow that are conflicting, more emphasis was laid on the fluid flow part. An attempt was made to seek answers to the questions being asked about microscale fluid flow and heat transfer characteristics, as discussed previously in this dissertation. The answers to these questions are the main contributions of this work and are discussed below:

- It was found that the differences between the experimental observations and the conventional theory predictions are in part due to the interfacial effects that are neglected in conventional theory. These effects are, surface roughness and electrokinetic phenomena such as the effects of electrical double layer at the solid-liquid interface.
- Mathematical models were developed to incorporate the effects of these phenomena. Appropriate corrections are made to the conventional theory by incorporating these extra terms in the system of governing equations. It can be seen that the predicted results agree very well with the experimental observations.
- For flow and heat transfer in parallel plate microchannels, the electrokinetic transport model developed explains the differences and suggests corrections that should be made to the conventional theory.

- For cylindrical microchannels of stainless steel and fused silica, the experimentally measured pressure gradient was significantly higher than theoretical predictions. This higher pressure difference is explained by incorporating the roughness effects at the wall of the microchannel. A mathematical model 'Roughness Viscosity Model' was developed that explains the observed higher pressure requirement. The effects of surface roughness on fluid flow in laminar range can be accounted for by this model. The predicted results agree very well with the experimental results. However, the electrokinetic effects in fused silica microtubes used in this study are negligible and were not considered.
- An experimental apparatus was designed and developed to investigate fluid flow and heat transfer characteristics of water in microchannels with interfacial effects. Equipped with the state of the art equipment and fully computer controlled, this setup can be used to pursue further research in this field or any other related fields.
- For flow in trapezoidal silicon microchannels, the experimental pressure drop across a microchannel is much higher than predicted by conventional theory. Therefore, the apparent viscosity of water is higher than the bulk viscosity. This apparent viscosity decreases with an increase in the electrolyte concentration. However, as observed from the experimental data, the interfacial effects are present but are negligible for microchannels with hydraulic diameters greater than 50 μm . However, as the hydraulic diameters of the microchannels decreases, the difference between the experimental results and theoretical predictions increases while as for microchannels with hydraulic diameters greater than 100 μm , there is a reasonably good agreement between the experimental data and theoretical predictions.

- This higher apparent viscosity can be explained if the effects of distributed surface roughness at the microchannel walls is considered. It was found that the average height of the surface roughness element increase as the depth of the etch increases. For etch depths of less than 80 μm , the average height of the roughness element is less than 1 μm , whereas for etch depths greater than 80 μm , the average height is about 2 μm . A mathematical model developed to incorporate the effects of this surface roughness predicts results that are in very good agreement with the experimental data. Therefore, it is very important not to neglect the effects of surface roughness in laminar flow.
- The temperature increase in the coolant from inlet to outlet of the microchannel is much higher than expected in macroscale channels. Consequently the thermophysical properties of the coolant change appreciably. Therefore, the effect of variable properties should be considered in heat transfer characteristics. The heat transfer results are lower than as predicted by the conventional thermophysical correlations, but are at par with published results on microchannel heat transfer in literature, and agree well with the predicted results by incorporating the effects of surface roughness.

9.2 Future work

Because of the time and program constraints, flow in very small microchannels could not be investigated up to critical Reynolds number. To study flow and heat transfer up to critical Reynolds number in these small microchannels, the microchannel chip should be reinforced to avoid breaking at pressures greater than 250 psi. More tests should be conducted to investigate the electrokinetic effects in trapezoidal silicon

microchannels. In fact, the number of microchannels on the chip could be increased to minimize pressure ranges. The effects of H/W ratio should also be thoroughly investigated. The effects of distributed surface roughness could be further investigated following the mathematical models developed in this work.

Appendix I Equipment specification and calibration

AI.1 Calibration curve for the valdyne pressure transducer

The calibration of the sensor was performed with a dead weight tester with known weights and the output was noted. The process was repeated number of times and in both

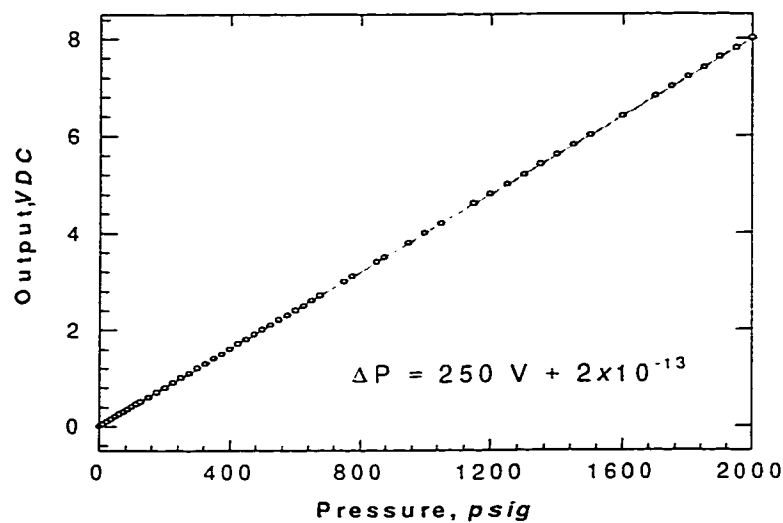


Figure: Calibration curve for valdyne pressure transducer

the directions. The calibration curve is given:

AI.2 Features of the transducer

- High Sensitivity to Low Pressures
- Ranges as Low as 0.1 In H₂O Full Scale
- Changeable Sensing Diaphragms
- Rugged Construction
- Gas or Liquid Media

- Fast Dynamic Response

AI.3 Specifications of the high pressure precision pump

Some of the important specifications of the high pressure Ruska proportioning pump are:

- Number of cylinders 2
- Volume per cylinder 500 cc
- Maximum pressure 4000 psi
- Drive motor ½ HP 1800 rpm synchronous motor
- Number of feed rates 28
- Range of flow rates 2 to 560cc/hr
- Flow rate scale precision 0.02 cc

AI.4 Specifications of the low pressure tubing pump

Some of the important specifications of the low pressure-tubing pump are:

- Computer control drive, Model 7550-60
- Local remote operation
- Operating speeds of 60 to 600 rpm
- Flow rate for LS 16 tubing 4.8 to 480 ml/min @600 rpm
- 0.48 to 48 ml/min @60 rpm
- Com port control
- Different pump heads can be attached to the drive
- Different tubing options, classified as per pressure and flow rate rating

AI.5 Calibration of flow sensor

The flow sensor was calibrated by measuring the output voltage from the sensor corresponding to a known volume flow rate. The calibration was compared with the

manufacturers values and with high-precision pump flow rates, and a negligible difference was found. The calibration curve is given:

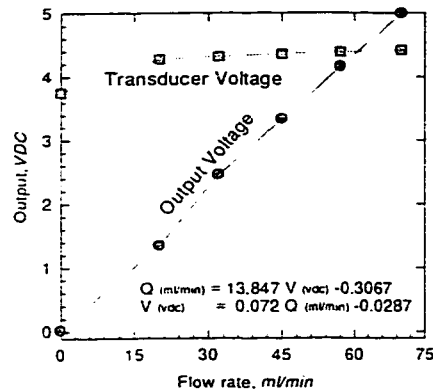


Figure: Calibration curve for flow sensor

AI.6 Specifications of the flow sensor

The most important specifications of the flow sensor are:

- Linear flow range 20-70 CC/min
- Total Accuracy $\pm 10\%$
- Repeatability $\pm 3\%$ full scale
- Linearity $\pm 4\%$ full scale
- Operating Temp range 32 to 180°F
- Voltage / current (12-18) $\pm 10\%$ VDC, and 20 mA maximum
- Analog 0-5 VDC

AI.7 Specifications of Keithley 6517A electrometer:

The model 6517A is a 6 ½-digit electrometer/high resistance system with the following measurement capabilities:

- DC voltage measurement from 10 μ V to 210 V
- DC current measurement from 100 aA to 21 mA
- Charge measurement from 10 fC to 2.1 μ C
- Resistance measurement from 10 Ω to 210 T Ω
- Surface resistivity measurement
- Volume resistivity measurement
- Temperature measurement
- Relative humidity measurement
- Remote operation using IEEE-488 GPIB bus
- Filtering; averaging and median
- Data storage
- Built in test sequence

AI.8 Specifications of InPro 7001/120 conductivity sensor

Some of the most important specifications of the conductivity sensor are:

- Electrodes and body AISI 31 6L
- Maximum pressure 14 bar @25 $^{\circ}$ C and 7 bar@95 $^{\circ}$ C
- A-length 221 mm
- Cell constant 0.100 cm^{-1} (nominal)
- Conductivity range 0.02 to 2500 μ S/cm
- Resistivity range 0.4 K Ω cm to 50 M Ω cm

- Temperature sensor Pt 1000 TD, class A, 3 wire
- Temperature range -10 to 100 °C
- Accuracy $\pm 0.5\%$ (cell constant accuracy)
- Temperature accuracy @25 °C ± 0.1 °C

AI.9 Specifications of conductivity / resistivity transmitter

The important specifications of the conductivity meter are:

- Inputs
 - 2 inputs for conductivity or resistivity
- 2 inputs for temperature measuring devices
- Measuring range
- Conductivity 0.02 $\mu\text{S}/\text{cm}$ to 1000 mS/cm
- Resistivity 1.0 Ωcm to 50 $\text{M}\Omega\text{cm}$
- TDS 0 to 62500 ppm (as KCl)
- Temperature -10 to 140 °C
- Display
- 1 line, 16 character backlit LCD
- Analog Output
- 4 to 20 mA, isolated, 10V, maximum load of 500 Ω , user definable options
- Calibration
- NIST traceable calibrators for conductivity, resistivity and temperature
- Cell constant
- Any cell constant can be entered
- Temperature compensation

- Automatic reference to 25 °C for conductivity, resistivity and TDS
- Enter manually from 0 to 120 °C
- Auto-uncompensated, standard for NaCl impurities according to ASTM #1125-91, linear 0.0 to 99% /°C
- Accuracy
- Conductivity/resistivity $\pm 0.5\%$ of the reading
- Temperature $\pm 0.25^{\circ}\text{C}$ of the reading
- Analog output ± 0.01 mA
- Repeatability
- Conductivity/resistivity $\pm 0.5\%$ of the reading
- Temperature $\pm 0.075^{\circ}\text{C}$

AI.10 Specifications of PCI-MIO-16E-4 DAQ board

Some of the important specifications of the DAQ card are:

- Number of channels 16 Single ended
- Resolution 12 bits, 1 in 4096
- Maximum sampling rate 500 kS/s single-channel
 250 kS/s multi-channel
- Maximum working Voltage ± 11 V
- Over-voltage protection ± 25 V
- No missing codes 12 bits
- Offset error $\pm 16 \mu\text{V}$ to ± 0.8 mV
- Gain error $\pm 0.02\%$ of reading maximum
- Bandwidth 350 kHz

- Accuracy 4 μS typical and 8 μS max.
- System noise 0.5 dB
- Bandwidth 1 MHz
- Offset temperature coefficient $\pm 50 \mu\text{V}/^\circ\text{C}$